

学位論文

Study on Tokamak Plasma Performance for Fusion Energy Development Scenario

(トカマク型核融合炉開発シナリオの基盤となる炉心プラズマ研究)

2005 年度

提出先

東京大学大学院新領域創成科学研究科
基盤科学研究系先端エネルギー工学専攻

日 渡 良 爾

(blank page)

ACKNOWLEDGMENT

I would like to express my deep gratitude to Prof. Y. Ogawa. He have given me many interesting subjects and precious chances for my study. Even after I left the Univ. of Tokyo, he had been continuously encouraging and guiding me as a teacher. I respect not only wide knowledge on plasma physics and fusion technology, but also his gentle, kind, and patient personality. Without his kind and proper guidance, I could not have completed this work.

I would like to thank Drs. K. Okano, T. Yoshida, Y. Asaoka and K. Tomabechi for continuous discussion with me. They are senior researchers of me in Central Research Institute of Electric Power Industry (CRIEPI). They had given me a lot of chance to expand my study field, which had resulted in many part of this thesis. Especially, Dr. K. Okano gave me the chance to work on fusion energy in CRIEPI. I'm very happy to study on fusion energy with them.

Dr. T. Takizuka in Japan Atomic Energy Research Institute (JAERI) had given me many profound suggestions. Moreover, he had taken care of me during my stay in JAERI and in International Tokamak Physics Activity. Several topics in this thesis was motivated by discussion with him. I really appreciate them very much.

I would like to thank Prof. A. Hatayama in Keio University for his kind instruction in the divertor plasma transport. Regardless of my poor understanding on this topic, he had taught me kindly, and he had also given me the chance to participate in the international conference. I am really grateful for his kindness.

Drs. Houlberg in Oak Ridge National Laboratory (ORNL) and K. C. Shaing in the University of Wisconsin had conducted me during my stay in ORNL. Especially, I have to thank Dr. Houlberg for his arrangement of my stay in ORNL. It was kind of them to teach me the extended neoclassical transport theory as for internal and external transport barrier of tokamak plasma. Their instruction had promoted my understanding on the neoclassical transport theory. I really appreciate it.

Profs. N. Inoue and Z. Yoshida were also instructors during my graduate school days of Inoue Laboratory at the University of Tokyo. Prof. N. Inoue is the first person to teach me plasma physics and nuclear fusion energy. His attractive talk on confinement of ultra cold neutron for measuring the neutron lifetime affected me to want to be a researcher. Prof. Z. Yoshida had pointed out the incompleteness of my work and helped me to understandings through the seminar of Inoue Laboratory. Moreover, his attractive

talk on plasma physics including space and process plasmas affected me to like plasma physics much more than before. Without their kind instruction, I had not known this challenging subject, and could not complete this thesis.

Dr.K.Shinya has taught me to use the plasma equilibrium code TOSCA. I want to thank him very much for his kindness.

Drs. N. Hayashi, H. Shirai, S. Nishio, T. Hirayama, K. Shimizu, T. Ozeki in JAERI, Profs. T. Amaono, Y. Tomita, Dr. T. Yamamoto in National Institute for Fusion Science (NIFS) , Prof. A. Fukuyama in Kyoto University had discussed and helped me to understand plasma physics and fusion technology. I want to thank them very much.

I want to thank Mr.Y.Kuzuyama for his collaboration in Keio University. He made a lot of suggestions on the SOL-divertor transport modeling.

I want to thank all members of Inoue Laboratory at Graduate School of Quantum Engineering and System Science, the University of Tokyo, and all members of Advanced Reactor System Sector at CRIEPI.

Finally, I would like to express my gratitude to my wife Ms. Motoko Hiwatari, my parents Mr. Yoshiharu Hiwatari and Ms. Michiko Hiwatari, and my sister Ms.Ryoko Hiwatari, for their support during my long term studies.

Tokyo, March 2005
Ryouji Hiwatari

Contents

1	Introduction	1
1.1	Fusion Energy and Development status	1
1.2	Review of Conceptual Designs for a Tokamak Fusion Power Plant	7
1.3	Characteristics of Fusion Energy:Merits and Demerits	12
1.4	Development Stages of Fusion Power Plant	15
1.5	Urgent Issues for Fusion Energy Development Strategy	17
1.6	Contexture of This Thesis	19
	Reference	21
2	Plasma Performance Required for the Demonstration Reactor and the Commercial Reactor	23
2.1	Introduction	23
2.2	Analysis Method of Plasma Performance	28
2.3	Plasma Performance Required for the Electric Breakeven Condition	34
2.4	Plasma Performance Required for the Economic Breakeven Condition	49
2.5	Summary	54
	Reference	56
3	Plasma Design of Demonstration Reactor based on Early Realization Concept	59
3.1	Introduction	59
3.2	Design Policy and Conditions of Reactor Technology	62
3.3	Optimization of Core Plasma for Demonstration Reactor	66
3.4	Plasma Ramp-up Scenario	75
3.5	Operation Condition of Divertor Plasma	80
3.6	Summary	84
	Reference	85

4	Study on Critical Issues of Tokamak Plasma in Each Development Stage	87
4.1	Introduction	87
4.2	Core Plasma Transport Analysis	89
4.3	L-H Transition Modeling	118
4.4	Edge Plasma Transport Modeling	126
4.5	MHD and Current Drive Analysis for Demonstration Power Plant	135
4.6	Operation Condition Analysis for Highly Elongated Advanced Plasma	145
	Reference	155
5	Concluding Remarks	159
A	Physical elements of the design database	162
B	Conceptual design studies of fusion power plants	164

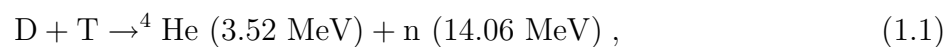
Chapter 1

Introduction

1.1 Fusion Energy and Development status

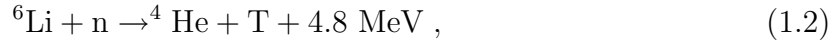
Fusion energy is the origin of solar power. It can be considered as the most abundant energy source in the world. Therefore, the fusion energy has been supposed to be the good candidate for the alternative energy source of fossil fuels in this about 50 years. That is why it has been researched in the long term in the world. Fusion reaction is happened only under the condition of high temperature and high density. Such high temperature and high density make nuclides close enough to cause fusion reaction by the tunnel effect. In the core of the sun, large gravitation causes fusion reaction. To realize the available energy from the fusion reaction, we have to find the way to induce the fusion reaction instead of large gravitation of the sun. How can we get the fusion reaction on the earth ?, which is the first issue to be resolved.

There are several kinds of the fusion reaction to realize the fusion energy on the earth. In Figure 1.1, fusion reaction rates for several kinds of combination are shown, and the fusion reaction rate of deuterium and tritium is largest in the lower temperature region. Hence, the easiest fusion reaction to be induced is the combination of deuterium and tritium as follows:



where induced nuclides are helium (He) and neutron (n), which have energy of 3.5 MeV and 14.0 MeV, respectively. However, the tritium is a radionuclide and does not exist in the nature. This is the second issue to be solved. Fortunately, with the neutron induced

in equation (1.1), the tritium can be produced by the following reactions;



The cross section of the first reaction is larger than that of the second one , and not only tritium production but also thermal energy generation can be possible because of an exoergic reaction. However, the fraction of ${}^6\text{Li}$ in the natural lithium is 7.5%, the major reaction of the natural lithium is the second equation, which is an endoergic reaction.

Hence, enrichment of ${}^6\text{Li}$ is effective to improve the tritium production and the thermal efficiency. Figure 1.2 shows the overall system of a fusion power plant by the fusion reaction of deuterium and tritium. The fusion reaction is induced in the reactor core. The device for tritium production and thermal energy output, which is called the blanket system, is located around the reactor core plasma. The tritium produced in the blanket system is extracted and fueled into the reactor core plasma. The thermal energy from the blanket system is also transferred to the turbine to generate electricity. We have to supply the deuterium and lithium as fuels. The deuterium exists abundantly in sea water, and the fraction of its comprisal in sea water is about 1.5% of the hydrogen.

The next issue is how to get the high density and high temperature enough to induce the fusion reaction. As mentioned, the central core of the sun has gravitation large enough to achieve the high density for the fusion reaction. Such high density is very difficult to achieve artificially. Hence, the research of the fusion energy focused on how to confine the dense deuterium and the tritium with high temperature enough to induce the fusion reaction. Generally, high temperature makes materials melted and boiled, and material state changes from solid state, to liquid state, and to gas state at last. Temperature required to induce fusion reaction is much higher than that required for the gas state. Further higher temperature makes the constituent atoms of materials separate into ions and electrons, that is, ionize from the gas state. Such ionized state is called plasma state. Usually, the fusion reaction is considered to be induced in the plasma state. How do we realize such high temperature and high density plasma on the earth ? In order to answer this problem, about half of century is spent for the fusion energy research.

Now, fusion plasma will be almost realized soon in the International Thermonuclear Experimental Reactor (ITER) project[1-1]. ITER is supposed to be the first device to get the fusion plasma, which is almost self-heated by fusion products, alpha particle. To complete the ITER project, a lot of scientists has been researching a lot of problems about plasma physics and engineering techniques. When the ITER project will be suc-

cessful, fusion plasma and reactor technology required for the fusion power plant will be fundamentally demonstrated. However, it was not easy to break the road to the ITER project.

The development history can be seen in Figure 1.3. In 1960's and 1970's, the first tokamak device 'T-3' was developed in Soviet union, and the principle demonstration of tokamak plasma was carried out. The following several small devices confirmed its result. In 1980's, PLT, Doublet III, T-10, ASDEX and so on were developed, and plasma performance was improved step by step. In 1990's, the break-even condition, which means the output power from fusion reaction is larger than the input power of plasma heating, was achieved in JET and JT-60U[1-2, 1-3]. You can see that we are ready for carrying out the burning plasma experiment.

On the other hand, the reactor technologies such as super conductor, structure materials, plasma heating and current drive method, tritium handling and so on, have also been developed. The 13T-42kA central solenoid coil and 13T-60kA toroidal coil with Nb₃Sn have already developed, and the experiments for demonstration of its performance was carried out in the ITER R&D activities[1-1]. Furthermore, the 13T-42kA Nb₃Al super conductor system has also developed, and larger magnetic field 16T with Nb₃Al super conductor for a demonstration fusion reactor is aimed at in JAERI[1-4]. The development status of the most promising structure material, that is ferritic steel, is shown together the development goal of other materials in Figure 1.4 [1-5]. The ferritic steel has a good potential to apply to the demonstration fusion reactor, however, it may not be enough to apply to the commercial fusion reactor because operation temperature of the ferritic steel, which should be as high as possible for the high thermal efficiency, is restricted under about 500 °C. Advanced materials of Vanadium alloy and SiC/SiC composite are preferable as shown in Figure 1.4 and are being developed now. Plasma heating and current driving are carried out with wave heating (RF) and neutral beam injection (NBI) method. In case of RF method, 170GHz-1MW gyrotron has developed and can be operated for 2.0 sec[1-1]. We have to improve it for higher frequency oscillation up to 300GHz for the high magnetic field over 13 T. In case of NBI method, beam energy up to 1 MeV and negative ion source with 400keV and 13.5A have been achieved[1-1]. Accelerator for higher beam energy and plasma neutralizer cell[1-6] for higher system efficiency are being developed for the demonstration reactor and the commercial one.

According to the present technologies mentioned above, we can conclude that burning plasma experiments is possible with the present technology with the ITER project, however, we have to develop more advanced technologies for the demonstration and com-

mercial fusion reactors. The difference of technology between ITER and a commercial reactor is not clearly clarified yet. Hence, we are still unsure when fusion energy can be realized. We should precisely investigate the development goal and the advancement from the present technology so as to make it clear when the fusion energy can be available.

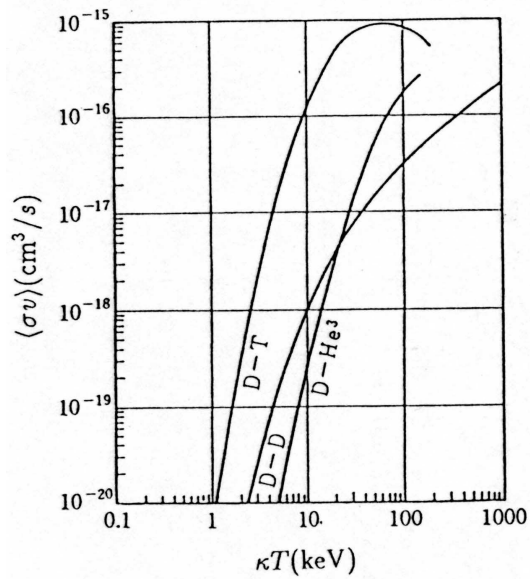


Figure 1.1: The dependence of fusion range $\langle \sigma v \rangle$ on the ion temperature T_i for several fusion reactions[1-7]

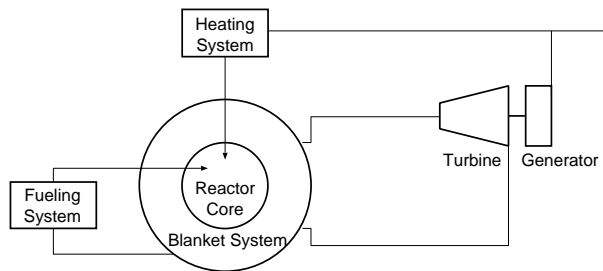


Figure 1.2: An basic concept of a fusion power plant system based on a D-T fusion.

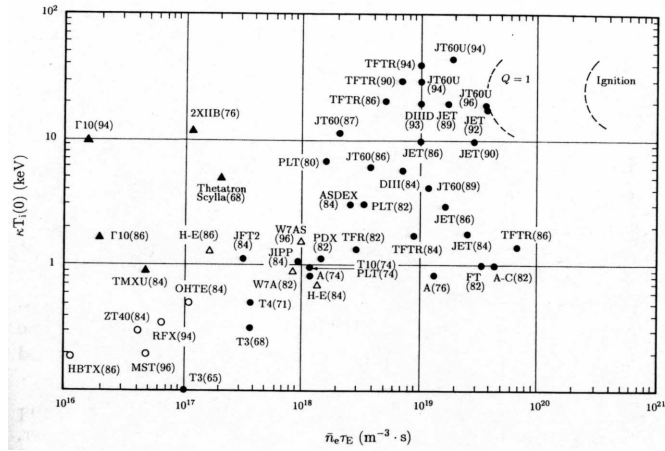


Figure 1.3: Development history in $n_e \tau_E - \kappa T_e(0)$ space[1-7].

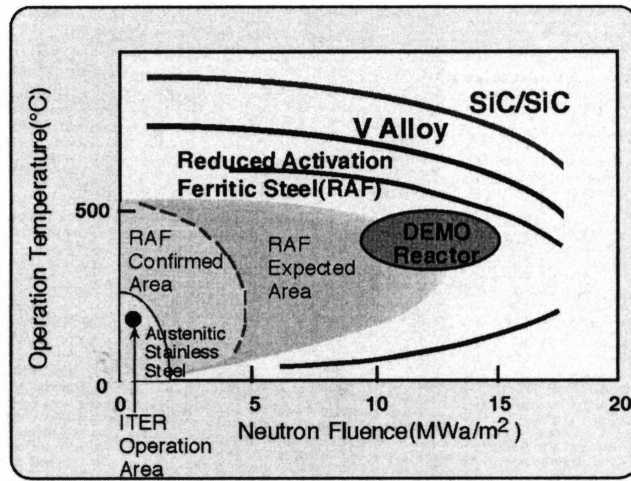


Figure 1.4: Design windows of the structural materials for a fusion power plant[1-5].

1.2 Review of Conceptual Designs for a Tokamak Fusion Power Plant

Conceptual design studies of fusion power plants were carried out to understand the development goal of plasma performance and reactor technologies. In this section, recent design studies i.e CREST[1-8], ARIES-AT[1-9], and A-SSTR2[1-10], are reviewed. These three design focused on economic competitiveness with other energy sources. In this section, COEn, which is the COE normalized by the that of the present coal plants in Japan, is considered for comparison of economic competitiveness. Under the condition of 1GWe net electric power, predicted COEn values of the CO₂ controlled fossils fuel plant and the light water reactor fission plant, at 50 years in the future are 1.5 ~ 1.8 and 1.0 ~ 1.5, respectively[1-11]. The target range of COEn for CREST, ARIES-AT, and A-SSTR2 is from 1.0 to 1.3, which corresponds to from 50mill/kWh to 65 mill/kWh as shown in Table 1.1. Simply speaking, the key parameters of a tokamak fusion power plant for economic competitiveness are a normalized beta value β_N and a thermal efficiency η_e . The higher β_N enables to achieve higher power density, which leads to the compact reactor and small construction cost. Needless to say, the high thermal efficiency is essential not only to a fusion power plant but also to other power plant. Main parameters of CREST, ARIES-AT, and A-SSTR2 are also shown in Table 1.1. To achieve the economic competitiveness, different design criteria are adopted to CREST, ARIES-AT, and A-SSTR2, respectively. Each design concept is summarized as follows. Those conceptual designs are useful to understand the typical goal of fusion energy development.

- **CREST**[1-8]

Fusion power plants in the future should be made economically and environmentally attractive compared with other advanced energy sources. In particular, the achievement of a competitive cost of electricity (COE) is the first priority for electric power industries. The compact reversed shear tokamak CREST is a cost competitive reactor concept based on a reversed shear (RS) plasma with a moderate aspect ratio $A = 3.4$ which is similar to the ITER advanced mode plasma. This study emphasized that presentation of such a concept based on ITER should be worth while for formulating a fusion development strategy. The Bird's-eye view of the CREST fusion power plant core is shown in Figure 1.5[1-8].

The design target of CREST is a cost competitive 1 GWe power plant. This will require about 3 GWth fusion output. A higher output would result in a lower COE,

but too high an output for a single plant may not be desired by the utilities because of network stability considerations. The aspect ratio and the plasma configuration of CREST should be as close as possible to the ITER advanced mode plasma, because testing by ITER is an important policy in the CREST study.

The cost assessment study for the CREST design shown that high normalized beta value β_N and high thermal efficiency η_e are the most effective key parameters for reducing the COE of tokamak reactors. The parametric study on COE has shown that a very high normalized beta value of $\beta_N \geq 5.0$ is required in order to achieve a competitive cost. Such a high β_N plasma may be realized with reversed shear (RS) operation of a tokamak, which is applied to the CREST design. As for thermal efficiency, a water cooling and ferritic steel materials system have been chosen in the CREST design, because a large database and extensive industrial experience exist for this combination, and therefore it seems to be a reliable path to power reactors, at least to the early generation of fusion reactors following the ITER project.

A reduced activation ferritic steel is adopted for the main in-vessel components, which is compatible with a high thermal efficiency cycle ($\eta_e = 41\%$) based on superheated steam. Current profile control and high speed plasma rotation by neutral beam current drive (NBCD) stabilize the ideal MHD activity up to the normalized beta value $\beta_N = 5.5$ with a closed conductive shell, which is installed in the breeding blanket.

- **ARIES-AT**[1-9]

The conceptual design study of ARIES-AT was initiated to assess the potential of high-performance tokamak plasma together with advanced technology in a fusion power plant. Several avenues were pursued in order to arrive at plasma with higher β_N and β . Advanced technologies that are examined in detail include: (1) Possible improvements to the overall system by using high-temperature superconductors, (2) Innovative SiC blankets that lead to a high thermal cycle efficiency of $\eta_e \sim 60\%$; and (3) Advanced manufacturing techniques which aim at producing near-finished products directly from raw material, resulting in low-cost, and reliable components. The 1000MWe ARIES-AT design has a major radius of 5.4 m, minor radius of 1.3 m, a toroidal β of 9.2 % ($\beta_N = 5.5$) and an on-axis field of 5.6 T. Figure 1.6 shows the bird's-eye of the ARIES-AT fusion power plant core. The plasma current is 13 MA and the current drive power is 24 MW. The ARIES-AT study shows that

the combination of advanced tokamak modes and advanced technology leads to attractive fusion power plant with excellent safety and environmental characteristics and with a COE (50 mill/kWh), which is competitive with those projected for other sources of energy.

- **A-SSTR2**[1-10]

An advanced commercial reactor concept (A-SSTR2), which is a compact power reactor ($R_p = 6.2$ m, $a_p = 1.5$ m, $I_p = 12$ MA) with a high fusion power ($P_f = 4$ GW) and a net thermal efficiency of $\eta_e = 51$ %, has been proposed in order to meet both economical and environmental requirements. Figure 1.7 shows the bird's-eye view of the A-SSTR2 fusion power plant core. The machine configuration is simplified by eliminating the center solenoid (CS) coil system. An SiC/SiC composite for the blanket structure material, helium gas cooling with a pressure of 10 MPa and an outlet temperature of 900 °C, and TiH₂ for the bulk shield material are introduced. For the toroidal field (TF) coil, a high temperature superconducting wire made of bismuth with a maximum field of 23 T and a critical current density of 1000 A/mm² at a temperature of 20 K is applied. In spite of the CS-less configuration, a computer simulation gives satisfactory plasma equilibria, plasma initiation process, and current ramp-up scenario. The current ramp-up time is about 22 hours. The MHD stabilities for the ballooning mode and the ideal low n kink-modes are confirmed. The stabilization of $n = 1$ and $n = 2$ kink modes requires a shell position closer than 1.4 times and 1.2 times the plasma minor radius, respectively. With regard to the divertor thermal condition, it was found that a neon gas-seeded divertor plasma with a fraction of ~ 2.5 % gives a thermal load reduction at the divertor plate from 460 MW to 100 MW and a plasma temperature drop at the divertor plate from 200 eV to 20 \sim 30 eV. By increasing the shield thickness by about 15 cm, the total radioactive waste is dramatically reduced. The radioactive waste percentage relative to the total waste is reduced from 92 wt.% to 17 wt.%.

Table 1.1: Main parameters of CREST[1-8], ARIES-AT[1-9], and A-SSTR2[1-10]. The definitions of these parameters are shown in Appendix A

	CREST	ARIES-AT	A-SSTR2
β_N (-)	5.5	5.5	4.0
R_p/a_p (m)	5.4/1.59	5.2/1.3	6.2/1.5
κ/δ (-)	2.0/0.50	2.2/0.78	1.8/0.4
I_p (MA)	12	13	12
f_{bs} (-)	0.83	0.92	0.83
q_ψ (-)	4.3	3.6	5.1
β_p (-)	2.5	2.3	2.9
B_t (T)	5.6	6.0	11.0
$\langle T_e \rangle$ (keV)	15.4	15.8	18.8
Z_{eff} (-)	2.2	1.8	1.6
$\langle n_e \rangle$ (10^{20}m^{-3})	2.1	2.3	2.0
fn_{GW} (-)	1.3	1.0	1.2
HH (-)	1.3	1.4	1.3
P_{CD} (MW)	97	36	60
P_f (MW)	2970	1755	4500
η_e (%)	41	59	54
P_e^{net} (MW)	1163	1000	2550
COE (mill/kWh)	~ 65	~ 50	~ 60

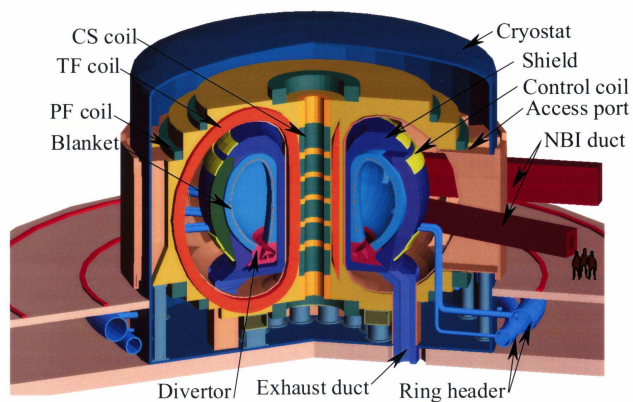


Figure 1.5: Bird's-eye of the CREST fusion power plant core

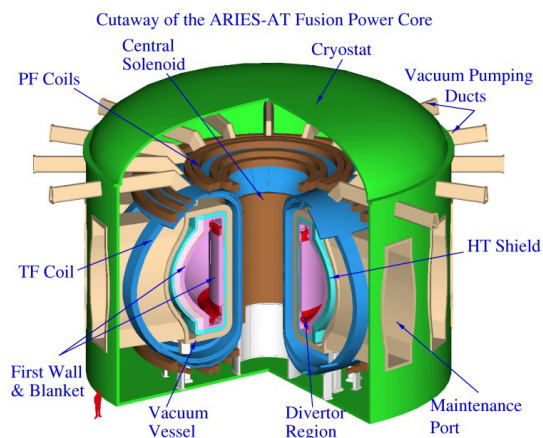


Figure 1.6: Bird's-eye of the ARIES-AT fusion power plant core

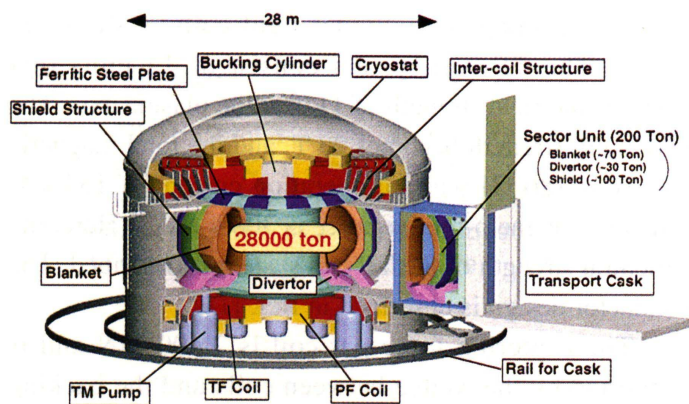


Figure 1.7: Bird's-eye of the A-SSTR2 fusion power plant core

1.3 Characteristics of Fusion Energy: Merits and Demerits

The characteristics of a fusion power plant are gradually understood through the conceptual design study as mentioned in the previous section. In this section, those characteristics are summarized. First of all, as for fuels, the deuterium is abundant in the sea water. The lithium of the material for the tritium is considered to be abundant, but its mine is not widely spread in the world. A technique to abstract lithium from the sea water is also underway, and completion of this technique leads fusion energy to the ultimate energy source in the earth. This will be the first merit to be mentioned on the fusion energy.

The second merit is less CO₂ emission during operation. Recently, the greenhouse effect is considered to be a critical issue in the world. Figure 1.8 shows the change of the CO₂ concentration in the atmosphere of the south pole (at Vostok station in East Antarctica)[1-12]. The CO₂ concentration is changing in the long period about 10000 years, and the upper region was 280ppmv. On the other hand, it should be noted that during recent only 100 years, the CO₂ concentration have jumped up to 380 ppmv and is still increasing as shown in Figure 1.9[1-13]. This sudden change of the CO₂ concentration is supposed to be result in the greenhouse effect. According IPCC activity, in order to keep the CO₂ concentration less than 550ppmv (twice of the industrial revolution period), the emission of CO₂ has to be reduced by the year 2050. The fusion energy may contribute to this problem because of less CO₂ emission during operation.

The third merit is the controllability of nuclear fusion reactor. From the nature of the system of a fusion reactor, it never falls into uncontrollability such as in a nuclear fission chain reaction. Therefore, there is no worry about the severe nuclear accident.

On the other hand, there are also several demerit in the fusion energy. One is the radioactive waste. Indeed, the fusion energy does not produce the high-level radioactive waste, but does the low-level one. According to the recent research of the future fusion power plant, the amount of the low-level radioactive waste is considered to be almost equal to or larger than the usual light water fission reactor. A part of the low-level radioactive waste has to be under the control for a certain period about 100 year.

The second demerit is, generally speaking, the large plant scale to generate available energy, which relatively results in large construction cost. This mainly comes from the fusion plasma property and the highly technological devise. There are mainly two method to realize the fusion energy on the earth, that is, a magnetic confinement fusion and a inertial confinement fusion (this method is outside the scope of this thesis). In case of

the magnetic confinement fusion such as the tokamak reactor, the size of fusion plasma required to generate electricity results in a large device size, because of the property of plasma performance. On the other hand, the inertial confinement fusion does not have a larger reactor than the magnetic confinement fusion, because the size of target for fusion reaction is roughly less than 10 cm. However, the driver system for fusion reaction, which is usually considered to be a high power laser system, becomes a large scale according to the present laser technology. The large scale device relatively results in the large construction cost. To get the economic competitiveness of the fusion energy, usually, increasing a plant scale is taken, and this results in the difficulty of introduction of a fusion power plant, because of unbalance between the total capacity of electric system and the large electric output of a fusion power plant. The key issue is how small device and electric output is feasible with a reasonable cost in a fusion power plant.

The last demerit is that a fusion power plant can not start up by itself. There are two reasons. One is the tritium of the special fuel, which can not be stored because it is the radionuclide of 12 years half-life. This means that the initial tritium has to be imported from other fusion plants at the beginning of operation. The other is the large initial electricity required for startup from other power plants.

The fusion development strategy should be constructed in order to advance its merit and to overcome its demerit. Recently, the possibility to reduce the total radioactive waste is proposed in the A-SSTR2 design[1-10], and this analysis shows that total radioactive waste from a fusion power plant can be 1000 ton less than from a usual light water fission reactor. The key issue of this method is the development of materials. Further, as for the tritium, the possible way to commission a fusion power plant without initial tritium is proposed in the CREST design[1-14], and this proposal shows that it takes about three months to achieve the rated power operation. In this method, tritium is produced by a neutron from the beam direct fusion reaction by a high energy particle of NBI. The key issue of this method is transport property of tritium in the fusion plasma and the recovery efficiency in the fuel cycle system. If this commissioning method without external tritium supply is possible, transportation of tritium is not necessary for a fusion power plant. This possibility is very important, because transportation of radioactive materials may not be necessary in a fusion power plant when the radioactive waste can be disposed of within the plant site.

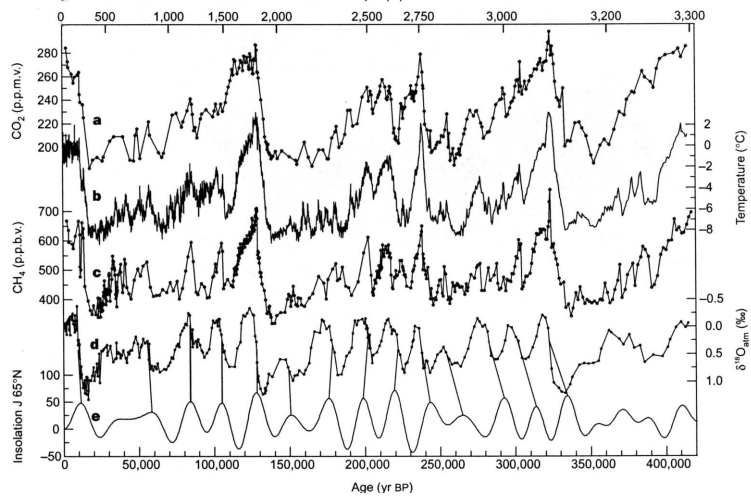


Figure 1.8: Vostok time series and insolation. Series with respect to time of : **a**, CO₂; **b**, isotopic temperature of the atmosphere; **c**, CH₄; **d**, $\delta^{18}O_{atm}$; and **e**, mid-Jun insolation at 65°N (in Wm^{-2})



Figure 1.9: Recent CO₂ concentration at the south pole

1.4 Development Stages of Fusion Power Plant

To realize the fusion power plant, its development strategy from ITER to a commercial plant such as CREST, ARIES-AT, and A-SSTR2, should be structured prudently enough to maximize the merits of the fusion energy as mentioned in the previous section. For the development strategy of the fusion power plant, the following four stages of development and each mission have to be considered [1-15].

1. **The stage for demonstration of a fusion reactor operation:** To establish plasma physics and engineering techniques for steady state operation of burning plasma with high energy multiplication factor.
 - high efficiency of plasma current drive, reduction of heat load to the divertor plates, exhaust of helium ash, control to avoid plasma disruption.
 - steady state plasma operation.
 - inevitable engineering techniques for continuous energy production from a fusion reactor.
 - prospect for developing characteristics and inevitable devices required for a fusion reactor.
 - technologies for continuous tritium handling on a plant scale.
 - technologies for manufacturing reliably the large devices (superconductor coil, vacuum vessel, and so on) with good function as designed.
 - technologies for remote maintenance.
 - development of materials and systems against high neutron flux load.
2. **The stage for demonstration of net electric power generation as a power plant:** To establish inevitable systems and technologies for electric power generation on a plant scale.
 - steady state plasma operation with high energy multiplication factor.
 - plasma performance similar to that of a commercial reactor, or certain prospect for it.
 - flexible control method required for a commercial reactor, i.e., partial load operation, unpredictable shutdown and so on.

- an electric generation system (i.e., electric output, coolant temperature, system structure and so on) similar to that of a commercial reactor.
 - self-sustainment of tritium.
 - techniques for safety, maintenance, and management and disposal of the wastes to advance the economic performance.
 - continuous long-term operation almost similar to that of a commercial reactor.
 - development and applicability of materials for a commercial reactor.
3. **The stage for demonstration of economic and safe performance:** To establish safe and economic performance required for a power plant.
- plasma performance and engineering design as same as a commercial plant.
 - specification of removable device and system to advance economic performance of a commercial plant.
 - achievement of steady state operation with good economy.
 - specification of merits and attraction of the fusion power plant.
4. **The stage for commercial use:** To establish attraction and competitiveness of fusion energy.
- good public acceptance promoted by stable, safe and economy operation.
 - attractive fusion power plant making the best of advantages of fusion energy.

In the case of the fast breeder reactor development, a specific device has been built in each stage as experienced in France in order to minimize the development cost, because any power level can be selected for a device to be built.

On the other hand, each stage in the development of the fusion power plant does not necessarily require the respective device to be built, because the thermal output from the experimental reactor such as ITER is inevitably large and can be gradually increased as the plasma performance improves. Eventually, the net electric power from an experimental reactor can be almost similar to the commercial reactor by replacing the blanket system with the advanced one having a higher thermal efficiency[1-15]. For example, the Fast Track Approach recently developed for aiming at early realization of the fusion power plant in 2030's suggested a roadmap somewhat different from the usual, i.e., the second and third stages mentioned above, which usually correspond to the demo

and proto-type reactor stages, will be combined into a single step[1-16, 1-17]. On the basis of this development concept, a new development strategy is being discussed, and would be re-constructed in Japan, EU and US. In the present paper, we assume this early realization concept of the fusion power plant and use the new term, ‘electric demonstration plant’, concerning the device for early realization concept. (The conventional development strategy forecasts a timescale of about 50 years towards the commercial scale. The early realization concept would shorten this period with in 20~30 years from ITER by reducing from two to one the number of generations of experimental machines after ITER. This is why we say the early realization concept.)

1.5 Urgent Issues for Fusion Energy Development Strategy

When a development strategy for the fusion energy is discussed, an important issue is how to maximize the contribution of the fusion energy to the world energy supply. This was investigated by Tokimatsu *et al.* with consideration of the cost and CO₂ emission[1-18, 1-19]. According to that study, fusion energy has a potential to generate 20% of the total electricity of the world in the year 2100, if introduction of fusion will be made in the year 2050. Simultaneously, fusion energy also contributes to decrease the atmospheric CO₂ concentration, which is considered as a critical world problem as pointed out in Section 1.3. According to ref.[1-20], the atmospheric concentration of CO₂ has to be decreased by the year 2050, so as to keep the CO₂ level at 550 ppmv, less than a level of twice that at the industrial revolution period, by the year 2100. If fusion power plants are realized before the year 2050, fusion energy will become one of the practical candidates to play an important role in decreasing the atmospheric CO₂ concentration. Consequently, the early realization of fusion power plants before the year 2050 has the significant potential to maximize the contribution of fusion energy to reduce the atmospheric CO₂ concentration. In addition, the early realization would lead to the smooth introduction of fusion energy into the energy sources in the world. Hence, it is worthwhile to consider the early realization concept such as Fast Track Approach for the fusion energy development.

The discussion on the development strategy for realizing fusion energy should be made prudently, but the requirements of plasma performance and reactor technology to generate net electric power and to get the economic competitiveness have not been understood

clearly yet. Such requirements are inevitable in discussing the development strategy of fusion energy. Figure 1.10 shows the roadmap of the fusion energy development. Roughly speaking, there are supposed to be three milestones in the fusion energy development, that is, the break-even condition, the electric break-even condition, and the economic break-even condition[1-21]. The first milestone is the usual break-even condition of fusion power equal to the heating power, which was achieved in JET and JT-60U[1-2, 1-3]. The electric break-even condition means that gross electric power generation is larger than the circulating power in a power plant. The economic break-even condition means that the COE of fusion energy is reasonably cheap enough to be selected as an alternative energy source in the market.

To structure the development strategy after the ITER project, understanding of the second and third break-even conditions is inevitable, because understanding those conditions leads to clarify the development goal of plasma performance and reactor technology. Clarification of the development goal enables to classify the priority of element technology to be developed for the fusion power plant. Accordingly, the feasible development strategy can be structured. However, at present, remaining break-even conditions for a fusion power plant are still ambiguous, and the discussion on the priority of the elemental technology of the fusion power plant is not sufficient. Since the development strategy is supposed to have an effect on the experimental program in the ITER project, each break-even condition and the development priority required for the development strategy have to be clarified, at least, by the beginning of ITER experiments. This is the urgent issue for the fusion energy development strategy.

1.6 Contexture of This Thesis

The objectives of this thesis are as follows;

1. to investigate the plasma performance and the reactor technologies required to achieve the electric and economic break-even conditions (in Chapter 2);
2. to carry out the plasma design of the electric demonstration plant under the condition of the early realization concept in order to derive the critical issues in each development stage of a development scenario consistent with the ITER project(in Chapter 3);
3. to resolve several critical issues in each development stage for the development scenario proposed in this thesis(in Chapter 4).

The first objective in Chapter 2 has to be carried out whenever any development strategy will be discussed. In this thesis, the conventional tokamak configuration like ITER is taken into account, and it should be noticed that a low aspect ratio tokamak (spherical torus) is outside the scope of this thesis.

To classify the priority of development and to derive the critical issues in each development stage, it is necessary to construct actually a development scenario consistent with the ITER project. In this chapter 3, based on the present early realization concept, a conceptual design of an electric demonstration plant will be carried out to construct a development scenario of the fusion energy. It should be noticed that the optimization of design parameters for an electric demonstration plant depends on the design criterion, and the development priority for one design criterion may be different from that for the other criterion. However, when the same development goal of a commercial fusion power plant is aimed at, the same critical issues will be derived from the different development scenario, and we expect that the difference is when the critical issue should be resolved in the development scenario.

In Chapter 4, several critical issues in each development stage including the experimental reactor (ITER) stage will be analyzed, and summarized in Chapter 5.

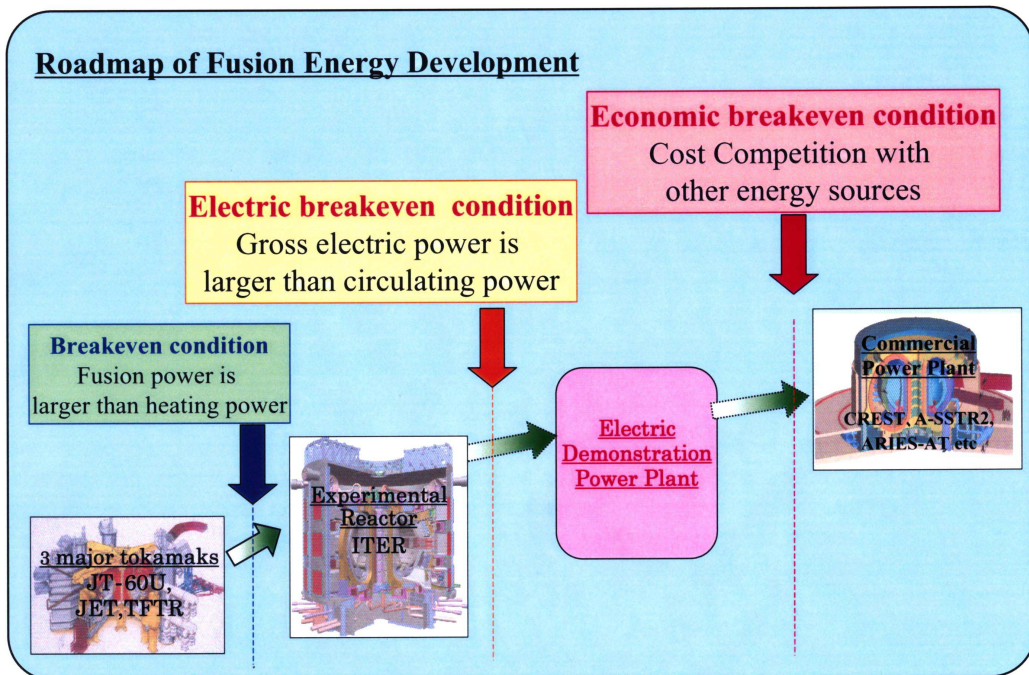


Figure 1.10: A roadmap of fusion energy development

Reference

- [1-1] Technical basis for the ITER final design report *ITER EDA Documentation Series No.24* (Vienna: IAEA) 2001
- [1-2] JET TEAM, The new experimental phase of JET and prospects for future operation IAEA-CN-60/A1-3 *Proc. 18th IAEA Fusion Energy conf.(Seville, September 1994)*(Vienna: IAEA)
- [1-3] S. Ishida and JT-60 Team, Nucl. Fusion **39**(1999)1211
- [1-4] N. Koizumi. *et al*, Cryogenics **42**(2002)675
- [1-5] M. Seki *et al*, Fusion Science and Technology **42**(2002)50
- [1-6] V. M. Kulygin *et al* Nucl. Fusion **41**(2001)355
- [1-7] K. Miyamoto, Fundamentals of Plasma Physics and Controlled Fusion, Iwanami Book Service Center, Japan, 1997
- [1-8] K. Okano *et al*, Nucl. Fusion **40**(2000)635
- [1-9] F. Najmabadi *et al*, ARIES-AT: An advanced tokamak, advanced technology fusion power plant steady-state tokamak reactor IAEA-CN-77/FTP2/15 *Proc. 18th IAEA Fusion Energy conf.(Sorrento, October 2000)*(Vienna: IAEA)
- [1-10] S. Nishio, *et al* J.Plasma Fusion Res. **78**(2000)1218
- [1-11] K. Okano *et al*, Fusion Eng. Des. **51-52**(2000)1025
- [1-12] J. R. Petit *et al*, Nature **399**(1999)429
- [1-13] World Data Centre for Greenhous Gases <http://gaw.kishou.go.jp/wdcccgg.html>

- [1-14] Y. Asaoka *et al*, Commissioning of a D-T fusion reactor without external supply of tritium, IAEA-CN-77/PDP/8 *Proc. 18th IAEA Fusion Energy conf.(Sorrento, October 2000)*(Vienna: IAEA)
- [1-15] Y. Asaoka *et al*, Research and Development Steps for Commercial Use of Fusion Power Plants, CRIEPI Research Report T97077, Central Research Institute of Electric Power Industry, Tokyo, 1997(In Japanese)
- [1-16] European Commission Community Research *ITER, THE ROAD TO FUSION ENERGY* (Office for Official Publications of the European Communities,L-2985 Luxembourg)
<http://europa.eu.int/comm/research/energy/pdf/fusiontheroadn2.pdf>
- [1-17] H. Bolt, Fast Track Concept in the European Fusion Program *Report of International Symposium for ITER(Tokyo, 24 January 2002)*
<http://www.naka.jaeri.go.jp/keijiban/iter-symposium/report.html> (JAERI, Tokyo, 2002)
- [1-18] K. Tokimatsu *et al*, Energy Policy **31**(2003)775
- [1-19] K. Tokimatsu *et al*, Nucl. Fusion **42**(2002)1289
- [1-20] Contribution of Working Group III to the Third Assessment Report of the Intergovernmental Panel on Climate Change 2001 *CLIMATE CHANGE 2001 Mitigation* (UK: Cambridge University Press) p 25
- [1-21] R. Hiwatari *et al*, Introduction condition of a tokamak fusion power plant as a innovative technology into world energy scenario. IAEA-CN-116/SE/P3-40 *Proc. 20th IAEA Fusion Energy conf.(Vilamoura, November 2004)*(Vienna: IAEA)

Chapter 2

Plasma Performance Required for the Demonstration Reactor and the Commercial Reactor

2.1 Introduction

It is considered that there are three milestones toward the introduction of the fusion energy as shown in Figure 1.10. The first one is the energy production equal to the input energy, which is the usual break-even condition. The first milestone was completed, and we have to develop plasma performance and reactor technologies so as to generate net electric power in a plant scale, that is, the electric break-even condition. This is the second milestone. Because this second milestone is not completed, the fusion energy is not currently expected as an alternative energy source even in the long term world energy scenario. The completion of the second milestone, the electric break-even condition, is important for the fusion energy to be recognized as one of the suitable candidates for the alternative energy source. The last one is to generate electric power economically enough to be selected as the alternative energy source, that is, the economic break-even condition. When the economic break-even condition of the fusion power plant is analyzed, we have to compare COE (cost of electricity) of the fusion power plant with that of other energy sources.

Several economic analyses on the fusion power plant were carried out[2-1, 2-2, 2-3]. For example, Okano *et al.* carried out the economic comparison of the fusion power plant with other energy sources including the future innovative technologies, *e.g.*, a fast

breeding reactor, a light water reactor based on uranium from the sea water, a fossil fuel plant with CO₂ control, a geothermal energy plant, a wind power plant, an ocean thermal energy conversion plant, and a solar power plant as shown in Figure 2.1[2-2]. This study concluded that a reasonable target of COE for the first generation of fusion reactors should be cheaper than that for the CO₂ controlled fossil fuel plant, because the CO₂ controlled fossil fuel plant will be a more feasible choice from the economic view point when the COE of fusion plants exceed that of the CO₂ controlled fossil fuel plant. Several similar economic analyses of fusion power plants were carried out, however, these analyses can not show the introduction time and the consequent share of the fusion energy in the market.

Recently, the potential of the fusion energy in a long term world energy scenario is being investigated, and the introduction year and the consequent share for the fusion energy is estimated together with the break-even price of COE[2-4, 2-5]. In this study, future uncertainties, e.g. energy demand scenarios and capacity utilization ratio of options in energy/environment technologies, are considered as several cases of world energy scenario. This analysis was carried out by using a long term world energy and environmental model (this model is used in the New Earth Plan by the Japanese Government and for IPCC post SRES activity), and estimate that the break-even price of the fusion energy for introduction in the year 2050 under the constraint of 550 ppmv CO₂ concentration (twice level at the industrial revolution period) is the range of from 65 mill/kWh to 135 mill/kWh (1000 mill=1 dollar) as shown in Figure 2.2[2-5]. The width of break-even price mainly comes from future uncertainties of the world energy scenario.

The typical value of the economic break-even condition is considered as the break-even price for introduction of the fusion energy into the long term world energy scenario. Of course, the break-even price is not the sufficient condition but the necessary condition. If the cost of electricity (COE) for the fusion energy can achieve the lowest break-even price of this range, i.e. 65 mill/kWh in the year 2050, as a result of smooth introduction of the fusion energy, 20% share of the fusion energy in all produced electricity in 2100 is expected as shown in Figure 2.3[2-5]. This range of the break-even price is estimated under the condition of the plant availability 60% for the first fusion power plant. This availability is rather low, because an unexpected outage of operation for the first fusion power plant should be considered in the plant availability. Of course, annual cost reduction of COE for 25 years after the first introduction is assumed because of improving the plant availability, operation cost and so on.

Figure 2.2 indicates that the later the introduction year of the fusion energy, the

more expensive break-even price is acceptable, however, it should be noticed that the share of produced electricity by the fusion energy in 2100 decreases with delay of the introduction year. For example, delayed introduction of the fusion energy in 2070 will result in only about 4% share in 2100[2-4]. The earlier introduction of fusion energy, the more important role in the long term world energy scenario the fusion energy will play in 2100. The concentration of CO₂ in the atmosphere has been recognized as a critical environmental issue to date, and the CO₂ emission has to be decreased by 2050, so as to keep the CO₂ level at 550 ppmv (less than the level of twice that at the industrial revolution period) by 2100[2-6]. Fusion energy has a potential enough to reduce the CO₂ emission[2-7], and when its introduction in 2050 is realized, consequently, the fusion energy can also contribute the world energy scenario to keep 550 ppmv CO₂ level in 2100. The key point for maximizing the role of the fusion energy is how early fusion energy will be ready for electric power generation at a lower COE than the break-even price. Delayed introduction at a lower cost is not effective for maximizing the role of the fusion energy. Hence, early demonstration of electric power generation in a plant scale is also important. In this study, we consider the introduction year 2050 of fusion energy as the year we should aim at, and we clarify the following conditions by using a fusion power plant system analysis code (FUSAC)[2-8]; (1) the electric break-even condition which is required for the fusion energy to be recognized as a suitable candidate of an alternative energy source in the long term world energy scenario, and (2) the economic break-even condition which is required to be selected as an alternative energy source.

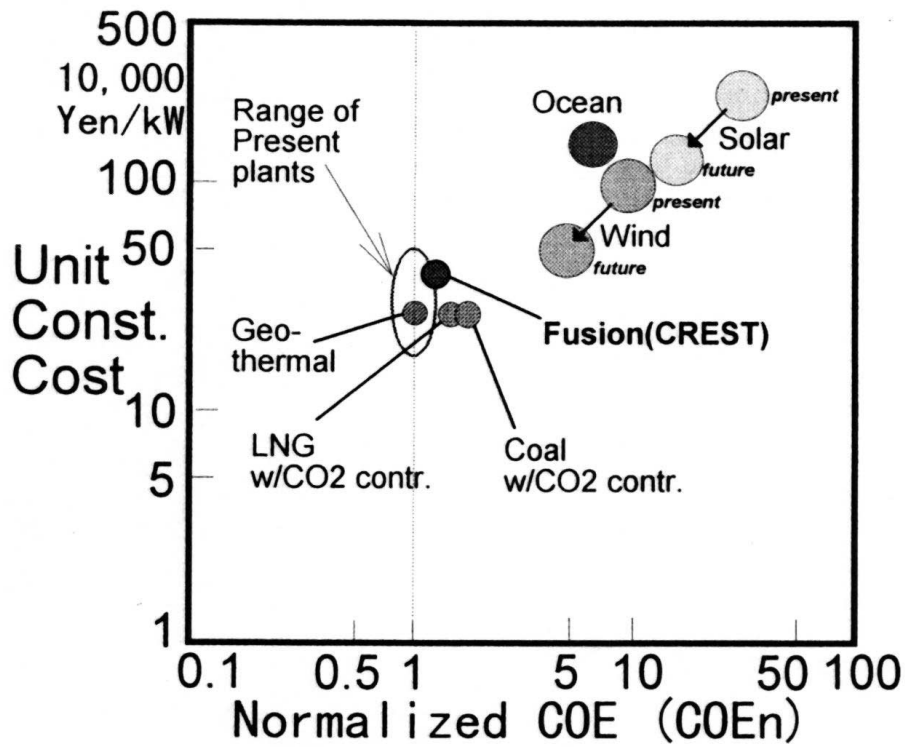


Figure 2.1: Normalized COE (COEn) and construction cost of various advanced power plants. COEn is normalized by the COE of the present coal plants in Japan.

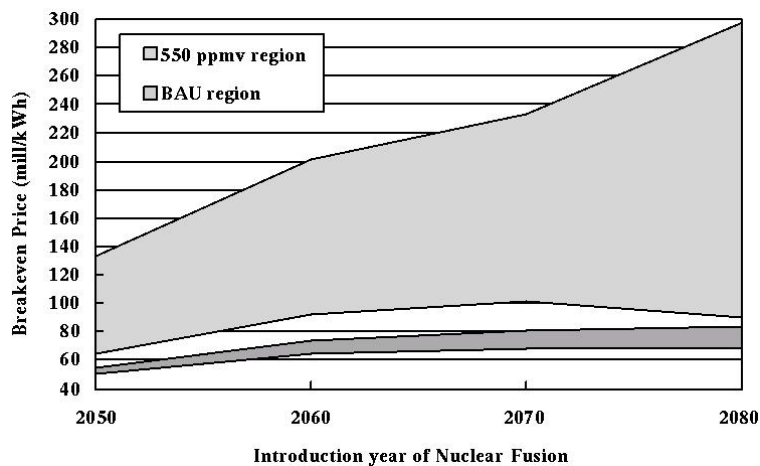


Figure 2.2: Breakeven price as a function of nuclear fusion introduction year for 550 ppmv of CO₂ constraint case and no CO₂ constraint case (business-as usual, BAU case)

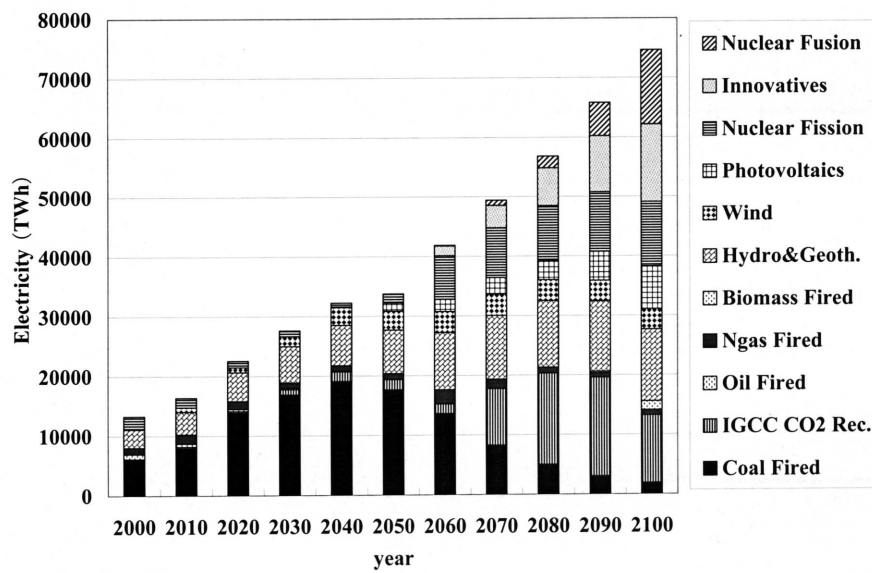


Figure 2.3: Nuclear fusion's share of electricity assuming a 550 ppmv CO₂ concentration constraint, a breakeven price of 65 mill/kWh is assumed for the nuclear fusion

2.2 Analysis Method of Plasma Performance

2.2.1 Outline of the fusion power plant system analysis code (FUSAC)

The requirements for a tokamak reactor to demonstrate net electric power generation are investigated with the database derived from the **F**Ution power plant **S**ystem **A**nalysis **C**ode (FUSAC)[2-8]. This system code is based on the CRIEPI cost assessment code (CCA code)[2-9, 2-2], which was used to clarify quantitatively that β_N was the most effective parameter to reduce the COE of a tokamak reactor[2-2]. The FUSAC consists of three main parts. The first part is a 0D plasma analysis program based on the ITER Physics Design Guidelines[2-10]. The second is a simple engineering design program to determine the shape of TF coil, the position and width for the components of the tokamak reactor (blankets, shields, central solenoid coils, and bucking cylinder), and so on. The engineering design model is based on ref. [2-11]. The last part is an economic analysis program for the designed reactor based on Generic Magnetic Fusion Reactor Model (Generomak Model)[2-12]. The FUSAC was improved particularly as for the plasma and engineering design based on the CCA code.

2.2.2 Plasma and power flow model

The plasma parameters are calculated according to ITER Physics Design Guidelines[2-10] and the power flow model is basically provided with Generomak Model[2-12]. The outline of calculations of plasma and power flow is illustrated in Figure 2.4, and the calculation process is briefly described as follows[2-9].

- The main input parameters are the plasma major radius R_p , the aspect ratio A , the safety factor on plasma surface q_ψ , the average plasma temperature T_{ave} , the normalized beta value β_N , and the maximum magnetic field on TF coils B_{tmax} . The magnetic field on magnetic axis B_t is calculated here.
- The total plasma current I_p is derived from q_ψ and B_t . The total beta value $\beta_{tot}(= \beta_{th} + \beta_\alpha)$ are defined by Toroyon scaling[2-13] and its alpha component β_α is estimated according to ref. [2-10]. The plasma volume V_p and its surface area S_p are also calculated here.
- The electron and ion densities, n_e and n_i , are derived from beta value. The fusion

power density p_f is estimated by the average plasma temperature T_{ave} and ion density n_i . The total fusion power P_f is also calculated in this step.

- The bootstrap current I_{bs} is estimated according to ref. [2-10] and, consequently, driven current I_{CD} is calculated. The confinement properties, such as the confinement improvement factor for H-mode HH , and the ratio of Greenwald density limit fn_{GW} are also derived here.
- The current drive power P_{NBI} , the total thermal output P_{th} , and the averaged neutron wall load $P_{\text{w}}^{\text{ave}}$ are calculated in this step. The current drive efficiency of NBI was defined by Mikkelsen-Singer approximation[2-14]. The total thermal output is defined with the neutron and alpha particle component of total fusion power, P_{N} and P_{α} .

$$P_{\text{th}} = M_{\text{n}}f_{\text{N}}P_{\text{N}} + \eta_{\alpha}P_{\alpha} + \eta_{\text{beam}}P_{\text{NBI}}, \quad (2.1)$$

where M_{n} , f_{N} , η_{α} , and η_{beam} are the multiplication factor of neutron energy in blankets, the covering fraction of blanket for the plasma surface, the collecting rate for the energy of alpha particle, and the collecting rate for the NBI input power, respectively. In this study, $f_{\text{N}} = 0.9$, $\eta_{\alpha} = 0.7$, and $\eta_{\text{beam}} = 0.7$ are assumed. It is necessary to design the blanket so as to fix the multiplication factor of neutron energy in the blankets, however, the details of the blankets are uncertain at present. Hence, the conservative value $M_{\text{n}} = 1.1$ are assumed in the present study in consideration of the use of solid breeders, Li_2O , Li_2TiO_3 , or Li_2ZrO_3 , with 100% dense at room temperature[2-15].

- The circulating power $P_{\text{e}}^{\text{circ}}$ is estimated by Generomak Model[2-12] and the gross electric power $P_{\text{e}}^{\text{gross}}$ is also calculated in this step.
- At last, the net electric power $P_{\text{e}}^{\text{net}}$ is obtained.

Each definition of physical and engineering parameters is explained in ref. [2-10] and ref. [2-12], respectively.

This 0D model for plasma property has produced satisfactory results in the ITER design and other reactor designs, when one roughly estimates the operational region for plasma parameters of a tokamak reactor as seen in ref. [2-16]. Of course, the 0D model cannot precisely take several effects into account, such as realistic heating/current drive profile, line radiation loss power localized in the edge region, bootstrap current fraction,

advanced operation with negative shear and so on. Therefore, when the operation point of a reactor design is selected, the detail analysis on plasma performance is additionally required with the specialized analysis code for MHD, transport, and current drive property.

2.2.3 Analysis Conditions of Reactor Technology

The electric demonstration plant for the realization of net electric power generation has to be designed with reasonably foreseeable conditions. In this study, following engineering parameters are considered as the references; the thermal efficiency of electric conversion $\eta_e = 30\%$, the NBI system efficiency $\eta_{\text{NBI}} = 50\%$, and the magnetic field on TF coils $B_{\text{tmax}} = 16\text{ T}$. The maximum magnetic field of TF coils $B_{\text{tmax}} = 16\text{ T}$ with Nb_3Al and the NBI system efficiency $\eta_{\text{NBI}} = 50\%$ are supposed to be attainable in the near future through the R&D in the ITER program[2-17, 2-18]. The thermal efficiency of electric conversion is assumed to be almost the same as that of an usual light water reactor, because the coolant conditions on the test breeding blanket proposed in the ITER program is similar to that of the usual light water reactor[2-19].

In addition to these parameters, the following three conditions are considered in the present study. First, the current drive power P_{NBI} is limited to 200 MW, because of the limit of available NBI ports and the necessity of a small circulating power. In the ITER NBI design, the injection power for a port is 16.5 MW[2-18]. If injection power of 33.0 MW, twice of the ITER design value, becomes possible, the total NBI power of 200 MW requires 6 ports, which is considered as the maximum port number in the present paper. Of course, the NBI power should be as small as possible, but $P_{\text{NBI}} \sim 200\text{ MW}$ is required to sustain the plasma current with the conservative plasma performance. Second, a sufficient space of 1.4 m for the blankets and the shields is maintained, because a tritium breeding ratio larger than 1.0 ($\text{TBR} \geq 1.0$) has to be surely achieved. At last, the plasma current ramp-up is provided with the magnetic flux swing of CS coils. The required magnetic flux Ψ_{ramp} is defined as follows.

$$\Psi_{\text{ramp}} = (L_p + \mu_0 C_{\text{Ejima}} R_p) I_p , \quad (2.2)$$

where L_p , R_p , and I_p are respectively the plasma inductance, the plasma major radius, and the plasma current with the Ejima coefficient $C_{\text{Ejima}} (= 0.45)$ and permeability of vacuum μ_0 [2-16].

These engineering constraints are not absolute, but will depend on the development of engineering elements and plasma operation techniques in the future. When more ad-

vanced parameters are firmly established in the ITER program, such advanced parameters should, of course, be applied. The sensitivity analysis for these engineering conditions are discussed in Section 2.3.3. The parameter ranges of the 0D system analysis are listed in Table 2.1. The maximum major radius is restricted to 8.5 m, similar to that of ITER-FDR[2-20], because of the machine construction cost. Based on the experimental data and the past reactor designs, the ranges of aspect ratio, plasma elongation, plasma triangularity, plasma temperature, and surface safety factor are respectively selected as shown in Table 2.1.

2.2.4 Database for plasma operational points

With extensive analyses by using the fusion power plant system analysis code (FUSAC), a database for about 100,000 operational points has been constructed with the conditions as mentioned in the previous subsection. Those database covers the plasma parameter ranges listed in Table. 2.1. With this database, investigation of the plasma performance required for net electric power generation was carried out. The main elements of the database are plasma performance parameters (β_N , HH , fn_{GW}), plasma configuration parameters (major radius R_p , aspect ratio A , plasma elongation κ , plasma triangularity δ), other plasma parameters (temperature T_{ave} , plasma densities n_e , n_i , plasma current I_p , bootstrap current I_{bs} and so on), and engineering parameters (coil shape and its location, flux supply with CS coils Ψ_{CS} , net electric power P_e^{net} , circulating power P_e^{circ} and so on).

The database also contains economic parameters, such as the cost of electricity and the construction cost. These elements will be applied to the analysis of the economic break-even condition in Section 2.4.

Table 2.1: The parameter ranges of 0D system analysis.

Major radius R_p (m)	5.5~8.5
Aspect ratio A	2.6~4.0
Plasma elongation κ	1.5~2.0
Plasma triangularity δ	0.35~0.45
Plasma temperature T_{ave} (keV)	12~20
Plasma surface safety factor q_ψ	3.0~6.0
Max. magnetic field B_{tmax} (T)	13.0~19.0
Thermal efficiency η_e (%)	30~40
NBI system efficiency η_{NBI} (%)	30~70

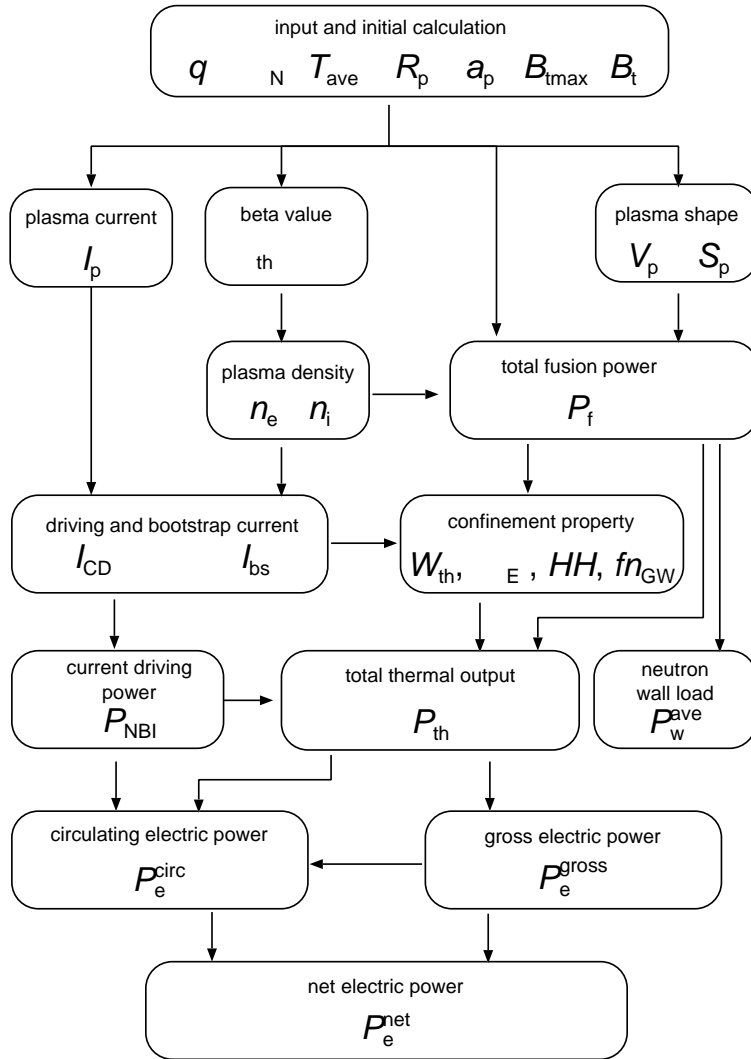


Figure 2.4: Calculation flow for plasma performance and power flow in FUSAC.

2.3 Plasma Performance Required for the Electric Breakeven Condition

2.3.1 The plasma performance required for net electric power and its characteristics

The normalized beta value (β_N), the confinement improvement factor for H-mode scaling (HH), and the ratio of Greenwald density limit (fn_{GW}) are considered as the representative parameters for plasma performance. These parameters are defined as follows.

$$\beta_N = \beta_{\text{tot}} / \left(\frac{I_p}{a_p B_t} \right), \quad (2.3)$$

$$HH = \tau_E / \tau_{E,\text{th}}^{\text{IPB98}(y,2)}, \quad (2.4)$$

$$fn_{GW} = n_e / n_{GW}, \quad (2.5)$$

where I_p , a_p , B_t , and n_e are the total plasma current, the plasma minor radius, the toroidal magnetic field on the magnetic axis, and the averaged electron density, respectively. The scaling law of the energy confinement time for H-mode $\tau_{E,\text{th}}^{\text{IPB98}(y,2)}$ is defined as[2-21]

$$\tau_{E,\text{th}}^{\text{IPB98}(y,2)} = 0.0562 I_p^{0.93} B_t^{0.15} P^{-0.69} \bar{n}_{19}^{0.41} M^{0.19} R_p^{1.97} \epsilon^{0.58} \kappa^{0.78}, \quad (2.6)$$

where P , \bar{n}_{19} , R_p , M , ϵ , and κ are the loss power (MW), the line average density (10^{19}m^{-3}) the plasma major radius (m), the fuel mass number (amu), the inverse aspect ratio, and the plasma elongation, respectively. The definition of Greenwald density limit is[2-22]

$$n_{GW} = I_p / \left(\pi a_p^2 \right). \quad (2.7)$$

As for these plasma performance parameters, the requirements for a tokamak reactor to generate net electric power will be investigated[2-8, 2-23].

The plasma performance parameters (β_N , HH , fn_{GW}) required for $P_e^{\text{net}} = 0$ MW, 400 MW, and 1000 MW are respectively plotted in Figures. 2.5. These results assumed $B_{\text{tmax}} = 16$ T, $\eta_{\text{NBI}} = 50$ %, $\eta_e = 30$ %, $P_{\text{NBI}} \leq 200$ MW, $\kappa = 1.9$ and $\delta = 0.45$. The electric break-even ($P_e^{\text{net}} = 0$ MW) condition for normalized beta indicates the range of $1.2 \leq \beta_N \leq 2.7$ as shown in Figure 2.5 (a1). The width of β_N plots for each net electric power results from the major radius mainly, that is, the plots for $\beta_N = 1.2$ and $\beta_N = 2.7$ in case of $P_e^{\text{net}} = 0$ MW correspond to $R_p = 8.5$ m and $R_p = 6.0$ m, respectively. For $P_e^{\text{net}} \sim 1000$ MW, $\beta_N \geq 3.0$ is required.

In this study, the NBI current drive power is restricted to 200 MW. When this restriction is changed, the requirement for a tokamak reactor to generate net electric power will be also changed. The dependence of the β_N requirement on the P_{NBI} restriction for $P_e^{\text{net}} = 1000$ MW is shown in Figure 2.5(a2). As the restriction of NBI power increases from $P_{\text{NBI}} \leq 100$ MW to $P_{\text{NBI}} \leq 300$ MW, the lower limit of operational region of β_N is reduced from $\beta_N \sim 3.5$ to $\beta_N \sim 2.8$. $P_{\text{NBI}} \sim 300$ MW may become practical in the future, but the following results are provided under the condition of $P_{\text{NBI}} \leq 200$ MW, because of the engineering consideration about the NBI port number discussed in section 2.2.

Regardless of net electric power P_e^{net} , it should be noted in Figure 2.5(b1) that at least $HH \geq 0.8$ is required for net electric power generation with the restriction of $P_{\text{NBI}} \leq 200$ MW. The operational range of $P_e^{\text{net}} = 1000$ MW apparently shrinks in the region of $HH \geq 1.5$ in comparison with that of $P_e^{\text{net}} = 0,400$ MW, because the HH operation points of $P_e^{\text{net}} = 1000$ MW with $HH \geq 1.5$, which have a large β_p and a small plasma current, results in a larger bootstrap current than the total plasma current. Therefore, such operation points with a large bootstrap current fraction beyond unity are excluded in the present analysis. When an advanced plasma is considered for a reactor design, *e.g.* as discussed in the CREST($\beta_N \sim 5.0$ and $f_{\text{bs}} \sim 0.8$)[2-24], the application of the present result should be carefully made, because the 0D plasma model used in the present paper cannot precisely deal with the advanced operation with negative magnetic shear. The operational region of HH also has the dependence on P_{NBI} restriction. The dependence of the HH on P_{NBI} restriction required for $P_{\text{NBI}} = 1000$ MW is shown in Figure 2.5(b2). According to this figure, the larger the restriction of P_{NBI} , the lower the limit of operational region for HH .

A large fn_{GW} is required as P_e^{net} becomes large as shown in Figure 2.5 (c), and this tendency is also similar to that of β_N . The electric break-even ($P_e^{\text{net}} = 0$) condition is provided with the fraction of Greenwald density limit of $0.3 \leq fn_{\text{GW}} \leq 1.1$. When $P_e^{\text{net}} = 1000$ MW is aimed at, at least $fn_{\text{GW}} \geq 0.9$ is required. The effect of the restriction of P_{NBI} on the operational region of fn_{GW} also exists as shown in Figures. 2.5(a2) and (b2), but it is not seen so clearly for fn_{GW} .

The relationships among plasma performance parameters (β_N , HH , fn_{GW}) are shown in Figures. 2.6. As shown in Figure 2.6 (a), β_N and fn_{GW} have to be increased together in order to increase net electric power. However, in Figures 2.6 (b) and (c), there is not clear relationship between HH and the other parameters, such as β_N and fn_{GW} . On the other hand, it should be noted that there is no operational points in the range of $HH \leq 0.8$. Therefore, the accomplishment of $HH \sim 1.0$ is inevitable for realizing net

electric power from the fusion power plant, under the condition of $P_{\text{NBI}} \leq 200$ MW.

According to Figures. 2.5 and 2.6, the increase in both β_{N} and fn_{GW} is inevitable in order to increase net electric power, but HH does not have such tendency as β_{N} and fn_{GW} . Consequently, the net electric power $P_{\text{e}}^{\text{net}} = 0$ MW requires the simultaneous achievement of $1.2 \leq \beta_{\text{N}} \leq 2.7$, $0.8 \leq HH$ and $0.4 \leq fn_{\text{GW}} \leq 1.1$, under the engineering conditions as mentioned in Section 2.2. It should be noted that the relatively moderate plasma performance of $\beta_{\text{N}} = 1.8$, $HH = 1.0$ and $fn_{\text{GW}} = 0.85$, which corresponds to the ITER reference plasma performance for inductive operational scenario[2-18], has a good potential to achieve the electric break-even condition ($P_{\text{e}}^{\text{net}} = 0$ MW) and has a possibility to obtain $P_{\text{e}}^{\text{net}} < 400$ MW with $R_{\text{p}} \leq 8.5$ m. When $P_{\text{e}}^{\text{net}} = 1000$ MW is aimed at, simultaneous achievement of $\beta_{\text{N}} \geq 3.0$, $HH \geq 1.0$ and $fn_{\text{GW}} \geq 1.0$ is required.

The plasma temperature T_{ave} has an effect on the required plasma performance parameters, especially on fn_{GW} as shown in Figures 2.7, because the plasma density decreases when plasma temperature increases at a constant fusion power. In Figure 2.7 (a), fn_{GW} required for $P_{\text{e}}^{\text{net}} = 0$ MW and 1000 MW decreases with increasing plasma temperature. On the other hand, in Figure 2.7 (b), the normalized beta value required for net electric power does not have a clear dependence on the plasma temperature. As a result, higher plasma temperature is the key to moderate fn_{GW} requirements at constant fusion power. The upper limit of plasma temperature depends on the divertor conditions, because increasing plasma temperature results in excessive heat load on the divertor plates. A careful investigation of divertor conditions is needed to select the upper limit of the plasma temperature. When a plasma temperature $T_{\text{ave}} \sim 20$ keV is permitted, the electric break-even condition is easy to be achieved with $fn_{\text{GW}} < 0.5$ and $P_{\text{e}}^{\text{net}} = 1000$ MW is also attainable with $fn_{\text{GW}} \sim 1.0$, which corresponds to the ITER operational region[2-18].

Generally, the required β_{N} can be reduced by either increasing plasma elongation or toroidal magnetic field. The effect of plasma elongation on the required β_{N} is shown in Figure 2.8. An increase from $\kappa = 1.5$ to $\kappa = 2.0$ results in reducing β_{N} by about 0.5 for both $P_{\text{e}}^{\text{net}} = 0$ MW and $P_{\text{e}}^{\text{net}} = 1000$ MW case. In the system code used here, the plasma beta value is defined by $\beta = \beta_{\text{N}} I_{\text{p}} / (a_{\text{p}} B_{\text{t}})$ and the decrease of the required β_{N} is caused from the increase of plasma current I_{p} , because of an increase in plasma elongation with a constant surface plasma safety factor. When $P_{\text{e}}^{\text{net}} = 1000$ MW is desired, $\beta_{\text{N}} \geq 3.5$, which is considered to be larger than the ideal MHD beta limit[2-13], is required for $\kappa = 1.5$ case. On the other hand, $\kappa = 2.0$ has a possibility to obtain $P_{\text{e}}^{\text{net}} = 1000$ MW with $\beta_{\text{N}} \leq 3.5$. From these results, $\kappa \geq 2.0$, which is considered in the recent design studies of commercial reactors such as CREST[2-24] and ARIES-AT[2-25],

is confirmed as a reasonable goal for tokamak fusion plants. This issue has, however, a very important relationship with the engineering design, i.e., blanket and shield design, control coil location, and so on, because of the positional instability. Accordingly, a careful consideration is required when a plasma elongation $\kappa \geq 2.0$ is selected in a reactor design.

2.3.2 Plasma performance diagram on the energy multiplication factor and fusion power (Q vs. P_f) space

In the previous subsection, the various conditions for a tokamak reactor to demonstrate net electric power are investigated under several engineering conditions. When the first tokamak reactor to demonstrate net electric generation is designed, these results should be taken into consideration. At that time, one of the initial tasks is to select the plasma major radius which has a sufficient capacity to produce the objective fusion power. Therefore, it is essential to comprehend the relationship between the requirement of plasma performance for a given fusion power and a major radius.

Figures 2.9 describe the attainable region with several plasma performances of β_N , HH , and fn_{GW} , on the energy multiplication factor and the fusion power (Q vs. P_f) space for each major radius of $R_p = 8.5$ m, 7.5 m, and 6.5 m. These figures are depicted under the engineering conditions of $P_{NBI} \leq 200$ MW, $\eta_e = 30\%$, $\eta_{NBI} = 50\%$, and $B_{tmax} = 16$ T. Each figure consists of two plots. The one is the plot for net electric power P_e^{net} on Q vs. P_f space. The other is for plasma performance parameters on Q vs. P_f space. The former relationship is evident for given engineering parameters. The latter one is derived in the previous subsection. Simply speaking, Figures 2.9 are superpositions of above two plots. With these figures, brief estimation of the plasma performance required for a tokamak reactor to generate net electric power can be made. The plasma performance line for β_N , HH , and fn_{GW} in Figures 2.9 describes the attainable boundary of respective plasma performance. For example, $fn_{GW} > 1.0$ is always needed for the domain above the line of $fn_{GW} = 1.0$, whereas for the domain below the line it is not. It should be noted that the domain below the line of $fn_{GW} = 1.0$, where all the operational points of $fn_{GW} \leq 1.0$ are contained, includes also operational points with $fn_{GW} \geq 1.0$. Similarly, the other plasma parameter lines shown in Figures 2.9 delineate respective attainable boundaries. In these figures, the operational points for each net electric power only with $P_{NBI} \leq 200$ MW are plotted, for the engineering conditions discussed in Section 2.2.

The attainable region with $R_p = 8.5$ m is depicted on Q vs. P_f space in Figure 2.9 (a). This figure shows that a moderate normalized beta value of $\beta_N \sim 1.5$ has a potential to

achieve $P_e^{\text{net}} = 0$ MW with $HH \sim 1.0$ and $fn_{\text{GW}} \leq 1.0$. When $P_e^{\text{net}} = 600$ MW, which corresponds to $P_f \sim 3000$ MW with $\eta_e = 30\%$, are aimed at with $R_p = 8.5$ m, the required β_N becomes about $\beta_N \sim 3.0$. In Figures 2.9, the two attainable boundaries of fn_{GW} are delineated for plasma temperatures of $T_{\text{ave}} = 16$ keV and $T_{\text{ave}} = 20$ keV. In case of $R_p = 8.5$ m, the condition of Greenwald density limit is more severe than in case of smaller major radius. Specifically, an electric power larger than $P_e^{\text{net}} = 200$ MW cannot be attained with $fn_{\text{GW}} < 1.0$ under the condition of $T_{\text{ave}} \leq 16$ keV. Furthermore, it should be noted that the construction cost for $R_p = 8.5$ m is considered to be expensive.

Figure 2.9 (b) shows that the requirement for β_N to achieve $P_e^{\text{net}} \sim 0$ MW with $R_p = 7.5$ m becomes a little demanding, *i.e.*, $\beta_N \sim 2.0$. This figure implies that the progress of the ITER program as planned at present will enable achieving electric break-even ($P_e^{\text{net}} = 0$ MW) condition with a major radius $R_p = 7.5$ m. In addition, this figure shows that it is possible to attain $P_e^{\text{net}} \sim 600$ MW with $P_f \sim 3000$ MW with $\beta_N \leq 3.5$ which is considered to be the ideal MHD beta limit. This plasma performance of $\beta_N \sim 3.5$ can be examined with ITER.

In case of $R_p = 6.5$ m in Figure 2.9(c), the β_N requirement for $P_e^{\text{net}} = 0$ MW with $R_p = 6.5$ is about $\beta_N \sim 2.5$, which is larger than that of ITER reference parameter. When $P_f \sim 3000$ MW is aimed at with $R_p = 6.5$ m, it is necessary to attain $\beta_N > 3.5$ which may require some stabilizing effects, *e.g.* by using a conducting wall in the blanket. However, if it is possible, its construction cost is considered to be moderate and the perspective for demonstrating an economic performance is relatively easy to obtain.

According to the comparison of Figures 2.9, β_N depends on the major radius R_p . The dependence of the required β_N on R_p corresponds to the width of operational plots for β_N in Figure 2.5(a1). On the other hand, the attainable boundary of HH is almost parallel to the restriction of P_{NBI} , which means that the restriction of P_{NBI} has a great impact on HH . Moreover, Figures 2.9 reveal that improvement in HH at a constant β_N cannot always increase the net electric power. It is also found in Figures 2.9 that the fn_{GW} requirement depends on the plasma temperature. $P_f \geq 3000$ MW cannot be attained with $fn_{\text{GW}} < 1.0$ under the condition of $T_{\text{ave}} \leq 16$ keV.

Taking the above results into account, we found that the major radius $R_p \sim 7.5$ may be reasonable to an ‘electric demonstration plant’ for early realization concept, because both of the electric break-even condition ($\beta_N \sim 1.8$, $HH \sim 1.0$, $fn_{\text{GW}} \sim 0.9$) and $P_e^{\text{net}} \sim 600$ MW condition ($\beta_N \sim 3.5$, $HH \sim 1.2$, $fn_{\text{GW}} \sim 1.0$) can be investigated with ITER[2-26, 2-27]. Furthermore, $P_e^{\text{net}} \sim 1000$ MW with $R_p = 7.5$ m, under the conditions of $\beta_N \sim 3.5$, $HH \sim 1.2$, and $fn_{\text{GW}} \sim 1.0$, may become possible by replacing the blanket

of $\eta_e = 30\%$ with an advanced one with $\eta_e \geq 40\%$. In other words, the perspective for an economic performance may be examined with a single device of $R_p = 7.5$ m.

Of course, the choice of the major radius for an electric demonstration plant depends on the basic policy of the reactor design. In the present study, we adopted the conservative engineering conditions mentioned in Section 2.2. Hence, a different policy from ours may lead to a different suggestion as for the major radius.

2.3.3 Consideration on the engineering conditions

The electric demonstration plant should not be always designed with the conservative engineering conditions, *e.g.*, $\eta_e \sim 30\%$, $\eta_{\text{NBI}} \leq 50\%$, and $B_{\text{tmax}} \leq 16$ T, if one can assume time enough to develop sufficient engineering technologies in addition to the advanced plasma. However, it is also necessary for the electric demonstration plant design to select actually foreseeable engineering conditions, since early construction of the electric demonstration plant just after or during the ITER program is seriously considered recently, as proposed in the Fast Track Approach[2-28, 2-29]. That is why we emphasize the conservative engineering conditions in the present study. At the same time, it is essential for attractive fusion power plants in the future to improve the engineering conditions, such as a high thermal efficiency $\eta_e \geq 40\%$ as proposed in CREST[2-24], ARIES-AT[2-25], and A-SSTR2[2-30]. In this subsection, the effects of engineering conditions are investigated and its contribution to mitigate the plasma performance required for net electric generation will be discussed.

- The effect of thermal efficiency

Improvement in thermal efficiency for electric power plants is preferable to generate net electric power. This issue is applicable not only to fusion power plants but to other electric power plants. It is clear that the improvement in thermal efficiency mitigates the plasma performance conditions required for a certain net electric power. In case of thermal efficiency $\eta_e = 40\%$, the attainable boundaries of each plasma performance on Q vs. P_f space is delineated in Figure 2.10, under the same conditions as in Figure 2.9(b). In comparison with Fig. 2.9(b), the plots of each net electric power for $\eta_e = 40\%$ can be realized with a smaller fusion power than that for $\eta_e = 30\%$. The attainable boundaries of β_N and HH in Figure 2.10 are almost the same as those in Figure 2.9(b). Basically, the difference between Figure 2.10 and Figure 2.9(b) is plots of each net electric power generation.

The electric break-even ($P_e^{\text{net}} = 0$ MW) for $\eta_e = 40\%$ is attainable with $\beta_N \sim 1.5$ and $HH \sim 1.0$, which is less demanding than that is planned to be achieved in the ITER operation scenario. Therefore, when $\eta_e = 40\%$ can be achieved, it becomes possible to design an electric demonstration plant with a major radius $R_p \leq 7.5$ m. On the other hand, the net electric power of $P_e^{\text{net}} \sim 900$ MW with $\eta_e = 40\%$, which corresponds to a fusion power $P_f = 3000$ MW with $Q = 35$, is attainable with $\beta_N \sim 3.5$ and $HH \sim 1.2$. In comparison with the case of $\eta_e = 30\%$ of Fig. 2.9(b), the net electric power increases from 600 MW to 900 MW. This implies that the electric demonstration plant with $R_p = 7.5$ m and $\eta_e = 30\%$ has a promising potential to generate net electric power of $P_e^{\text{net}} = 900$ MW with $\beta_N \leq 3.5$ and $HH \leq 1.2$ by replacing the blanket. Such upgrading capability is one of the merits for a fusion reactor and it should be noted when the development strategy of fusion energy is discussed.

- The effect of NBI system efficiency

It is also important for a fusion reactor to improve the NBI system efficiency for a small circulating power. At present, the NBI system efficiency of $\eta_{\text{NBI}} \sim 30\%$ is supposed to be achievable, if the ITER program is implemented as planned[2-18]. The attainable boundaries of each plasma performance with the same conditions as in Figure 2.9(b), except $\eta_{\text{NBI}} = 30\%$, are shown on Q vs. P_f space in Figure 2.11. The attainable boundaries of each plasma performance is roughly similar to that in Figure 2.9(b). The operation plots of each net electric power for a high Q value near $Q \sim 50$ in Fig. 2.11 are almost the same as those in Fig. 2.9(b). On the other hand, as the Q value decreases, the required fusion power for each net electric power increases more than that of $\eta_{\text{NBI}} = 50\%$ case in Fig. 2.9(b), which results in the increase of the β_N required for each net electric power. The electric break-even condition can not be attained with $\beta_N < 2.0$, as described in Fig. 2.11. In other words, the improvement in η_{NBI} is more important for the low Q reactor to mitigate the β_N required for net electric power than for a high Q power plant. Therefore, a high efficiency NBI system should be developed by construction of the electric demonstration plant with a small Q . Of course, the NBI system efficiency η_{NBI} has an effect on the construction cost of a fusion power plant and the improvement in NBI system efficiency is also important for a commercial reactor with high Q value.

- Selection of high magnetic field

Selection of a high magnetic field in a reactor design is one of the reasonable ways to

improve its economic performance as seen in the design concept of A-SSTR2[2-30]. The effect of increase from $B_{\text{tmax}} = 13$ T to $B_{\text{tmax}} = 19$ T on normalized beta value β_{N} for respective $P_{\text{e}}^{\text{net}}$ is shown in Figure 2.12. In the case of $B_{\text{tmax}} = 13$ T, the operational region of $P_{\text{e}}^{\text{net}} = 0$ MW for $\beta_{\text{N}} \leq 1.8$, which corresponds to the ITER reference parameter, is narrow. Altogether, a reactor design with $B_{\text{tmax}} = 13$ T and $\beta_{\text{N}} \sim 1.8$ requires a relatively large major radius $R_{\text{p}} \geq 8.0$ m for net electric power, but a such large reactor size seems disadvantageous to show attractive perspectives for economic performance as an electric power plant. In addition, the operational region of $P_{\text{e}}^{\text{net}} = 1000$ MW is not achievable under the condition of the ideal MHD beta limit, $\beta_{\text{N}} \leq 3.5$.

With the increase of B_{tmax} from 13 T to 19 T, the minimum value for β_{N} is reduced by about 1.0. On the other hand, each operational region for $P_{\text{e}}^{\text{net}} = 0$ MW, 400 MW, and 1000 MW shrinks in the part of large β_{N} . In the present study, a bucking cylinder and CS coils are located within the central torus region and a sufficient torus space of 1.4 m is kept for accommodating installation of blanket and shield. The reason of shrinking operational regions for $B_{\text{tmax}} = 19$ T case is that magnetic stress on TF, CS, and bucking cylinder becomes too large to ensure the torus space for these structures with a major radius $R_{\text{p}} \leq 7.5$. Consequently, the operation region for each $P_{\text{e}}^{\text{net}}$ for $B_{\text{tmax}} = 19$ T becomes narrow in comparison with the case of $B_{\text{tmax}} = 13$ T. Therefore, the selection of a high magnetic field requires a simplified radial build in the central torus region by adopting advanced techniques. For example, if a technique of current ramp-up without CS coils, which was recently investigated in JT-60U[2-31], is firmly established in the ITER program, a reactor with high magnetic field such as $B_{\text{tmax}} \sim 20$ T may become a practical candidate for an electric demonstration plant or a commercial plant, as proposed in the A-SSTR2 concept[2-30].

2.3.4 The condition of blanket design

The averaged neutron wall load $P_{\text{w}}^{\text{ave}}$ for $P_{\text{e}}^{\text{net}} = 0$ MW, 400 MW, 1000 MW is shown in Figure 2.13. This figure is under the same conditions as in Figures 2.5. The width of each $P_{\text{e}}^{\text{net}}$ is mainly caused from the plasma major radius. The minimum plot of $P_{\text{w}}^{\text{ave}}$ in each $P_{\text{e}}^{\text{net}}$ corresponds to the plasma major radius of $R_{\text{p}} \sim 8.5$. Similarly, the maximum ones correspond to $R_{\text{p}} \sim 6.0$. This figure implies the requirement of materials of the first wall and tritium breeding ratio (TBR). When $P_{\text{f}} \sim 3000$ MW would be aimed at, the material

of the first wall for averaged neutron wall load $1.0 \text{ MW/m}^2 \leq P_w^{\text{ave}} \leq 3.5 \text{ MW/m}^2$ is required. $TBR \geq 1.0$, which has to be surely demonstrated in the electric demonstration plant after ITER, is essential for a fusion power plant. This figure also implies the design condition of the neutron wall load for the breeding blanket for each net electric power level.

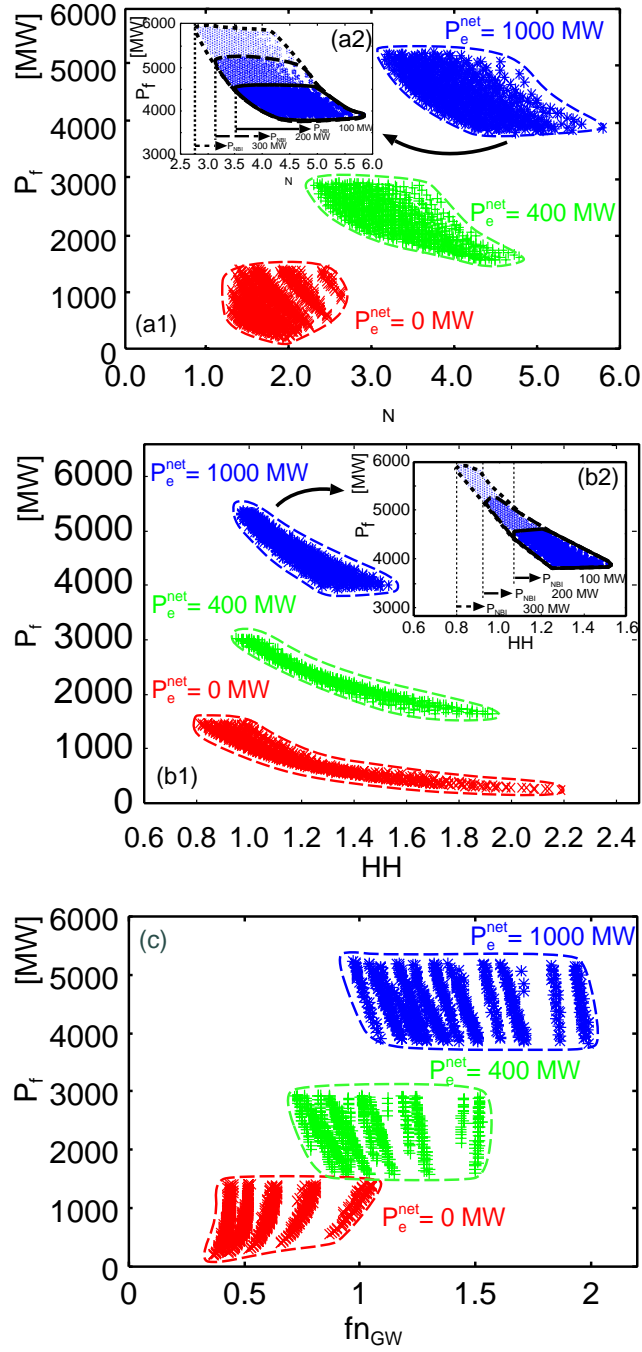


Figure 2.5: Plasma performance required for each net electric power $P_e^{\text{net}} = 0, 400, 1000$ MW. The upper band edge is for $R_p = 6.0$ m while the lower band edge is for $R_p = 8.5$ m. (a1) the required β_N for each net electric power, (a2) the dependence of P_{NBI} restriction on the required β_N for $P_e^{\text{net}} = 1000$ MW, (b1) the required HH for each net electric power, (b2) the dependence of P_{NBI} restriction on the required HH for $P_e^{\text{net}} = 1000$ MW, (c) the required fn_{GW} for each net electric power

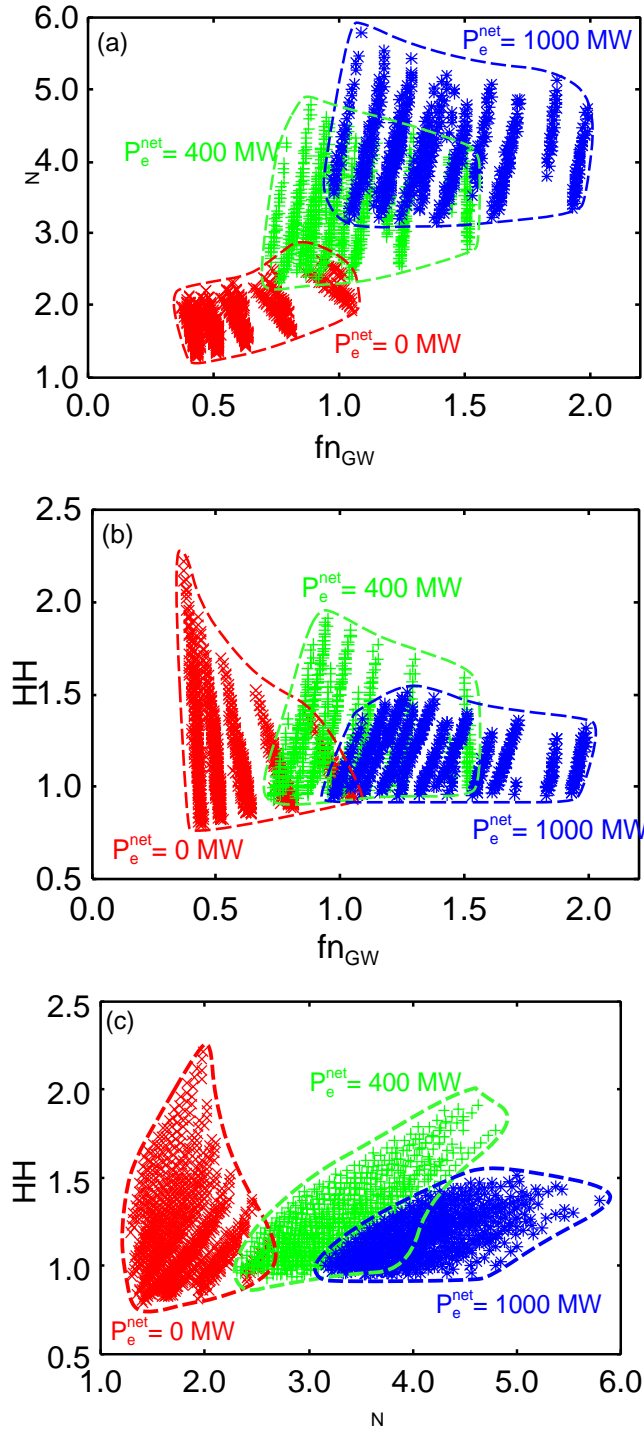


Figure 2.6: The relationship between plasma performance parameters required for $P_e^{\text{net}} = 0, 400, 1000$ MW. The upper band edge is for $R_p = 6.0$ m while the lower band edge is for $R_p = 8.5$ m. (a) the relationship between β_N and fn_{GW} , (b) the relationship between fn_{GW} and HH , (c) the relationship between HH and β_N .

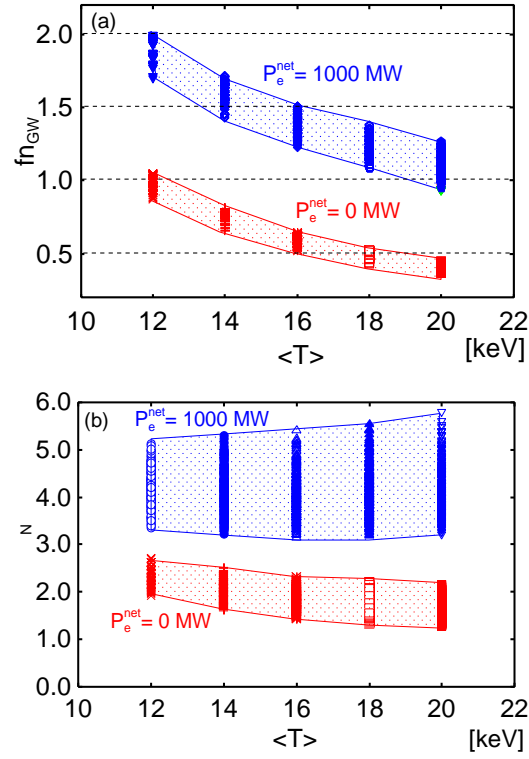


Figure 2.7: The effect of average plasma temperature T_{ave} on (a) $f n_{\text{GW}}$ and (b) β_N for each net electric power $P_e^{\text{net}} = 0, 1000 \text{ MW}$. The upper band edge is for $R_p = 6.0 \text{ m}$ while the lower band edge is for $R_p = 8.5 \text{ m}$.

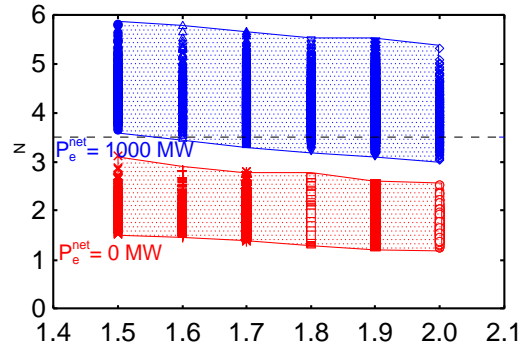


Figure 2.8: The dependence of κ on the required β_N for each net electric power $P_e^{\text{net}} = 0, 1000 \text{ MW}$. The upper band edge is for $R_p = 6.0 \text{ m}$ while the lower band edge is for $R_p = 8.5 \text{ m}$.

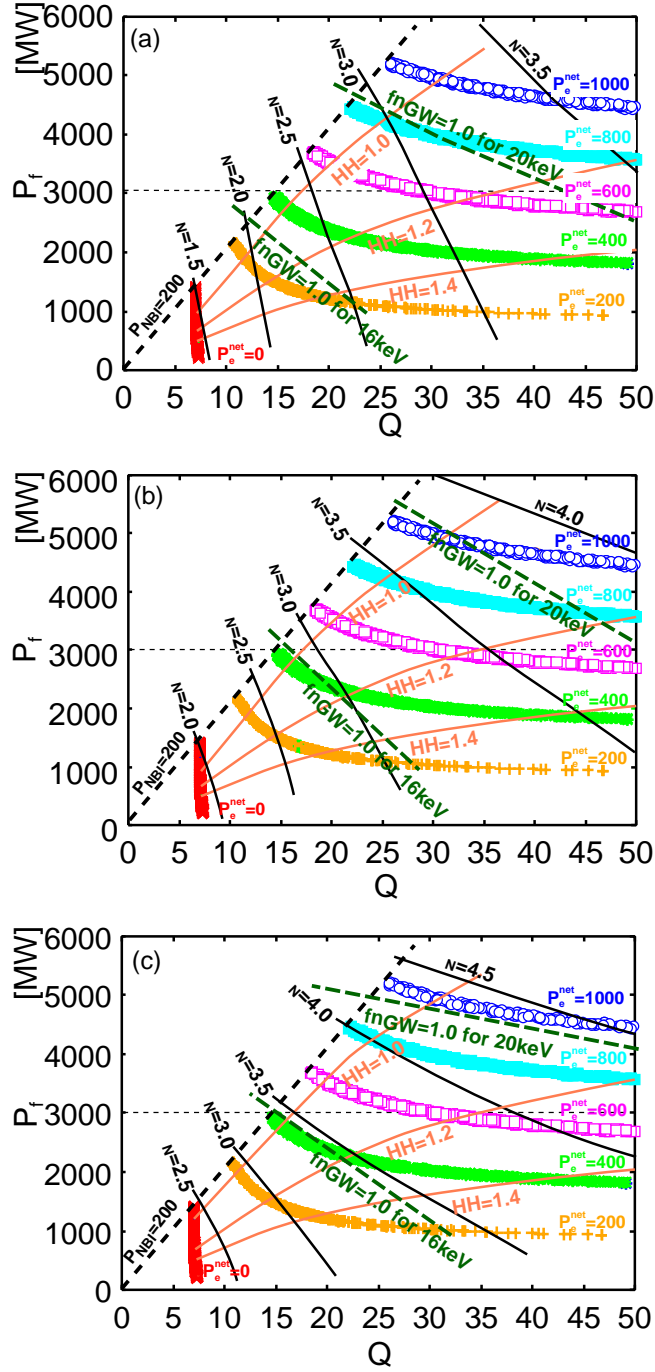


Figure 2.9: Plasma performance diagram on Q vs. P_f space for (a) $R_p = 8.5$ m, (b) $R_p = 7.5$ m, (c) $R_p = 6.5$ m. Each line of β_N , HH , and $f_{n_{GW}}$ delineate the respective attainable boundary. $f_{n_{GW}}$ boundary has two lines for plasma operation temperature $T_{ave} = 16$ keV and 20 keV.

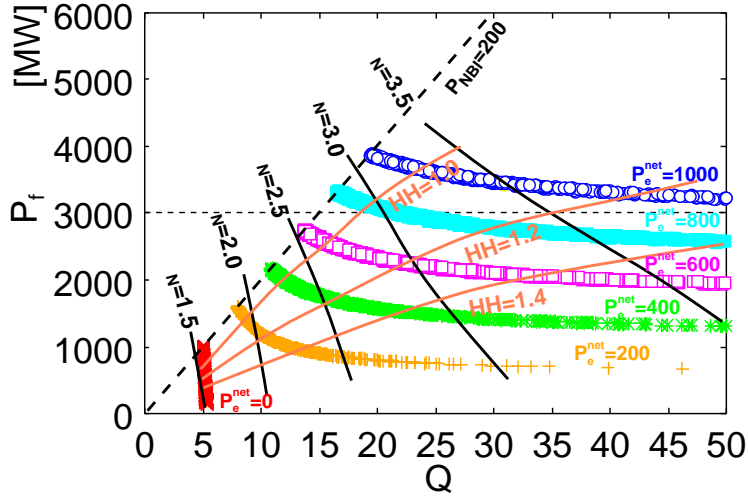


Figure 2.10: Plasma performance diagram on Q vs. P_f space for $R_p = 7.5$ m with the same condition as Figure 2.9(b) except thermal efficiency $\eta_e = 40$ %.

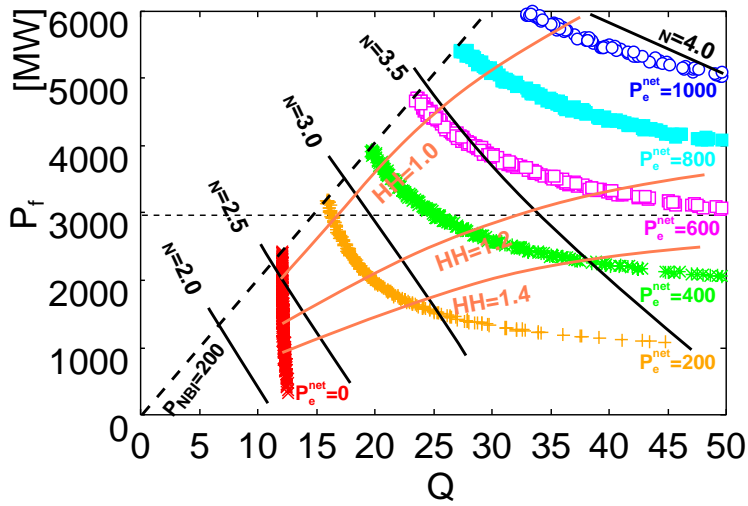


Figure 2.11: Plasma performance diagram on Q vs. P_f space for $R_p = 7.5$ m with the same condition as Figure 2.9(b) except NBI system efficiency $\eta_{\text{NBI}} = 30$ %.

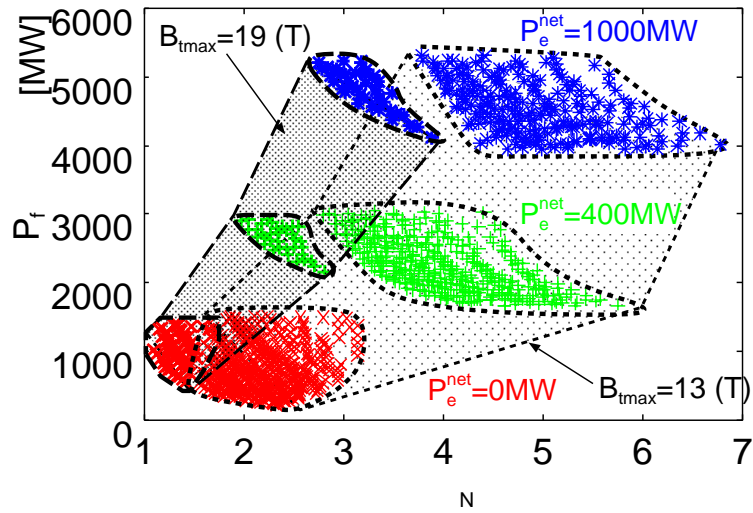


Figure 2.12: The effect of B_{tmax} on the required β_N for each net electric power $P_e^{\text{net}} = 0, 400, \text{ and } 1000 \text{ MW}$. The upper band edge is for $R_p = 6.0 \text{ m}$ while the lower band edge is for $R_p = 8.5 \text{ m}$.

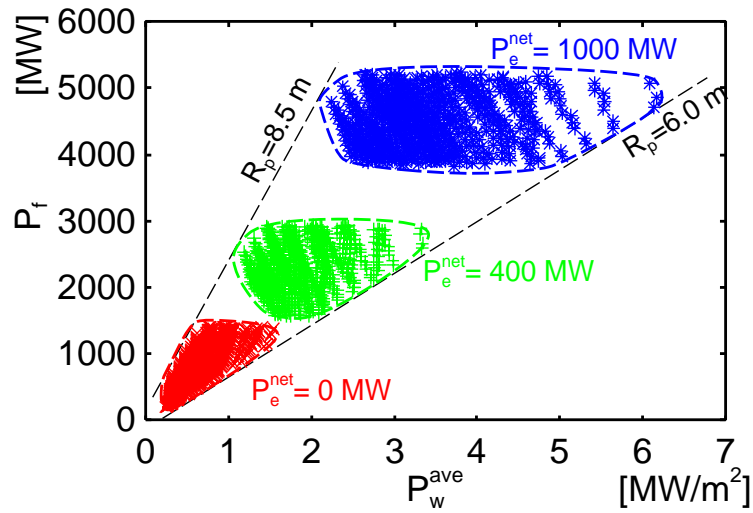


Figure 2.13: P_w^{ave} and P_e^{net} for each net electric power P_e^{net} under the same conditions as in Figures 2.5. The upper band edge is for $R_p = 6.0 \text{ m}$ while the lower band edge is for $R_p = 8.5 \text{ m}$.

2.4 Plasma Performance Required for the Economic Breakeven Condition

2.4.1 Plasma performance required for the break-even price of a world energy scenario

The database constructed by FUSAC as mentioned in Section 2.2 is also applied to this parametric analysis to clarify the plasma performance required to achieve the break-even price of from 65 mill/kWh to 135 mill/kWh in the year 2050 in the world energy scenario. The result of the economic break-even condition for a tokamak fusion power plant with $B_{\text{tmax}} = 16$ T, $P_e^{\text{net}} = 1000$ MW and plant availability 60% is shown in Figures 2.14. Each operational space in Figures 2.14 is composed of the plots for possible operation points. Those operational points are calculated under the same conditions as in the previous section except: (1) thermal efficiency $\eta_e = 40\%$; (2) the feasibility of a simplified radial build without CS coils (which means full non-inductive current ramp up is required in case of without CS coils). In the present study, when there is not space sufficient enough to locate the CS coils with the same B_{tmax} and coil current density J_{tfc} as TF coil, that radial build is designed without CS coils. Note that β_N more than 2.5 has a potential to achieve the upper region of the break-even price in the long term world energy scenario. This β_N value is supposed to be attainable by the ITER advanced plasma performance aiming at the steady state operation[2-18], which implies that the completion of ITER advanced plasma with $\beta_N \sim 3.0$ lead to the possibility of introduction of the fusion energy in the world energy scenario. On the other hand, to achieve the most severe case of the break-even price 65mill/kWh, $\beta_N > 5.0$ with smaller major radius $R_p < 6.0$ m is required. As shown in Figure 2.14 (a), the simplified radial build without CS coil (CS-less region) is required to attain the lower boundary of COE with $5.5 \text{ m} < R_p < 6.5 \text{ m}$. This is because the current density of TF and CS coils is not large enough to make a sufficient space for CS coil in the central torus region. In this result, overall current density of TF coil is $J_{\text{tfc}} \sim 10 \text{ MA/m}^2$, which is almost the same as the ITER design[2-18].

Figure 2.14 (b) shows the HH region required to achieve the break-even price. The higher HH is the lower COE is because of reducing the cost for the current drive system, however, in contrast with β_N , the required HH region is almost the same through the range of $5.5 \text{ m} < R_p < 8.5 \text{ m}$. The most important suggestion in this figure is that there is no path with $HH < 0.9$ to introduction of the tokamak fusion reactor into the long term world energy scenario. The fn_{GW} required to achieve the break-even price (which

is not shown in a figure) has no clear dependence on COE. This is mainly because both the required density and the density limit are decreased as the major radius increases under the condition of the almost the same fusion power.

2.4.2 Dependence of COE on the maximum magnetif field of TF coil

Figure 2.15 shows the dependence of COE on B_{tmax} in case of $5.5 \text{ m} < R_p < 6.5 \text{ m}$. These data reveal that the increase of B_{tmax} is very effective for the decrease of the required β_N under the condition of including a CS-less radial build. On the other hand, the increase of B_{tmax} increases the lowest limit of COE under the condition of the same critical current density. This comes from the increase of the coil volume or the device size, and the lower limit of COE range of 19 T increases up to 90mill/kWh. To get the merit of high magnetic field, the current density of a super conductor also has to be improved. When a current density about 20MA/m² of TF coils is feasible with the same cost as a 10MA/m² coil, the merit of high magnetic field is clearly obtained, that is, the decrease of required β_N with the same COE as 13 T is possible as shown in Figure 2.15. For example, use of a high temperature super conductor with low temperature is effective to increase the current density of TF coils. When the advanced plasma with $\beta_N \sim 6.0$ is possible, a super conductor of 13 T is almost sufficient enough to achieve the lower region of break-even price of 65mill/kWh.

As mentioned in Section 1.2, recent conceptual designs for the commercial reacotr, CREST, ARIES-AT, and A-SSTR2, are carried out in order to get the economic competitiveness. The estimated COEs are in the range of from 50 mill/kWh to 65 mill/kWh as shown in Table 1.1. These COEs have achieved in the lower limit of the break-even price. The CREST design, where $R_p = 5.4 \text{ m}$, $\eta_e = 41\%$, $B_{\text{tmax}} = 13 \text{ T}$ [2-24], has almost the same engineering parameters as is applied in Figure 2.15. The design for the commercial plant CREST is located on the lower boundary of operation region for $B_{\text{tmax}} = 13 \text{ T}$ in Figure 2.15. The ARIES-AT has a higher thermal efficiency $\eta_e \sim 60 \%$, which results in a lower COE about 50 mill/kWh outside the operation region for $B_{\text{tmax}} = 13 \text{ T}$ in Figure 2.15. In case of A-SSTR2, the design criterion is different from above two designs, that is, higher magnetic field and larger electric power output are applied to achieve COE \sim 60mill/kWh. The TF coil current density of A-SSTR2 roughly corresponds to about 20MA/m². In comparison with the operational region for $B_{\text{tmax}} \sim 19 \text{ T}$ with $J_{\text{tfc}} = 20 \text{ MA/m}^2$ in Figure 2.15, lower COE of A-SSTR2 is reasonable because of a higer

thermal efficiency and a plant scale merit. Anyway, Figure 2.15 implies that CREST, ARIES-AT, and A-SSTR2 have a good potential to be introduced into the market in the year 2050 based on the world energy scenario.

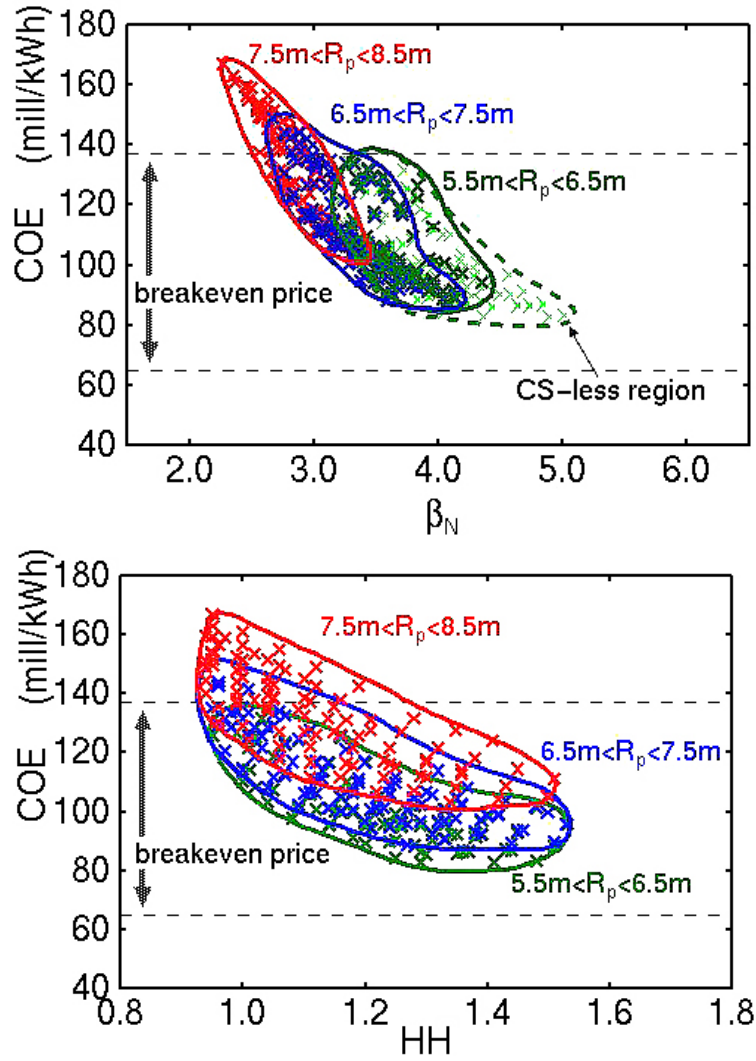


Figure 2.14: (a) Normalized beta value β_N vs. COE for 16 T with the breakeven price of fusion energy. The broken line shows the extension without CS coils (CS-less). (b) Confinement improvement factor HH vs. COE for 16 T with the breakeven price of the fusion energy.

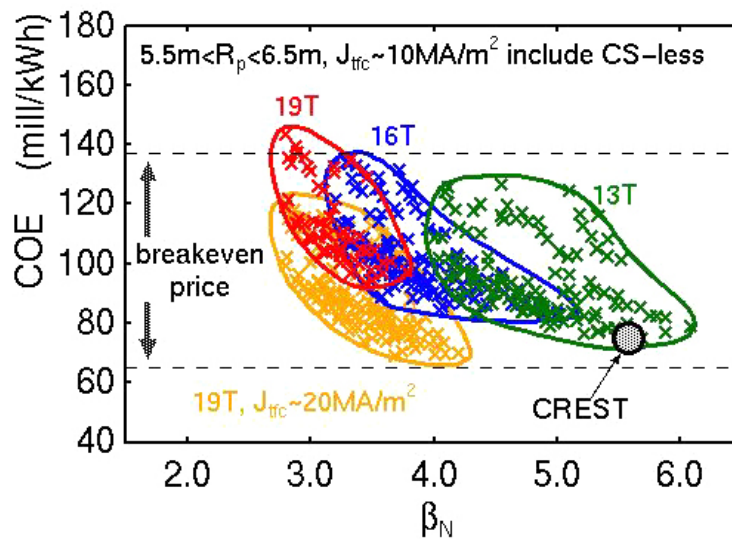


Figure 2.15: Dependence of B_{tmax} on COE for $5.5 \text{ m} \leq R_p \leq 6.5 \text{ m}$ and $J_{\text{tfc}} \sim 10\text{MW/m}^2$ of TF and CS coils. The COE region for 19 T with $J_{\text{tfc}} \sim 20\text{MW/m}^2$ is also shown. The CREST design point is located in the lower limit of the 13 T case.

2.5 Summary

In this chapter, the plasma performance required for a tokamak reactor to achieve the electric break-even condition and the economic break-even condition are investigated. The electric break-even condition requires the simultaneous achievement of $1.2 \leq \beta_N \leq 2.7$, $0.8 \leq HH$, and $0.3 \leq fn_{GW} \leq 1.1$, under the restriction of $P_{NBI} \leq 200$ MW. It should be noted that relatively moderate condition of $\beta_N \sim 1.8$, $HH \sim 1.0$, and $fn_{GW} \sim 0.9$, which corresponds to the ITER reference operation parameters, has a strong possibility to achieve the electric break-even condition. The β_N required for the demonstration of net electric power is mainly reduced with increase of the major radius. The HH required for realizing net electric power is $HH \geq 0.8$ at least, under the condition of $P_{NBI} \leq 200$ MW. Increase in HH with the constant β_N does not always lead to increase net electric power. The condition of Greenwald density limit is found to be mitigated by increase in plasma temperature, but plasma temperature depends on the divertor conditions. The limit of operational plasma temperature needs to be carefully investigated through the divertor analysis. When a high plasma temperature such as $T_{ave} \geq 16$ keV cannot be selected in a reactor design, improvement in $fn_{GW} > 1.0$ should be pursued in the ITER program.

Furthermore, the plasma performance diagram on Q vs. P_f space for a tokamak reactor to generate net electric power is depicted for respective major radius, $R_p \sim 8.5$ m, 7.5 m, and 6.5 m. With these figures, an approximate plasma performance required for net electric power generation is easily estimated when a fusion reactor is designed. According to these figures, we found that the major radius $R_p \sim 7.5$ m is preferable to the electric demonstration plant for early realization of fusion energy as mentioned in Section 1.4, because both of the electric break-even condition and $P_e^{net} \sim 600$ MW condition are supposed to be tested with ITER.

Through the investigations on the sensitivity of the engineering conditions, it is confirmed that improvement in both thermal efficiency and NBI system efficiency are important and $\eta_e \geq 30$ % and $\eta_{NBI} \geq 50$ % should be firmly established for the electric demonstration plant with $R_p \sim 7.5$ m. In addition, it is quantitatively shown that it is necessary for a compact reactor with high magnetic field to compose the radial build by advanced techniques, such as the elimination of CS coils.

The economic break-even condition requires $\beta_N \sim 2.5$ for 135mill/kWh of upper boundary of break-even price and $\beta_N \sim 5.0$ for 65mill/kWh of lower boundary under the conditions of $B_{tmax} = 16$ T, $\eta_e = 40\%$, plant availability 60%, and feasibility of a simplified radial build without CS coil. The demonstration of steady state operation with $\beta_N \sim 3.0$

in the ITER project leads to the prospect to achieve the upper region of break-even price in the world energy scenario. This β_N requirement will be somewhat mitigated with higher B_{max} , however, current density of TF and CS coils has to be simultaneously improved to obtain the clear merit of higher magnetic field.

Reference

- [2-1] R. L. Miller, *Fusion Eng. Des.* **41** (1998) 393
- [2-2] K. Okano *et al*, *Fusion Eng. Des.* **51-52** (2000) 1025
- [2-3] J. G. Delene *et al*, *Fusion Technol.* **39** (2001) 228
- [2-4] K. Tokimatsu *et al*, *Nucl. Fusion* **42** (2002) 1289
- [2-5] K. Tokimatsu *et al*, *Energy Policy* **31** (2003) 775
- [2-6] Contribution of Working Group III to the Third Assessment Report of the Intergovernmental Panel on Climate Change 2001 *CLIMATE CHANGE 2001 Mitigation* (UK: Cambridge University Press) p 25
- [2-7] M. I. Hoffert *et al*, *Science* **298** (2002) 981.
- [2-8] R. Hiwatari *et al*, *Nucl. Fusion* **44** (2004) 106
- [2-9] T. Yoshida *et al*, Development of Cost Assessment Code of Fusion Power Reactors *CRIEPI report No. T94001* (Central Research Institute of Electric Power Industry, Tokyo), 1994 (In Japanese)
- [2-10] N. Uckan and ITER Physics Group ITER Physics Design Guidelines:1989 *ITER Documentation Series No.10* (Vienna: IAEA), 1990
- [2-11] T. Mizoguchi *et al*, Development of tokamak reactor conceptual design code “TRESOCODE” —Conceptual design study of FY86 FER— JAERI-M 87-120 (Naka-machi:Naka Fusion Research Establishment, JAERI), 1987
- [2-12] J. Sheffield *et al*, *Fusion Technology* **9** (1986) 1986
- [2-13] F. Troyon *et al*, *Plasma Phys. Controlled Fusion* **26** (1984) 209

- [2-14] D. Mikkelsen and C. Singer, Nucl. Technol. Fusion **4** (1983) 237
- [2-15] L. El-Guebaly *et al*, Fusion Eng. Des. **38** (1997) 139
- [2-16] Y. Murakami *et al*, J. Plasma Fusion Res. **77** (2001) 712
- [2-17] Y. Takahashi *et al*, IEEE Trans. Appl. Superconduct., **12** (2002) 1799
- [2-18] Technical basis for the ITER final design report *ITER EDA Documentation Series No.24* (Vienna: IAEA) 2001
- [2-19] M. Seki *et al*, Fusion Science and Technology **42**(2002) 50
- [2-20] Technical basis for the ITER final design report(FDR) *ITER EDA Documentation Series No.16* (Vienna: IAEA) 1999
- [2-21] ITER Physics Expert Groups on Confinement and Transport and Confinement Modeling and Database, ITER Physics Basis Editors, Nucl. Fusion **39** (1999) 2175
- [2-22] M. Greenwald *et al*, Nucl. Fusion **28** (1988) 2199
- [2-23] R. Hiwatari *et al*, J. Plasma Fusion Res. **78** (2002) 991
- [2-24] K. Okano *et al* Nucl. Fusion **40** (2000) 635
- [2-25] F. Najmabadi *et al* ARIES-AT: An advanced tokamak, advanced technology fusion power plant steady-state tokamak reactor IAEA-CN-77/FTP2/15 *Proc. 18th IAEA Fusion Energy conf.(Sorrento, October 2000)*(Vienna: IAEA),2000 CD-ROM file, <http://www.iaea.org/programmes/ripc/physics/fec2000/html/node1.htm>
- [2-26] I. Senda *et al*, Advanced Operation Domain in ITER-FEAT, 2I132 *Proc. 4th Fusion Energy Joint Conference.(Osaka, June 2002)*(The Japan Society of Plasma Science and Nuclear Fusion Research, Atomic Energy Society of Japan), 2002 (In Japanese)
- [2-27] M. Shimada *et al*, Nucl. Fusion **44**(2004)350
- [2-28] European Commission Community Research *ITER, THE ROAD TO FUSION ENERGY* (Office for Official Publications of the European Communities,L-2985 Luxembourg) <http://europa.eu.int/comm/research/energy/pdf/fusiontheroadn2.pdf>

- [2-29] H. Bolt, Fast Track Concept in the European Fusion Program *Report of International Symposium for ITER(Tokyo, 24 January 2002)*
<http://www.naka.jaeri.go.jp/keijiban/iter-symposium/report.html> (JAERI, Tokyo, 2002)
- [2-30] S. Nishio, *et al*, J. Plasma Fusion Res. **78**(2000)1218
- [2-31] Y. Takase *et al*, J. Plasma Fusion Res. **78** (2002) 719

Chapter 3

Plasma Design of Demonstration Reactor based on Early Realization Concept

3.1 Introduction

The International Thermonuclear Experimental Reactor (ITER) project is in progress as the experimental reactor stage mentioned in Section 1.4. An ideal commercial fusion power plant is discussed in the conceptual design studies such as CREST[3-1], ARIES-AT[3-2], and A-SSTR2[3-3]. However, the development scenario from the ITER to the proposed commercial plants is not clear yet. To evaluate the critical issues on the plasma performance in each development stage, first of all, it is necessary to structure a development scenario of a fusion power plant. In other words, the conceptual design of an electric demonstration plant consistent with both the ITER and the commercial plant is required. Today, the ITER project is the only one for the experimental reactor. Hence, the design of the electric demonstration plant should be based on the progress in the ITER project. On the other hand, the electric demonstration plant has to provide the outlook for the commercial plant.

Indeed, there are several elements to be considered in the commercial plant design, e.g., economic aspect, safe aspect, and environmental aspect, and so on, but the first priority in the present development status of the fusion energy must be the economic aspect. That is to say, it is essential to develop plasma performance well enough to get the economic competitiveness in the market. Without a reasonable COE of a fusion power

plant, other merits of the fusion energy are not effective. Recent designs of commercial fusion power plants, CREST, ARIES-AT, and A-SSTR2, also focus on the economic aspect, and have compact device sizes in order to realize the small construction cost and competitive COE in the market.

The key for a compact device size is to increase fusion power density of a fusion plasma. The fusion power density (p_f) is roughly proportional to the square of ion plasma pressure ($p_i = n_i T_{ave}$), that is, $p_f \propto p_i^2 = (n_i T_{ave})^2$ [3-4]. This relationship can be rewritten as

$$p_f \propto (\beta_t B_t^2)^2, \quad (3.1)$$

where β_t and B_t are a plasma beta value and toroidal magnetic field on the magnetic axis. Generally, there are two methods for realizing a compact device size with high fusion power density. The first one is the improvement of the plasma performance to increase the plasma pressure, which means the improvement of plasma beta value (β_t). The other is the application of high confinement magnetic field, which means the increase of magnetic field (B_t).

The former method is applied to the designs of CREST and ARIES-AT. In Table 1.1, a high normalized beta value $\beta_N = 5.5$ is applied to CREST and ARIES-AT. According to equation. (2.3), the larger normalized beta value, the larger beta value. This high normalized beta value is achieved by making maximum use of the advanced plasma mode, namely, the reversed shear plasma configuration. The reversed shear configuration has the following characteristics; (1) a good coexistence with high bootstrap fraction[3-5]; (2) good MHD stability regardless of existence of zero shear[3-6, 3-7]; (3) formation of internal transport barrier[3-8, 3-9]. On the other hand, the latter method is applied to A-SSTR2. The normalized beta value of A-SSTR2 is more moderate than that of CREST and ARIES-AT, but magnetic field applied in A-SSTR2 is larger than others as shown in Table 1.1. This high magnetic field is supplied by a high temperature superconductor.

In this study, plasma performance required to realize a demonstration and a commercial plant is focused on, and reactor technology is based on the advancement through the ITER project. The development of high temperature superconductor which is applied to ARIES-AT and A-SSTR2 is outside the scope of the ITER project, and the advanced plasma such as the reversed shear plasma configuration will be examined in the ITER project[3-10]. Hence, the commercial reactor assisted mainly by the advanced plasma will be considered as the main subject in this study.

Roughly speaking, there is no difference of plasma performance between CREST and ARIES-AT as shown in Table 1.1. The plasma configuration applied to CREST and

ARIES-AT is the same configuration, that is, the reversed shear plasma. Hence, the critical issues of plasma performance in CREST is supposed to be also critical ones in ARIES-AT. As for reactor technologies, of course, there is large difference. In the ARIES-AT design, an innovative material of silicon carbide (SiC) composite is applied to realized a extremely high thermal efficiency $\eta_e \sim 60 \%$ [3-2]. In addition, a high temperature superconductor is also applied. On the other hand, a reduced activation ferritic steel is applied in the CREST design, and this material already has a large database and extensive industrial experience. Accordingly, the CREST is considered as the development goal of the fusion energy in this study, and the electric demonstration plant toward the CREST, which is named Demo-CREST[3-11, 3-12], will be carried out. At last, a development scenario of the fusion energy will be structured in order to evaluate the critical issues on the plasma performance in each development stages.

3.2 Design Policy and Conditions of Reactor Technology

The early realization concept as mentioned in Section 1.4 is applied to the design of Demo-CREST. First of all, prior to the discussion on the design policy for Demo-CREST, besides early realization of net electric power generation, the inevitable conditions for the device following ITER will be pointed out. First, it is necessary to generate electric power exceeding the circulating power in a plant scale (electric break-even condition). Second, it is necessary to operate stably and to produce tritium self-sustainably for a certain period so as to demonstrate the backbone of an electric energy source. Last of all, it is necessary to be safe enough to be licensed as a power plant. These conditions are widely accepted as the common ones for the device following ITER. Hence, these conditions are considered to be preconditions for the design of Demo-CREST.

Three guidelines for the design of Demo-CREST are established so as to satisfy the first preconditions mentioned above. Those guidelines are based on the condition that Demo-CREST will be constructed just after or during the ITER program. In other words, the plasma performance and technologies applied to Demo-CREST should be established in the ITER program. The following guidelines for Demo-CREST were chosen:

1. **net electric power output with achievable plasma performance and technologies assured through the ITER program;**
2. **flexible incorporation of the progress of plasma performance and technologies to increase net electric power generation after the construction of Demo-CREST;**
3. **reasonable cost of construction and operation.**

In this study, we consider the first guideline as the most important one. The second guideline means that, for example, an advanced plasma operation and engineering technology such as reversed shear configuration and high thermal efficiency can be installed into Demo-CREST with replacing the blanket system, which is examined in the next chapter. The third guideline leads to choose the major radius as small as possible. In this study, the major radius 8.5 m, which is similar to the previous ITER design[3-13], is considered as the maximum major radius so as to constrain the construction cost.

The design conditions corresponding to the first guideline are listed in Table 3.1. These conditions restrict the plasma operational space of Demo-CREST. The first con-

dition in Table 3.1 is most important for Demo-CREST concerning the plasma performance. Usually, the rated electric power output is one of the critical conditions for optimizing plasma performance in the design studies of fusion power plants. Therefore, the plasma performance applied in past studies is considered as the development goal as seen in CREST[3-1], ARIES-AT[3-2], and A-SSTR2[3-3]. On the other hand, plasma performance is the most critical condition in case of Demo-CREST. Thus, we apply to Demo-CREST the plasma performance expected to be confirmed in the early phase of the ITER program. This is because the role of Demo-CREST focuses on the early realization of net electric power generation just after or during the ITER program.

Second, it is preferable for Demo-CREST to utilize as strong magnetic field as possible because of the conventional plasma performance. In the present study, the Nb₃Al superconducting coil of maximum magnetic field 16 T is considered to be ready for application to fusion reactors in the near future, based on a 13 T-46kA Nb₃Al superconductor completed through the ITER R&D activity in JAERI[3-14].

Third, the thermal efficiency of electric conversion is a critical element concerning engineering technology for Demo-CREST. However, the neutronics experiment of the blanket system for tritium breeding and electric generation is just beginning with a mockup blanket model[3-15], and will be completed in the ITER program. Hence, the thermal efficiency is assumed to be almost the same as that of an usual pressurized water reactor, because the coolant conditions of the test breeding blanket proposed in the ITER program are similar to that of the usual pressurized water reactor[3-16].

Fourth, the NBI system efficiency has a great effect on the circulating power in a power plant. In case of Demo-CREST, more NBI current drive power will be required than that of past reactor studies because of the smaller bootstrap current. Accordingly, the NBI system efficiency for Demo-CREST becomes very important. According to the 30%–40% NBI system efficiency of the ITER design[3-10, 3-17], we consider that a 50% NBI system efficiency can be applied to Demo-CREST by improving the plasma neutralizer cell[3-18].

Fifth, the NBI current drive power is limited, because the limit of available NBI ports and the necessity of a small circulating power. In case of the NBI design for ITER, the injection power for a port is about 16 MW[3-10, 3-17]. If an injection power of 33.0 MW per port, which is twice the ITER design value, becomes possible, a total NBI power of 200 MW requires 6 ports, which is considered as the maximum port number in the present paper. Of course, the NBI power should be as small as possible, but $P_{\text{NBI}} \sim 200$ MW is required to sustain the plasma current with the conservative plasma performance described in the following chapter.

Sixth, plasma current ramp-up is essential to tokamak devices because of the nature of its configuration. In this section, current ramp-up is provided with the magnetic flux swing of CS coils Ψ_{CS} . The required magnetic flux Ψ_{ramp} is evaluated as follows.

$$\Psi_{\text{ramp}} = (L_p + \mu_0 C_{\text{Ejima}} R_p) I_p , \quad (3.2)$$

where L_p , R_p , and I_p are respectively plasma inductance, plasma major radius, and plasma current with permeability of vacuum μ_0 and the Ejima coefficient $C_{\text{Ejima}} (= 0.45)$. The magnetic flux swing provided by CS coils Ψ_{CS} is estimated as

$$\Psi_{CS} \sim 2B_{CS}\pi R_{CS}^2 , \quad (3.3)$$

where B_{CS} and R_{CS} are allowable magnetic field and the radius of CS coil, respectively. The estimation of equation (3.3) implies that the CS coils are fully magnetized before breakdown. Whether such operation for CS coils is possible should be more precisely examined, because the plasma current ramp-up scenario has to be planned under the condition of critical magnetic field and current density for CS and PF coils. Hence, the plasma ramp-up scenario will be discussed in section 3.4.

Table 3.1: Conditions for the initial phase design guideline of Demo-CREST.

-
- (1) Electric break-even condition (the condition of net electric power $P_e^{\text{net}} = 0$ MW) is achieved with the plasma performance similar to the ITER reference operation mode ($\beta_N \sim 1.9$, $HH \sim 1.0$, $fn_{\text{GW}} \sim 0.85$) .
 - (2) Maximum magnetic field 16 T of Nb₃Al is considered according to the prospect obtained in JAERI through the ITER R&D activities.
 - (3) Thermal efficiency 30% is considered on the basis of the design of ITER test blanket modules.
 - (4) NBI system efficiency 50% is considered according to the prospect obtained through the ITER R&D activities.
 - (5) NBI current drive power is limited to 200 MW from the consideration of unit NBI input power and maximum port number on the vacuum vessel.
 - (6) Plasma current ramp-up is provided with the magnetic flux swing of central solenoid coils.
-

3.3 Optimization of Core Plasma for Demonstration Reactor

3.3.1 Optimization method for plasma operation space

The new optimization method of plasma operation point for a fusion reactor was applied in this section, because the design concept of Demo-CREST is different from that of the past design studies of fusion power plants. Specifically, the past design studies of fusion power plants such as CREST, A-SSTR2, and ARIES-AT aimed at clarifying the development goal of physical and engineering parameters. In contrast, the design of Demo-CREST has to be based on the results of the ITER program. That is to say, the progress of ITER leads to directly the design conditions for Demo-CREST. The design constraints of Demo-CREST are supposed to have the complex relationship with each other. In case of past design studies, we can obtain the development goal by investigating how to satisfy all of such constraints. In case of the design of Demo-CREST, we have to follow the inevitable constraints derived from the plasma performance and technologies established through the ITER program, because Demo-CREST will be really constructed just after or during the ITER program. The clearest way to optimize the plasma operation point for Demo-CREST is to pick up the design point, which satisfies all constraints, from all possible design points. At that time, it is important to prepare the database of operation points for fusion power plants, which covers the conceivable range of plasma parameters focused on in the design of Demo-CREST. In this section, the plasma operation point for Demo-CREST is optimized with the systematic database for tokamak fusion power plants. This database is the same one constructed in Section 2.2.

The main characteristics of a tokamak reactor focused on in this section are listed as follows:

- the ELMy H-mode plasma without an internal transport barrier;
- steady state operation with current drive by NBI;
- conventional aspect ratio;
- the central solenoid coil and bucking cylinder system;
- the blanket system based on the test blanket module design in the ITER program.

Indeed, these characteristics are too conservative to achieve the attractive fusion power plants, but the first reactor to generate net electric power just after or during the ITER

program is eventually designed with such conservative characteristics because we consider it reasonable that the design condition of Demo-CREST should be based on the present ITER program experimental plan. Of course, when the advanced plasma and engineering system will be established in the ITER program, such advanced ones should be surely taken into the design of an electric demonstration plant. Hence, a feasibility study depending on the future development level of plasma performance and engineering technology such as ref.[3-19] becomes important, while that is not discussed in this study.

The major elements of this systematic database are listed in Appendix A[3-20], and those symbols are used in this thesis. In addition, this database has engineering and economic elements. The engineering elements are the shape of TF coil, the position and width for the components of the tokamak reactor (blankets, shields, central solenoid coils, and backing cylinder), and so on. These engineering elements sometimes have an important effect on the plasma configuration, i.e., radial build and confinement of alpha particles. Such effects are also briefly validated in FUSAC. The economic elements are also included in the database. For example, the construction cost and the cost of electricity (COE) are calculated in FUSAC. Nevertheless, these economic elements are not emphasized in this section, because the electric demonstration plant should not necessarily optimize economic performance.

A brief outline of optimizing plasma parameters for Demo-CREST is as follows: First of all, the parameter range of the database is selected so as to cover the appropriate range for the device following ITER. Second, the database for the design of a tokamak fusion power plant is constructed with FUSAC. Third, the design criterion for Demo-CREST is determined, and then optimization of its plasma parameters is carried out. At last, the consistency of the optimized results is confirmed with a 2-D MHD and current drive code.

The target range of plasma parameters for the database is based on the present experimental database and the past reactor designs. The major input parameter of the system code FUSAC are a major radius, an aspect ratio, a plasma elongation, a plasma triangularity, a plasma temperature, a plasma surface safety factor, a maximum magnetic field, a thermal efficiency and a NBI system efficiency, and so on. The ranges of these parameter are listed in Table 2.1. How to choose the parameter ranges are explained in Section 2.2. The past conceptual design studies as listed in Appendix B are also referred about these parameter ranges. In addition to these parameters, a sufficient space of 1.4 m for the blanket and the shield is maintained, because the tritium breeding ratio larger than 1.0 ($TBR \geq 1.0$) has to be kept.

With extensive analyses by using FUSAC, a database for about 100,000 operation points has been constructed as mentioned in Section 2.2 We put the design constraints of Demo-CREST on this database, and optimize its operation point.

3.3.2 Main plasma parameters for Demo-CREST

As mentioned in Section 3.2, the priority for the plasma size of Demo-CREST is the electric break-even condition with the same plasma performance as the ITER reference operation mode, i.e., normalized beta value $\beta_N \sim 1.9$, confinement improvement factor for the H-mode $HH \sim 1.0$, the ratio of Greenwald density limit $fn_{GW} \sim 0.85$ [3-10]. The operational space for the net electric power $P_e^{\text{net}} = 0$ MW concerning the major radius and the aspect ratio is depicted in Figures 3.1. The constraints applied here are as follows:

- $\beta_N \leq 1.9$;
- $HH \leq 1.0$;
- $fn_{GW} \leq 0.85$;
- $P_{\text{NBI}} \leq 200$ MW.
- $\Psi_{\text{CS}} \geq \Psi_{\text{ramp}}$;

In Figure 3.1 (a), the total operational space is composed of four spaces corresponding to $q_\psi = 3.5 - 6.0$. In this section, a plasma elongation $\kappa = 1.9$ and plasma triangularity $\delta = 0.40$ are selected. The operation with $q_\psi = 3.0$ cannot be sustained with $P_{\text{NBI}} \leq 200$ MW. The boundary conditions for $q_\psi = 4.0$ are illustrated in Figure 3.1 (b). The left side boundary condition (red line) corresponds to $\beta_N \leq 1.9$. The right side one (green line) corresponds to $P_{\text{NBI}} \leq 200$ MW. The bottom side one corresponds to $\Psi_{\text{CS}} \geq \Psi_{\text{ramp}}$. The conditions for HH and fn_{GW} do not appear explicitly in Figure 3.1 (b). This figure implies the following characteristics:

- The minimum major radius of the operational space is derived from β_N constraints;
- The maximum major radius of the operational space is derived from P_{NBI} constraint;
- The minimum aspect ratio of the operational space is derived from the magnetic flux supply of CS coils for current ramp-up.

Figure 3.1 (a) indicates that the minimum major radius $R_p = 7.0$ m can be applied to Demo-CREST. Considering the design guideline (ii) of Demo-CREST, we choose $R_p = 7.25$ m as the major radius of Demo-CREST. The major radius 7.25 m is preferable for Demo-CREST, because it is possible to have a flexibility for a plasma surface safety factor, that is, total plasma current. Concerning the aspect ratio A , there is not a critical condition, however, we should consider following factors:

- Steady state operation in the present ITER program is planned with $A = 3.4$ and $q_\psi = 5.3$ [3-10].
- Hybrid operation in the present ITER program is planned with $A = 3.1 \sim 3.4$ and $q_\psi = 3.1 \sim 3.5$ [3-10].

According to the above ITER experimental plan, we consider $A = 3.1 \sim 3.4$ preferable for Demo-CREST. Furthermore, the commercial power plant CREST, which is designed with $A = 3.4$ and $q_\psi = 4.3$ [3-1]. Hence, we conclude that $A = 3.4$ is best, because it is the same aspect ratio as ITER steady state operation and CREST. Another advantage of $A = 3.4$ is that it can take almost both $q_\psi = 4.3$ for CREST and $q_\psi = 5.3$ for ITER steady state operation as shown in Figure 3.1(a). In addition, the major disruption, which should not happen in a power plant, is not likely to happen in this $q_\psi = 4.0 \sim 5.0$ range[3-21].

The next task is to examine the attainable range of net electric power with major radius 7.25 m and aspect ratio 3.4. Briefly speaking, free boundary ideal MHD limit, that is, $\beta_N \leq 3.5$, can be roughly examined in ITER. Within this β_N range, the range of net electric power was surveyed, and the operation points of $P_e^{\text{net}} = 0$ MW (OP1), $P_e^{\text{net}} = 200$ MW (OP2), 400 MW (OP3) and 600 MW (OP4) are picked up as shown in Table 3.2. A net electric power 600 MW is possible within $\beta_N \leq 3.5$. Corresponding to OP2, OP3, and OP4 of Table 3.2, each operational space of $R - A$ diagram for $q_\psi = 4.0, 4.5, 5.0$ was also depicted in Figures 3.2. It should be noticed that the way to depict Figures 3.2 is different from that of Figure 3.1. In case of Figures 3.2, we selected the plasma performance conditions ($\beta_N, HH, fn_{\text{GW}}$) of Table 3.2 so that the optimized point $(R, A) = (7.25, 3.4)$ of Demo-CREST is included in each operational space of $P_e^{\text{net}} = 200$ MW, $P_e^{\text{net}} = 400$ MW and $P_e^{\text{net}} = 600$ MW. In other words, the plasma performance of OP1 is the design restriction derived from the ITER experimental plan, and that of OP2-OP4 is the arbitrary condition derived from the optimized configuration $(R, A) = (7.25, 3.4)$ of Demo-CREST. With increasing β_N , the operational space for each q_ψ value becomes narrower, but combined operational space of $q_\psi = 4.0, 4.5$ and 5.0 is

almost the same through the increase of net electric power. On the plasma performance diagram[3-20] for the major radius 7.25 m, which is discussed in Section 2.3, these operation points are plotted in Figure 3.3. The ranges of fusion power for OP1-OP4 are from 1005 MW to 3324 MW. When the engineering design for heat removal from the divertor region is taken into consideration, it is preferable to design a fusion reactor with as a low fusion power as possible, because heat removal in the divertor region is the critical issue in a tokamak fusion reactor (This issue will be discussed in Section 3.5). For the small divertor heat load, the maximum fusion power is limited to about 3000 MW for Demo-CREST. Consequently, the increase of net electric power over 600 MW has to be tried with the same fusion power by reducing the current drive power and improving thermal efficiency.

The operation points from $P_e^{\text{net}} = 0$ MW to $P_e^{\text{net}} = 600$ MW of Demo-CREST have been briefly optimized with 0D plasma analysis model. Those operation points have to be confirmed about whether they can be kept stable against major MHD instabilities. In addition, they also have to be confirmed about whether their plasma current can be sustained with under $P_{\text{NBI}} \leq 200$ MW, because the 0D plasma analysis model cannot precisely take several effects into account, such as realistic heating/current drive profile, bootstrap current fraction, advanced operation with negative shear and so on. Usually, one operation point has only to be confirm in case of a commercial plant. On the other hand, every operation point or operation path has to be done in case of Demo-CREST, because plant performance should be improved step by step. As for MHD stability and current profile control, to confirm the consistent operation path from OP1 to OP4 and to advanced plasma toward a commercial plant is the critical issue in the design of Demo-CREST. This issue will be discussed in the next chapter.

Table 3.2: Representative operation points for $(R_p, A) = (7.25, 3.4)$ of Demo-CREST derived with FUSAC.

	OP1	OP2	OP3	OP4
P_e^{net} (MW)	0	200	400	600
β_N (-)	1.85	2.45	2.96	3.36
HH (-)	1.00	1.08	1.08	1.1
fn_{GW} (-)	0.51	0.64	0.77	1.0
f_{bs} (-)	0.27	0.38	0.43	0.54
Z_{eff} (-)	1.7	1.7	2.1	2.1
P_f (MW)	1005	1772	2590	3324
P_{NBI} (MW)	141	140	148	145

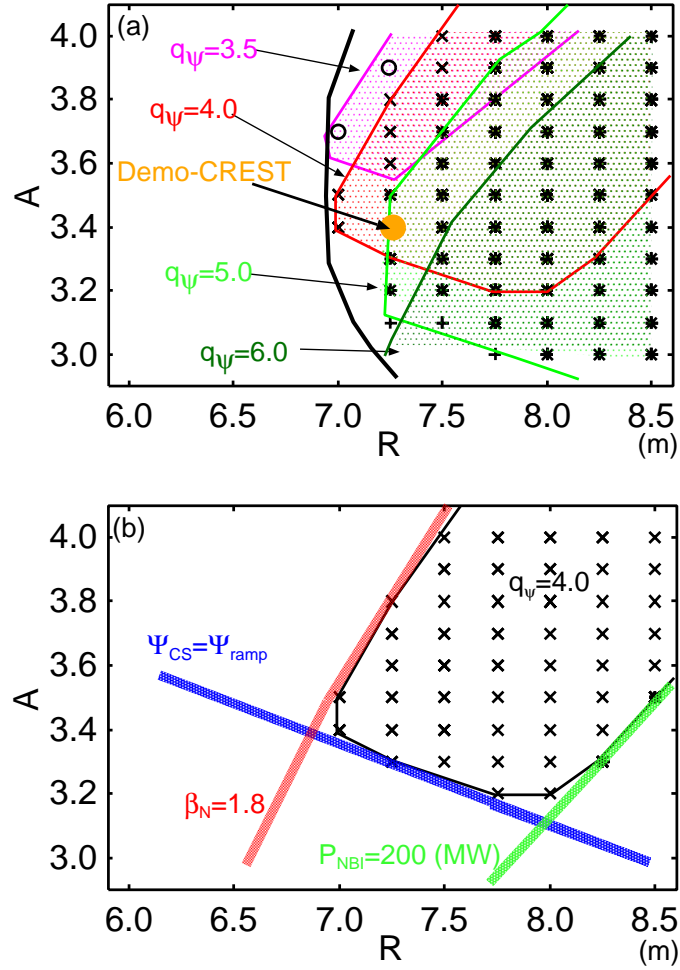


Figure 3.1: (a)Operational space of $P_e^{\text{net}} = 0$ MW with $\beta_N \leq 1.9$, $HH \leq 1.0$, $f_{n_{\text{GW}}} \leq 0.85$, $\Psi_{\text{CS}} \geq \Psi_{\text{ramp}}$ and $P_{\text{NBI}} \leq 200$ MW. Each operational space for $q_\psi = 3.5, 4.0, 5.0, 6.0$ is also described. (b)Boundary conditions for $q_\psi = 4.0$.

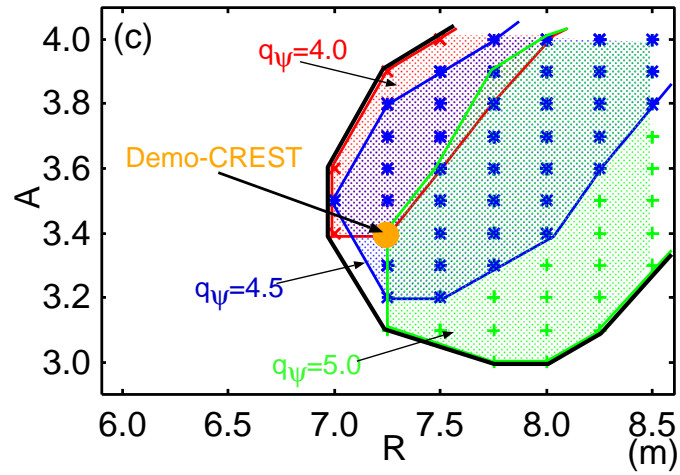
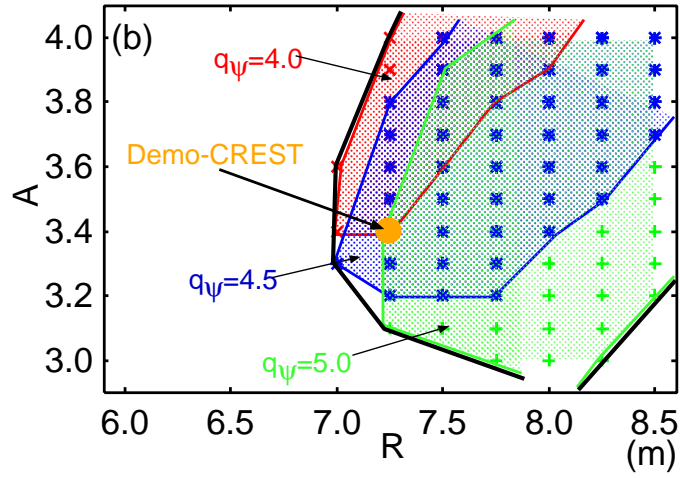
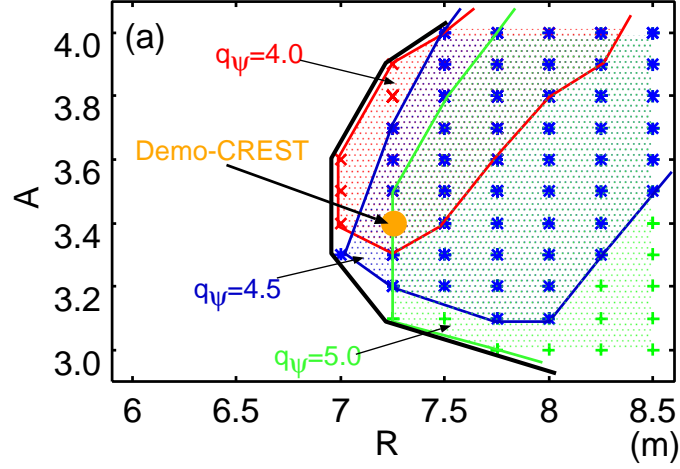


Figure 3.2: Operational space of $q_\psi = 4.0, 4.5, 5.0$ for (a) $P_e^{\text{net}} = 200$ MW, (b) $P_e^{\text{net}} = 400$ MW, and (c) $P_e^{\text{net}} = 600$ MW under the conditions of plasma performance (β_N, HH, fn_{GW}) shown in Table 3.2.

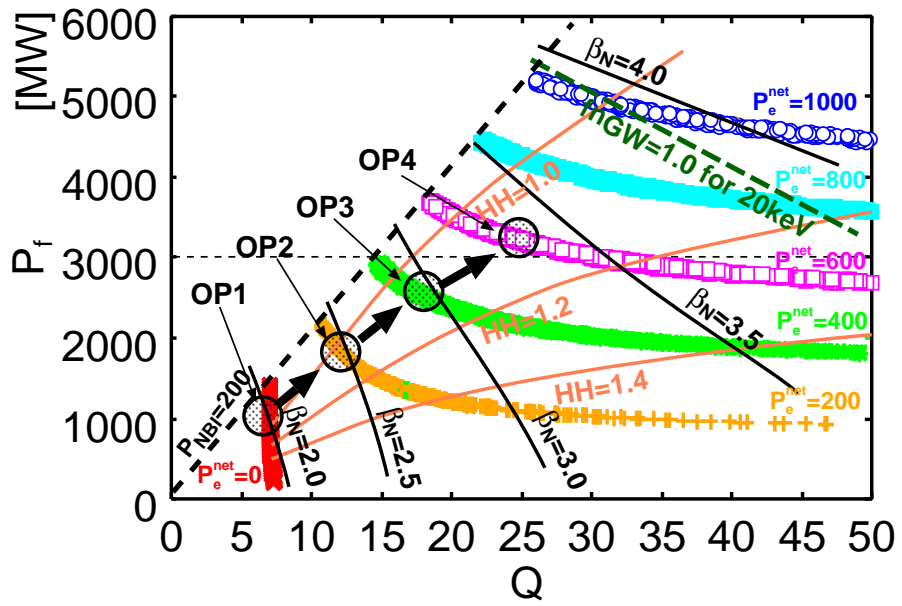


Figure 3.3: Trace of operation point from OP1 to OP4 on the plasma performance diagram.

3.4 Plasma Ramp-up Scenario

In the design of Demo-CREST, current ramp-up is mainly supported by central solenoid (CS) coils, as mentioned in Section 3.2. In equation (3.3), all the available magnetic flux is assumed to be able to use for plasma current ramp-up, however, the ramp-up scenario should be made under the constraints of plasma equilibrium, CS and poloidal field (PF) coil capacity, transition from limiter to divertor configuration, plasma performance, and so on. In this section, the precise analysis for plasma equilibrium and ramp-up scenario with the 2D plasma equilibrium code TOSCA[3-22] is carried out in order to ensure the consistency between the plasma current ramp-up scenario and engineering constraints.

A 16T-Nb₃Al superconductor is applied to Demo-CREST. Since we consider the development of Nb₃Al with higher critical current and the increase of structure material in the coil system due to larger magnetic stress than 13T-Nb₃Sn, we assume that the overall coil current density including insulator and structure material is almost the same as the ITER design[3-10]. Accordingly, the overall coil current density of a toroidal field coil and poloidal field coil (central solenoid coil) in Demo-CREST are restricted to 10 MA/m² (15 MA/m²) in the magnetic field 16T. These current densities are the primary critical parameters to be confirmed in the plasma equilibrium analysis.

Because of a small fraction of bootstrap current in Table 3.2, the operation point OP1 has a more peaked current profile than other operation points. Accordingly, the CS and PF coil current of the OP1 becomes larger than other operation points, because the CS and PF coils is considered to be farther from the plasma current. Hence, the OP1 is the most severe among all operation points of Table 3.2 concerning the operation current of CS and PF coils. In this section, we confirm the most severe case of the OP1 as the sufficient condition. From the system code analysis, the radial build of Demo-CREST is obtained, and the present design is shown in Figure 3.4. Based on Figure 3.4, the location of TF, CS and PF coils are decided as shown in Figure 3.5.

The optimized scenario of plasma current ramp-up is shown in Figure 3.6. In this equilibrium analysis, the pressure profile similar to that derived from MHD analysis (which is discussed in the next chapter) is applied. The plasma internal inductance $l_i = 0.85$, which is almost the same as the ITER inductive operation scenario, is assumed. As shown in Figure 3.6, the current ramp-up fully supported by CS coils is not achievable, and non-inductive current ramp-up of 2.4 MA (15% of total plasma current) is required. The current ramp-up ratio for inductive current ramp-up is 1.0MA/sec until plasma current 1MA, and 0.5MA/sec after plasma current 1.0MA. During non-inductive current ramp-

up phase, it is assumed to be 0.25MA/sec in this study, which should be confirmed by the current drive code. The transition from limiter to divertor configuration is completed at about 5.0 sec in Figure 3.6, and plasma cross sections during current ramp-up are delineated in Figure 3.5. The shaded plasma cross section corresponds to the transition from limiter to divertor configuration. In this equilibrium analysis, poloidal coil system is divided into three groups; CS coil group (coil No. #4-#8 in Figure 3.5), divertor coil group (#3 and #9), and PF coil group (#1,#2,#10,#11). Figure 3.7 (a) shows the respective maximum magnetic field experience in the CS coil group, the divertor coil group, and the PF coil group. Figure 3.7 (b) and (c) show the coil current density for each coil. Before breakdown, the initial magnetization of the CS coils is 90 Vs. In Figure 3.7 (a), the maximum magnetic field experience for CS coils around the transition phase from limiter to divertor configuration rises up to about 16 T, which is the design constraint of superconductor coil. This implies that more initial magnetization of CS coils is restricted by the maximum magnetic field experience of themselves. The divertor and PF coils are under the magnetic field experience of 10 T. This means that another superconductor instead of Nb₃Al can be also applied to PF coils. The current densities of the CS, divertor, and PF coils are also within our design condition of 15 MA/m²(for CS coils) and 10 MA/m²(for divertor and PF coils) as shown in Figure 3.7. Non-inductive current ramp-up phase remains to be examined. Recently, the current ramp-up without CS coils was examined in JT-60U, and advanced tokamak plasma with both internal and edge transport barrier was achieved[3-23]. The non-inductive current ramp-up of Demo-CREST is considered not to be difficult, because it is required only after 85% establishment of the operation plasma current.

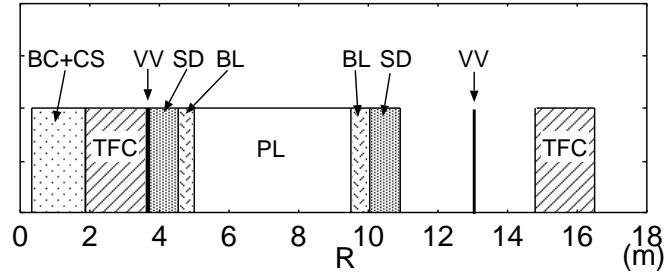


Figure 3.4: Radial build of Demo-CREST. BC+CS : buckling cylinder and central solenoid, TFC : toroidal field coil, VV : vacuum vessel, SD : shield, BL : blanket, PL : plasma.

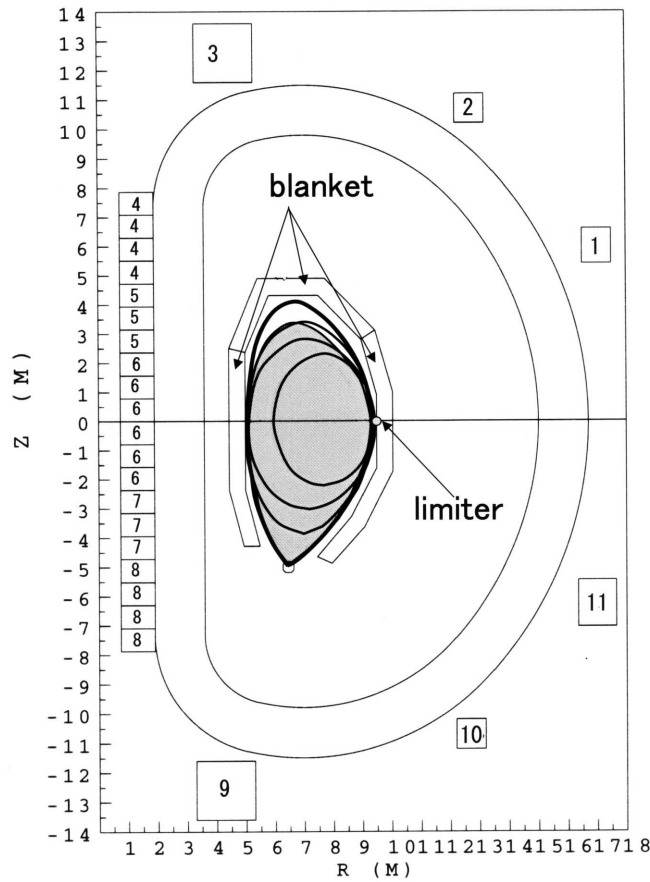


Figure 3.5: Time evolution of plasma shape from breakdown for Demo-CREST and coil location. The shaded plasma cross section corresponds to the transition phase from limiter to divertor configuration.

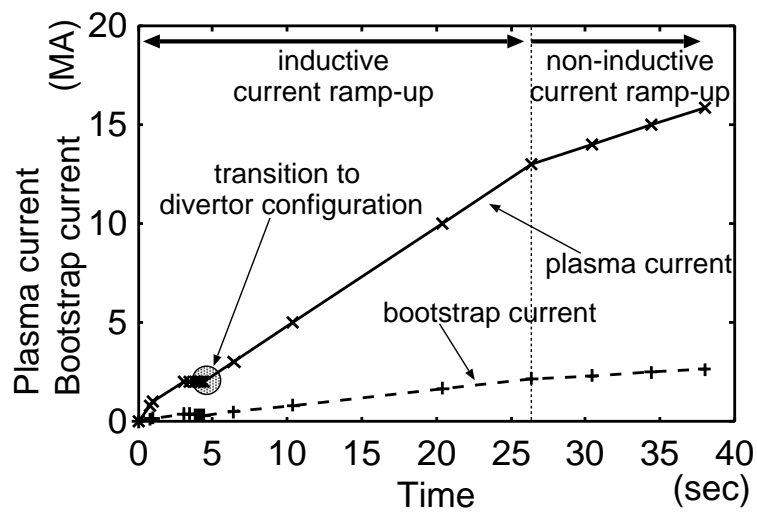


Figure 3.6: Time evolution of plasma current ramp-up for the operation point OP1 of Demo-CREST .

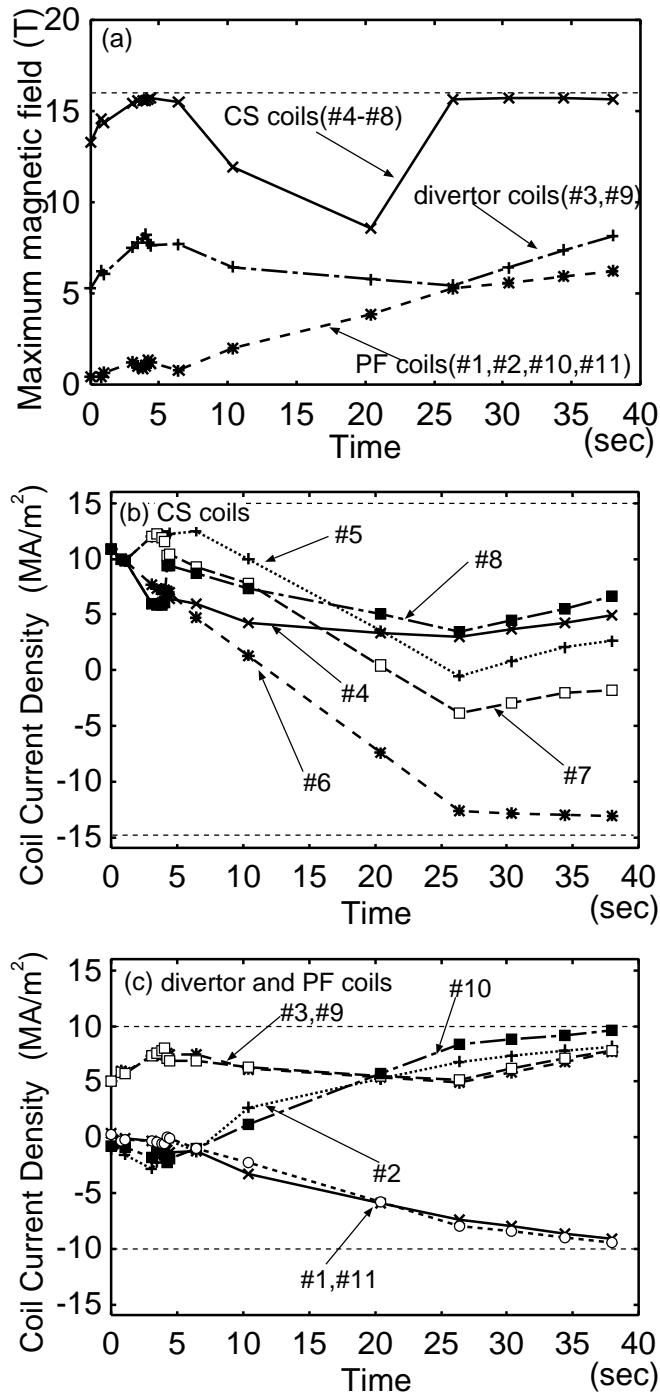


Figure 3.7: (a) The respective maximum magnetic field experience for CS, divertor and PF coil group, (b) current density for CS coils, and (c) current density for divertor and PF coils. The coil number corresponds to that in Figure 3.5.

3.5 Operation Condition of Divertor Plasma

The decrease of heat load on the divertor plate q_{div} is a critical issue for a tokamak fusion reactor. In the ITER design, the peak value of q_{div} in the steady state is restricted to 10 MW/m^2 [3-10]. This limitation of the divertor heat load should be also achieved in the CREST and Demo-CREST design. In the CREST design, the operation condition for the SOL-divertor plasma becomes more severe than the ITER design, because of a smaller major radius and a larger heating power. In order to manage a large thermal power in the CREST design, a small amount of xenon is seeded in the main plasma (0.04%, $Z_{\text{eff}} = 2.2$) and the SOL plasma (0.1%). Under the condition of the upstream SOL density $n_{\text{sol}} = 0.9 \times 10^{20} \text{ m}^{-3}$, which is about half of the core plasma density, total radiation power is estimated at 588 MW (86% of total heating power), and the divertor heat load less than 10 MW/m^2 is achievable[3-1].

The advancement from the ITER divertor to the CREST one is mainly the high-Z impurity seeding for mitigation of the divertor heat load. This approach to the divertor heat load has a large impact not only on the divertor plasma but also on the core plasma. The permeation of impurity into the core plasma results in the degradation of plasma performance. Hence, before the massive divertor analysis with the 2D divertor transport code such as B2-EIRENE, the divertor operation target consistent with the core plasma operation has to be confirmed. An important element for the operation target is the total radiation power required to achieve $q_{\text{div}} \leq 10 \text{ MW/m}^2$. In this section, by using an usual two-point SOL-divertor transport model[3-24], the total radiation power $P_{\text{rad}}^{\text{all}}$ required to achieve $q_{\text{div}} \leq 10 \text{ MW/m}^2$ is investigated in order to prepare for the 2D divertor transport analysis. The precise analysis on the divertor plasma including its effect on the core plasma will be reported in a subsequent submission paper.

First of all, the required radiation power for ITER and CREST is estimated by using the two-point model. In the ITER reference operation, the total heating power of alpha and auxiliary heating is about 120MW[3-10], and the total radiation power required for $q_{\text{div}} \sim 8.7 \text{ MW/m}^2$ with $n_{\text{sol}} = 0.32 \times 10^{20} \text{ m}^{-3}$ is estimated at 83 MW (75% of total heating power). On the other hand, in the CREST design, total heating power is about 710 MW, and the total radiation power required for $q_{\text{div}} \sim 10.0 \text{ MW/m}^2$ with $n_{\text{sol}} = 0.9$ is estimated at 603 MW (85% of total heating power). These results by this two-point model are consistent with the design values of ITER (35MW from the core region and 50 MW from the SOL region) [3-25] and CREST (364 MW from the core region and 224 MW from the SOL region)[3-1].

By using this tow-point model, the total radiation power required to achieve $q_{\text{div}} \leq 10 \text{ MW/m}^2$ for each operation point (from OP1 to OP4) of Demo-CREST is investigated, and the results together with the ITER and CREST results are plotted in Figure 3.8. In this figure, the upstream SOL density of Demo-CREST is assumed to be 2/3 of the core plasma density, which is somewhat mitigated from that of ITER and CREST. In the Demo-CREST operation, the total radiation power has to be increased step by step, and that of OP4 for Demo-CREST finally becomes a little larger than that of CREST. Because the total radiation is supposed to be caused mainly by the line radiation of xenon seeding and mainly in the plasma boundary layer, it is approximately defined as $P_{\text{rad}}^{\text{all}} \propto f_z n_{\text{sol}}^2 I_z(T_{\text{sol}}) R_p^3$, where f_z and $I_z(T_{\text{sol}})$ are the ratio of impurity and its cooling rate, respectively. Accordingly, when the same operation conditions of f_z and $I_z(T_s)$ as CREST are applied by the xenon seeding, about 900MW of radiation power is roughly possible in OP4 of Demo-CREST. With the same way, the possible boundary of radiation power for each operation point for Demo-CREST is delineated in Figure 3.8, and the radiation powers required for all operation points are found to be achievable under the same condition of impurity seeding as CREST.

It should be noted that the effective charge of OP3 and OP4 is almost the same as CREST in preparation for reducing the divertor heat load as shown in Table 3.2. Consequently, the required radiation powers for OP3 and OP4 are considered to be feasible, and $q_{\text{div}} \leq 10 \text{ MW/m}^2$ is achievable. On the other hand, the required radiation powers of OP1 and OP2 are almost marginal to the possible radiation power with the same condition of xenon seeding as CREST, which means that even lower fusion powers of OP1 and OP2 requires xenon seeding as much as or more than CREST. This implies that high-Z impurity seeding technique for the reducing divertor heat load has to be firmly established in the ITER project. Hence, plasma parameters of OP1 and OP2 in Table 3.2 should be more optimized so that higher density with higher effective charge by a high-Z impurity can be achieved. In addition, the upstream SOL density is also the key for the radiation power enough to keep $q_{\text{div}} \leq 10 \text{ MW/m}^2$, because $P_{\text{rad}}^{\text{all}} \propto n_{\text{sol}}^2$. If $n_{\text{sol}} \sim \langle n_e \rangle / 3$, the possible radiation power decrease to 1/4 of that for $n_{\text{sol}} \sim 2\langle n_e \rangle / 3$ and the radiation powers required for all operation points are not achievable. Furthermore, the divertor heat load increases with the decrease of the upstream SOL density. In such case, higher density and lower temperature of plasma operation, which results in a higher current drive power and a higher ratio of Greenwald density limit of the core plasma, should be explored to achieve the required radiation power. In other words, the upstream SOL density is considered as a critical condition of the steady state operation scenario for

small net electric power generation in the demonstration reactor stage.

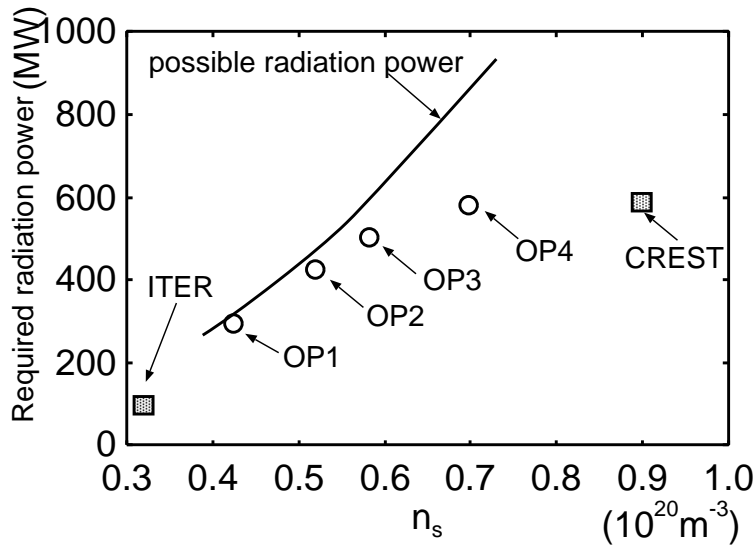


Figure 3.8: Total radiation power required to achieve $q_{\text{div}} \leq 10 \text{ MW/m}^2$ for each operation point (from OP1 to OP4) of Demo-CREST is plotted together with the ITER and CREST design point. The solid line corresponds to the possible boundary of radiation power in case of $n_{\text{sol}} = 2\langle n_e \rangle/3$ case estimated from the CREST design

3.6 Summary

We propose Demo-CREST as an device for early realization of electric generation by fusion energy. The plasma configuration for Demo-CREST was optimized so as to satisfy the electric break-even condition with the reference plasma performance of ITER inductive operation mode. This optimization way is reasonable, although, of course, plasma performance of Demo-CREST is conservative in comparison with the past design studies. Within the plasma performance as planned in the present ITER program, net electric power from 0 MW to 600 MW is possible in Demo-CREST with maximum magnetic field 16 T, thermal efficiency 30 %, NBI system efficiency 50 %, and NBI current drive power restricted to 200 MW. In addition, the development scenario of the physical and engineering technologies of the commercial plant CREST with the electric demo plant Demo-CREST is also suggested by the method of replacing the blanket system.

We also propose the development path with ITER, Demo-CREST, and CREST for early realization of net electric generation by fusion energy, however, we want to emphasize that our proposal is just one example based on the present ITER project. As for this development scenario, the critical issue on plasma performance in each stage is discussed in the following chapter

Reference

- [3-1] K. Okano *et al* Nucl. Fusion **40** (2000) 635
- [3-2] F. Najmabadi *et al* ARIES-AT: An advanced tokamak, advanced technology fusion power plant steady-state tokamak reactor IAEA-CN-77/FTP2/15 *Proc. 18th IAEA Fusion Energy conf.(Sorrento, October 2000)*(Vienna: IAEA),2000 CD-ROM file, <http://www.iaea.org/programmes/ripc/physics/fec2000/html/node1.htm>
- [3-3] S. Nishio, *et al*, J.Plasma Fusion Res. **78**(2000)1218
- [3-4] N. Uckan and ITER Physics Group ITER Physics Design Guidelines:1989 *ITER Documentation Series No.10* (Vienna: IAEA), 1990
- [3-5] C.Kessel *et al*, Phys. Rev. Lett. **72** (1994) 1212
- [3-6] J. M. Green and M. S. Chance, Nucl. Fusion **21** (1981) 453
- [3-7] T. Ozeki *et al*, *Proc. of the 14th International Conference on Plasma Physics and Controlled Nuclear Fusion Research*, Wurzburg, 1992 (IAEA, Vienna,1993), Vol. 2, p.187
- [3-8] F. M. Levinton *et al*, Phys. Rev. Lett. **24** (1995) 4417
- [3-9] E. J. Strait *et al*, Phys. Rev. Lett. **24** (1995) 4421
- [3-10] Technical basis for the ITER final design report *ITER EDA Documentation Series No.24* (Vienna: IAEA) 2001
- [3-11] R. Hiwatari *et al*, “Demo-CREST:Conceptual Study on Fusion Power Reactor for Early Demonstration of electric Generation (1)“, *Proc. of 19th Japan Society of Plasma Science and Nuclear Fusion Research Annual Meeting* 28pC20P, (Inuyama-shi, 2002)

- [3-12] Y. Asaoka *et al*, “Conceptual design of a demonstration reactor for electric power generation”, *Proc. of 20th IAEA Fusion Energy Conference*, IAEA-CN-166/FT/P7-4, Vilamoura 2004.
- [3-13] Technical basis for the ITER final design report(FDR) *ITER EDA Documentation Series No.16* (Vienna: IAEA) 1999
- [3-14] N. Koizumi *et al*, *Cryogenics* **42** (2002) 675
- [3-15] S. Sato *et al*, *Nucl. Fusion* **43** (2003) 527
- [3-16] M. Seki *et al*, *Fusion Science and Technology* **42** (2002) 50
- [3-17] T. Inoue *et al*, *Fusion Eng. Des.* **56-57** (2001) 517
- [3-18] V. M. Kulygin *et al*, *Nucl. Fusion* **41** (2001) 355
- [3-19] W. M. Stacey *et al*, *Nucl. Fusion* **35** (1995) 1369
- [3-20] R. Hiwatari *et al*, *Nucl. Fusion* **44** (2004) 106
- [3-21] ITER Physics Expert Group on Disruptions, Plasma Control, and MHD, ITER Physics Basis Editors 1999 *Nucl. Fusion* **39** 2251
- [3-22] H. Fujieda, K. Shinya, *et al*, JAERI-M 08-256 (Naka-machi:Naka Fusion Research Establishment,JAERI)(In Japanese) 1996
- [3-23] Y. Takase *et al*, *J. Plasma Fusion Res.* **78** (2002) 719
- [3-24] R. Hiwatari *et al*, *Contrib. Plasma Physics* **44** (2004) 76sl
- [3-25] A. S. Kukushkin *et al*, IAEA-CN-94/ITERP/10R *Proc. 18th IAEA Fusion Energy Conf. (Sorrento, October 2000)*(Vienna: IAEA), 2000
- [3-26] N. Inoue *et al*, Feasibility study on inductively operated day-long tokamak reactor, *Nuclear Fusion Supplement (Plasma Physics and Controlled Nuclear Fusion Research 1992)***3** 347, 1993
- [3-27] J. Raeder *et al*, *Safety and Environmental Assessment of Fusion Power (SEAFP), EURFUBRU XII-217/95 (June 1995)* European Commission directorate General XII Fusion Program Brussels, 1995
- [3-28] M. Kikuchi *et al*, *Nucl. Fusion* **30** (1990) 265

Chapter 4

Study on Critical Issues of Tokamak Plasma in Each Development Stage

4.1 Introduction

In the previous chapter, a conceptual design of the electric demonstration plant Demo-CREST was proposed, and the development scenario consistent with the ITER project was structured with the experimental reactor ITER, the electric demonstration plant Demo-CREST, and the commercial plant CREST. In this chapter, several critical issues on plasma performance in each development stage will be analyzed on the basis of development scenario proposed in the previous chapter.

As for plasma performance, the main subjects to be developed in a tokamak-type fusion power plant are listed in Table 4.1. When a fusion power plant is designed, the following subjects have to be solved; First of all, plasma configuration has to be optimized based on a certain design policy in order to achieve an objective electric power (or an objective fusion power). This corresponds to Optimization of plasma configuration in Table 4.1. Second, plasma equilibrium consistent with engineering conditions, such as superconductor coils, has to be confirmed, and plasma ramp-up scenario is also worked out. This corresponds to “Equilibrium and Ramp-up Scenario” in Table 4.1. Third, whether the plasma confirmed by equilibrium analysis is stable and sustainable or not has to be analyzed. This corresponds to “MHD and Current drive” in Table 4.1. Last of all, Whether the stable and sustainable plasma can be consistent with the plasma transport or not has to be confirmed by the precise transport physics. This corresponds to “Transport” in Table 4.1.

In the ITER design, the physics of 'Equilibrium & Ramp-up Scenario' and 'MHD & Current Drive' for ITER reference plasma has been understood well, and the reliable prediction is possible. Only 'Transport' phenomena has not been understood well enough to predict the transport property of ITER. Hence, this 'Transport' subject is the critical issue in ITER. In Sections 4.2-4.4, following three topics for Transport are discussed; (1) transport model for core plasma region; (2) H-mode transition modeling for core-edge boundary region; (3) simple transport modeling for edge plasma region.

In the Demo-CREST design, the critical issue is considered as 'MHD & Current Drive' at present, because the electric demonstration plant Demo-CREST has a unique mission. While a commercial reactor usually has a rated operation point, the electric demonstration plant such as Demo-CREST requires a operation path from ITER-like plasma performance to advanced plasma one in order to achieve the outlook for the commercial power plant. Establishment of this operation path is considered as one of the missions of the electric demonstration plant. Hence, the confirmation of operation path consistent with MHD stability and current profile alignment by single NBI system is the critical issue. In Section 4.5, 'MHD and Current Drive' analysis for the operation path from ITER-like plasma to CREST-like one is carried out.

The CREST design corresponds to the final stage of the fusion energy development, and plasma performance should be improved as high as possible. As seen in the designs of CREST and ARIES-AT, high plasma elongation more than 2.0 is required for high plasma performance. On the other hand, pursuit of high performance plasma by high elongation makes the plasma operation difficult. In Section 4.6, operational condition of plasma elongation and current profile for 'Ramp-up Scenario' is discussed.

Table 4.1: Main subjects to be developed in a tokamak fusion power plant. “ ” is discussed in this thesis, and “ ” is considered as the critical issue in this chapter (corresponding section is denoted).”—” is already completed, while ”×” is not completed yet.

	ITER	Demo-CREST	CREST
Optimization	-		-
Equilibrium & Ramp-up Scenario	-		(Sec. 4.6)
MHD & Current Drive	-	(Sec. 4.5)	-
Transport	(Sec. 4.2— 4.4)	×	×

4.2 Core Plasma Transport Analysis

4.2.1 Dimensional transport property

Prediction of the energy confinement performance for a fusion power plant is one of the most important issues, when we design a fusion reactor. Based on accumulated experimental data of many tokamak devices, several empirical scalings of the energy confinement time have been proposed [4-1, 4-2], and applied for the evaluation of an energy confinement time of the next generation tokamak device such as ITER. Several transport models have been proposed to explain the anomalous transport in tokamak plasma, and have succeeded to simulate the experimental data in some cases. However, comparison between experiments and theory seems not to be sufficient.

Through the dimension analysis, it is found that the transport coefficient χ is described by several non-dimensional parameters as follows[4-3];

$$\chi = \chi_B (\rho^*)^\alpha F(\beta, \nu^*, q, \dots) , \quad (4.1)$$

where $\chi_B = T_e/eB$ is the Bohm diffusion coefficient. Here ρ^* is a normalized minor radius, defined by $\rho^* = \rho_s/a$, where ρ_s is a Larmor radius and a is a plasma minor radius. Independent variables of the function F are non-dimensional parameters such as beta value of $\beta \sim nT/B^2$, normalized collision frequency of $\nu^* \sim qn/T^2$, the safety factor q and so on. In the present experiments we have achieved these non-dimensional parameters equivalent to those of fusion reactors, except for the ρ^* value. Since the ρ^* value of the reactor plasma is quite smaller than that of present experiments, it is quite important to examine the dependence of the transport coefficient on the ρ^* value.

The power of ρ^* on the thermal diffusivity in equation (4.1) is denoted with α . In the case of $\alpha = 1.0$, it is called Gyro-Bohm diffusion, where turbulence with the short wavelength in the range of the Larmor radius might be excited. While in the case of $\alpha = 0$, the plasma transport is called Bohm diffusion, where it is inferred that a scale length of the plasma turbulence is in the range of the plasma minor radius. When the thermal diffusivity is highly enhanced due to the stochasticity of the magnetic field, this is called Goldston diffusion ($\alpha = -0.5$).

To study which type of diffusion governs the plasma transport, dimensionally similar discharges (ρ^* -scaling experiments) have been vigorously carried out in many tokamak plasmas, where a pair of plasma discharges with different ρ^* values are carried out and the thermal diffusivity is compared with other non-dimensional parameters kept fixed. Depending on the experimental devices and confinement modes such as L- and H-modes, experimental results have prevailed different features. DIII-D group has systematically studied on ρ^* scaling, where electrons exhibit a Gyro-Bohm characteristics for all confinement modes and parameter regimes, but ρ^* scaling for ions varies with regime [4-4, 4-5]. For H-mode plasmas in low- q regime ions also show a Gyro-Bohm behavior. However, high- q H-mode and low- q L-mode plasmas yield a Bohm scaling, and high- q L-mode plasmas give Goldston scaling for ions. It might be inferred that the difference of the density scale length between L- and H-modes plays an important role, in addition to the effect of the magnetic shear between different q values. JET group has also reported that the scaling is close to the Gyro-Bohm for ELMy H-mode plasmas [4-6]. Similar results has been observed in ASDEX-U plasmas, where the H-mode plasma yields the Gyro-Bohm scaling, and L-mode plasma exhibits the Bohm feature [4-7]. On JT-60U L-mode plasmas, it has been reported that the electron is between Bohm and Gyro-Bohm diffusions, and this is called Weak-Gyro-Bohm diffusion with $\alpha = 0.5$ [4-8].

Many transport models have been developed theoretically and/or empirically [4-9, 4-10]. Intrinsically each transport model itself predicts Bohm or Gyro-Bohm diffusion. However, the results of transport simulation with each model might differ from its intrinsic characteristics, when many factors such as heating profile, convection effect, boundary conditions, electron-ion equipartition and so on are taken into account and incorporated into the transport simulation. For example, H. Nordman, *et al.* have simulated Bohm-type plasmas in JET L-mode with Gyro-Bohm transport model for temperature gradient driven drift waves, and compared with Gyro-Bohm-type plasmas in H-mode [4-11]. They have concluded that a difference of a boundary condition between L- and H-mode has affected on the core transport through the sensitivity of the stability properties of these

drift waves close to marginal stability.

In ρ^* experiments many other non-dimensional parameters except for ρ^* value should be controlled between different discharges as same as experimentally achievable, and plasma density and heating power are employed so as to keep β and ν^* values within 10 - 20 % accuracy. We can easily match non-dimensional parameters related with plasma geometry such as elongation and divertor configuration, but it is quite difficult to control other non-dimensional parameters related to the plasma parameter itself such as the normalized scale length of the temperature gradient L_i^* , the safety factor profile, in addition to the heat deposition profile, the edge temperature and so on. These uncontrolled factors might affect on the transport characteristics, as pointed out by H. Nordman *et al.* Paying much attention on these parameters, we carry out transport simulations with several transport models for dimensionally similar discharges in JT-60U L-mode plasmas, which are stored in the ITER profile database[4-12], and discuss the validity and the applicability of these transport models in this section.

4.2.2 Physical Models

We use 1-1/2 dimensional tokamak transport code[4-13], which solves following transport equations,

$$\frac{1}{V'} \frac{\partial}{\partial t} (V' n) = - \frac{1}{V'} \frac{\partial}{\partial \rho} [V' \Gamma_n] + S_n, \quad (4.2)$$

$$\frac{3}{2} \frac{1}{V'^{5/3}} \frac{\partial}{\partial t} [(V')^{5/3} n_e T_e] = - \frac{1}{V'} \frac{\partial}{\partial \rho} \left[V' \left(Q_e + \frac{3}{2} T_e \Gamma_e \right) \right] + S_e, \quad (4.3)$$

$$\frac{3}{2} \frac{1}{V'^{5/3}} \frac{\partial}{\partial t} [(V')^{5/3} n_i T_i] = - \frac{1}{V'} \frac{\partial}{\partial \rho} \left[V' \left(Q_i + \frac{3}{2} T_i \Gamma_i \right) \right] + S_i, \quad (4.4)$$

where the flux surface is labeled with ρ ($0 \leq \rho \leq 1$), and $V' = dV/d\rho$. The source and loss terms are denoted by S_n for particle and S_e and S_i for electron and ion energies, respectively. The radial fluxes are described by Γ_n for the particle flux and Q_e and Q_i for heat fluxes of electrons and ions, respectively. Here the heat flux is given by

$$Q_j = - \langle (\nabla \rho)^2 \rangle n_j \chi_j \frac{\partial T_j}{\partial \rho} \quad (j = e, i), \quad (4.5)$$

where χ_j is the thermal diffusivity for species j.

In this study, we are mainly paying attention to the thermal transport, and trying to avoid the uncertainty of the particle transport. Here we evaluate the particle flux in the thermal transport equation with experimental data, instead of solving the particle

transport equation given by equation (4.2). In the steady-state the particle flux is given by the integration of the particle source. In NBI experiments on JT-60U plasmas, the particle source originated from the injected neutral beam is dominant, and the neutral flux due to the recycling and gas-puffing is negligibly small at the core plasma region ($r/a < 0.9$). Therefore the integration of the deposition profile of the neutral beam gives the particle flux with a good accuracy.

In divertor plasmas the plasma boundary is defined by separatrix, and in conventional transport simulation the plasma parameters such as plasma density and temperatures at the separatrix are employed as the boundary condition. However, in the neighborhood of the separatrix, transport characteristics is sometimes exhibiting a remarkable difference from that of the core plasma, because many complicated physical mechanisms such as ionization of neutral particles play an important role on the power balance even inside the separatrix. To exclude these phenomena from the transport mechanism of the core plasma, we set the plasma boundary deeply inside the separatrix (*i.e.*, $r/a = 0.9$), and employ the experimental data at this position (such as $n_e(r/a = 0.9)$, $T_{e,i}(r/a = 0.9)$) into the transport simulation.

We employ three transport models; Bohm-type model [4-14], Current Diffusive Ballooning Mode (CDBM) model [4-15, 4-16, 4-17], and Multi-Mode model [4-18]. Here, these models are briefly explained.

(a) Bohm-type model

Bohm-type model is empirically constructed through the analysis of L-mode JET plasmas. The thermal diffusivity is assumed to be the Bohm like diffusivity which is described as

$$\chi_{e,i} = \chi_B F(\nu^*, \beta, q, L_T^*, L_p^* \dots), \quad (4.6)$$

where χ_B is T_e/eB , $\beta \sim nT/B^2$, $\nu^* \sim an/T^2$, $L_T^* = (dT/dr)^{-1}T/a$ and $L_p^* = (dp/dr)^{-1}p/a$. By analyzing JET L-mode plasmas, the function F is empirically determined as,

$$F = C_B q^2 / |L_{T_e}^*|, \quad (4.7)$$

where q is the safety factor and C_B is a constant value to be derived from the analysis of experimental results. The temperature scale length $L_{T_e}^*$ is almost equal to the pressure scale length $L_{p_e}^*$ in JET L-mode plasmas, and replaced by L_{p_e} in the equation (4.7). The thermal diffusivity is eventually described as

$$\chi_e = \frac{|\nabla p_e|}{nB_t} a q^2, \quad (4.8)$$

$$\chi_i = 2\chi_e , \quad (4.9)$$

Here, the thermal diffusivity for ions is assumed to be two times of that for electrons.

(b) Current Diffusive Ballooning Mode (CDBM) model

By introducing the current diffusivity due to the electron viscosity into the Ohm's law equation, the stability for ballooning mode is analyzed. It is pointed out that the ballooning mode becomes unstable even in low beta plasmas, if the mode amplitude and transport coefficients are small. The saturation level of this ballooning instability is determined by the balance of the stabilization effect due to the enhanced thermal diffusivity and the ion viscosity. Detailed analysis gives the thermal diffusivity due to the current diffusive ballooning mode as follows;

$$\chi_{e,i} = F(s, \alpha, \kappa) |\alpha|^{3/2} \frac{c^2}{\omega_{pe}^2} \frac{v_A}{qR} , \quad (4.10)$$

where

$$\hat{s} \equiv \frac{r}{q} \frac{dq}{dr} , \quad (4.11)$$

$$\alpha \equiv -q^2 R \frac{d\beta}{dr} , \quad (4.12)$$

$$\kappa \equiv -\frac{r}{R} \left(1 - \frac{1}{q^2} \right) , \quad (4.13)$$

and the function F is related with the magnetic shear and approximately given by

$$F(\hat{s}, \alpha, \kappa) = \frac{(1 + \kappa)^{5/2}}{\sqrt{2(1 - 2\tilde{s})[1 - 2\tilde{s} + 3\tilde{s}^2(1 + \kappa)]}} , \quad (4.14)$$

where $\tilde{s} = \hat{s} - \alpha$.

(c) Multi-Mode model

This model is constructed from the combination of theoretically derived transport models; trapped electron mode, ion temperature gradient driven mode and resistive ballooning mode.

Tapped electron mode is described as

$$\chi_{e,i}^{TE} = 8.33 F_{e,i}^{TE} F_\beta \left(\frac{r}{R} \right)^{1/2} \frac{\rho_s^2 c_s}{L_{ni}} \left[1; \frac{0.1}{\nu_e^*} \right]_{min} , \quad (4.15)$$

$$F_\beta = \frac{1 + \beta/\beta'_c}{1 + (\beta/\beta'_c)^3} , \quad (4.16)$$

where $\beta' = \partial\beta/\partial r$ and $\beta'_c = \hat{s}/(1.7q^2R)$.

Ion temperature gradient(η_i) mode is described as

$$D_{\eta_i} = \left(\rho_s^2 c_s / L_n\right) \max(\eta_i - \eta_i^{th}, 0) \times \exp[-\min(5L, 4L_{T_i})/L_s], \quad (4.17)$$

$$\chi_e^{ITG} = F_e^{ITG} D_{\eta_i}, \quad (4.18)$$

$$\chi_i^{ITG} = F_i^{ITG} D_{\eta_i}, \quad (4.19)$$

where the threshold function is $\eta_i^{th} = \max(1, 5L_n/R)$.

Resistive Ballooning mode is described as

$$D^{RB} = f_{dia} \Lambda^2 \frac{\beta R q^2 r^2}{\sqrt{2} L_p \hat{s} \tau_R}, \quad (4.20)$$

$$\chi_e^{RB} = F_{e1}^{RB} f_{dia} \frac{\Lambda^{4/3}}{2^{13/6}} \left(\frac{\tau_{hp}}{\langle n \rangle \tau_R}\right)^{2/3} \times \left(\frac{\beta R q^2}{L_p}\right)^{4/3} \frac{v_{th} e r^2}{\hat{s} R} + F_{e2}^{RB} D^{RB}, \quad (4.21)$$

$$\chi_i^{RB} = F_i^{RB} D^{RB}, \quad (4.22)$$

where

$$\Lambda = \frac{2}{3\pi} \ln \left[\frac{256 (\tau_R / \tau_{hp})^2 L_p}{\beta R \Lambda^3} \left(\frac{\hat{s}}{\langle n \rangle}\right)^4 \right] \sim 7.0. \quad (4.23)$$

Numerical coefficients for these modes are summarized in Table 4.2, and in total the transport coefficient is given by the linear combination of these three modes.

4.2.3 Simulation Results for L-mode Discharges

Dimensionally similar discharges are provided from JT-60U L-mode plasmas [4-8]. Typical plasma parameters are summarized in Table 4.3, where two sets of the dimensionally similar discharges with different safety factors ($q_{\text{eff}} = 4.5$ and 6 cases) are listed. Experimental data are chosen at the steady-state phase of these discharges in all cases.

In Figure 4.1, plasma parameters experimentally measured and computationally calculated are shown for #21795 and #21810 discharges, and employed in the transport

simulations. In the core plasma region the dominant particle source is the injected neutral beam. The deposition profile of the neutral beam is calculated, as shown in Figure 4.1, and incorporated into equation (4.2), giving the particle flux Γ at the steady-state. The ion density is estimated with the effective charge Z_{eff} and the fast ion density n_i^f ; *i.e.*, $n_i = (Z - Z_{\text{eff}})/(Z - 1)n_e - n_i^f$. Since the carbon is dominant as an impurity, we set that $Z = 6$, and $Z_{\text{eff}} = 2.5$ with the uniform profile. The fast ion density is derived from the beam deposition and the slowing-down time. Compared to the electron density profile, the ion density profile is quite flat at the plasma central region and is not a smooth profile, because the fast ion population is large at the central region and the calculated profile is slightly fluctuating. Careful attention should be paid in the simulation with the Multi-Mode model, where the scale length of the ion density gradient L_{n_i} is explicitly introduced in the transport coefficients. The assignment of the heating power between electrons and ions are the almost same between two discharges; *i.e.*, $S_e : S_i = 0.44 : 0.56$ for #21795 and $S_e : S_i = 0.41 : 0.59$ for #21810, but a relatively central heating is taking place in #21795 due to the deep penetration of the neutral beam at the low density plasma. The safety factor profile employed in this simulation is calculated by the equilibrium solver as shown in Figure 4.1 (c1) and (c2).

In experiments small sawteeth activities are observed at the central region of the plasma column ($r/a < 0.2$). However, since the effect of the sawtooth on the global confinement seems small, we have not considered the sawtooth model in our simulations. Simulation results with three transport models (Bohm-type, CDBM and Multi-Mode models) are compared with experimental data in Figures 4.2 and 4.3 for four discharges.

Difference between experimental data and simulation results is evaluated with two methods. One is the total stored energies of electrons and ions, by integrating the profile data. The errors defined by $(W_j^{\text{sim}} - W_j^{\text{exp}})/W_j^{\text{exp}}$ are plotted in Figure 4.4, where $j = \text{electron, ion and total}$. The other is the standard deviation between experimental and simulational profiles in Figure 4.5, which is defined as follows;

$$STD_j = \frac{\sqrt{\sum_k (T_j^{\text{sim}}(k) - T_j^{\text{exp}}(k))^2}}{\sum_k T_j^{\text{exp}}(k)} \quad (j = e, i), \quad (4.24)$$

where k is the number of mesh.

Bohm-type model

The electron stored energy is in agreement within $\pm 10\%$ with experimental data. In low q_{eff} plasmas (#21795 and #21810) simulation results show a higher electron temperature than experimental data, but in high q_{eff} plasma (#21796 and #21811) simulation results become smaller than experimental data. In Bohm-type model, it is deduced from equation (4.7) that the global confinement time is proportional to the plasma current. Therefore, in JT-60U L-mode plasmas, it might be suspected that the power of the plasma current in the global confinement time might be weaker than unity, as was shown by a scaling of thermal energy confinement given in ref. [4-8]. Simulation results give ion temperatures lower than experimental data for all cases. If the ion thermal diffusivity is lowered from the twice of electron thermal diffusivity, the simulated ion temperature profile is more agreeable with experimental results.

Current diffusive ballooning mode (CDBM) model

In CDBM model, the simulation results are in agreement with at most 15% error for electron stored energy. Here we should remark that strong peaking of the electron temperature appears at the plasma central region ($r/a < 0.2$) in this model. This might be caused due to the strong dependence of the thermal diffusivity on the pressure gradient (*i.e.*, $\chi \sim (d\beta/dr)^{3/2}$). The disagreement between simulation results and experimental data is quite large for ion stored energy. In all cases the simulation results show remarkably higher ion temperature than experimental data. We should consider the enhancement of the ion thermal diffusivity in this model, because the ion thermal diffusivity is assumed to be same with electron one.

Multi-Mode model

In Multi-Mode model, the electron stored energy is in good agreement between simulation results and experimental data within $\pm 15\%$ error, although the temperature profile seems not to be so smooth function. The electron thermal diffusivity is plotted in Figures 4.6 for #21795, where three modes (TE: trapped electron, ITG: ion temperature gradient and RB: resistive ballooning) are depicted as a function of the minor radius. At the central region ($r/a < 0.2$) the trapped electron mode is quite large, yielding the depression of the electron temperature at $r/a < 0.2$ region in Figures 4.2 and 4.3. Here, large fluctuations of the electron thermal diffusivity of the trapped electron mode comes from the L_{n_i} term, where the L_{n_i} profile has a large fluctuation, as shown in Figures 4.1(c1) and (c2). At

the intermediate region ($0.2 < r/a < 0.8$) the ion temperature gradient mode becomes dominant, and ion thermal diffusivity is chosen to be two times of electron one for this mode, similar to the assumption in the Bohm-type model. The ion stored energies in the simulation results are, however, higher than those of experimental data in all cases. This could be accounted for by the contribution from the trapped electron mode in this intermediate region, because the contribution from the trapped electron mode is not small and the ion thermal diffusivity due to the trapped electron mode is equal to the electron one. At the outer region of the plasma column ($0.8 < r/a$) the resistive ballooning mode governs the electron/ion thermal diffusivity.

4.2.4 Simulation Results for H-mode Discharges

The understanding of plasma transport in tokamak plasmas is one of the most crucial issues for designing the future tokamak device such in the ITER machine. ITER physics R&D group has promoted comprehensive comparison between the experimental results from present machines and theoretical models with complicated transport simulation codes. For these purposes, radial profile data on plasma parameters such as density and temperatures have been gathered from many machines as ITER Database.

With our transport simulation code, we have carried out the comparison between experimental data installed in ITER Database and several theoretical models. Here we employ four models; i.e., the current diffusive ballooning mode model, the mixed shear model, the IFS/PPPL model and the multi-mode model. These models are applied for DIII-D and JET plasmas, where several discharges of L- and H-mode plasmas are included.

Current diffusive ballooning mode (CDBM) model

Simulation results are summarized in Figure 4.7, where the incremental stored energies defined by $W_{\text{inc}} = W - W_{\text{pedestal}}(r/a = 0.9)$ are compared between experimental data and simulation results, and the offset of the increment stored energy defined by $\Delta W_{e,i}/W_{e,i} = W_{\text{inc,sim}}/W_{\text{inc,exp}} - 1$ are plotted for various discharges in DIII-D and JET. Since almost all of the simulation results predict lower values than experimental data, the adjustment of the transport coefficients might be necessary for χ_e and χ_i . This adjustment factor is roughly estimated as follows. For precise analysis, we have to deal with electrons and ions, separately. However we consider the situation that the heating power due to equi-partition between electrons and ions is small in comparison with external heating power. In addi-

tion, provided that the heating terms are given and the convection term is neglected, the diffusion equation shows that $n\chi dT/dr = \int SdV_p = constant$. If the diffusion coefficient χ_{CDBM} is replaced with χ_{CDBM}/C_{CDBM} , the temperature might increase by a factor of $T^{5/2}$, because $\chi_{CDBM} \sim T^{3/2}$ and $\chi dT/dr \sim \chi_{CDBM}/C_{CDBM}T/L_T \sim T^{5/2}/C_{CDBM} = constant$. To check the validity of this recalibration factors, we have carried out transport simulation by changing the transport coefficient as $\chi_{sim} \implies \chi_{CDBM}/C_{CEBM}$. Figure 4.8 shows the stored energy as a function of a recalibration factor C_{CDBM} . When C_{CDBM} value is increased up to around $5 \sim 6$, the stored energy and the temperature profile agree with each other satisfactorily. In Table 4.4, the recalibration factors are listed for various modes and devices, respectively.

At first, let us see the difference between L- and H-mode plasmas. Systematically the simulation shows that in H-mode plasmas $\Delta W_{e,i}$ is lower than that obtained in L-mode for both DIII-D and JET cases. This indicates the improvement of the core transport coefficient in H-mode plasmas. By comparing the recalibration factors between L- and H-mode plasmas, we could find the improvement of the diffusion coefficient to be $1.8 \sim 2.1$ for electrons and $2.6 \sim 3.4$ for ions, where these improvement factors are yielded by the ratio between the recalibration factors of L- and H-modes, as $C_{CDBM,H}/C_{CDBM,L}$; e.g., $C_{CDBM,H} = 7.5$ and $C_{CDBM,L} = 3.5$ for electrons in DIII-D.

Systematic difference can be seen between DIII-D and JET plasmas. Since the recalibration factors in DIII-D are much larger than those in JET, the confinement performance in DIII-D might be superior to that in JET. The ratios of $C_{CDBM(DIII-D)}/C_{CDBM(JET)}$ are $1.8 \sim 2.2$ for electrons and $2.9 \sim 3.8$ for ions in L- and H-modes. This results imply that the hidden parameters exist which is not considered in the theory, for example, the effect of radial electric fields or non-local effects and so on.

Mixed shear(MS) model

JET group has proposed semi-empirical transport model based on the mixture of Bohm and GyroBohm diffusion models[4-19]. This model is based on Bohm-type model as shown in Section 4.2.2. In recent model, the shear is introduced into the Bohm-type diffusion coefficient by a form of $\chi_{e,i}^B = \chi_{e,i}^B(0) * f(s)$, where $f(s) = s^2/(1 + s^3)$ at $s > 0$. The recalibration factors are shown in Table 4.4, where the relation that $T^{5/2}/C_{MS} = const.$ is applied. We could say that the characteristics obtained in the mixed shear model seem to be very similar to those in CDBM model; i.e., the reduction of the transport coefficient should be introduced in H-mode plasmas in comparison with L-mode ones by a factor of ~ 1.5 for electrons and ~ 3.0 for ions, and the recalibration factor is different by a factor

of ~ 2.0 for electrons and ~ 4.0 for ions between DIII-D and JET.

Multi-mode model

An agreement between experimental data and simulation results are quite excellent for L- and H-modes in DIII-D plasmas; typically within $10 \sim 20\%$. In addition a slight improvement of the transport can be seen in H-mode plasmas, in comparison with L-mode ones. At the core confinement region the η_i -mode is dominant.

In case of CDBM model and Mixed Shear model, we found that the calibration of the transport coefficient is useful to predict the experimental data. On the other hands, in case of IFS/PPPL model without no shear flow, we can not find the same tendency as CDBM model and Mixed Shear model.

4.2.5 Dimensionally Similar Simulation

The dependence of the thermal diffusivity on the normalized gyro-radius $\rho^*(= \rho_s/a)$ has been investigated on various tokamak devices with dimensionally similar discharges, where other non-dimensional parameters such as beta value and normalized collisionality are controlled to be fixed between dimensionally similar discharges. Many transport models have been proposed theoretically and/or empirically, and some of them could reproduce experimental data with a good accuracy. However, these transport models should be tested for the dimensionally similar discharges, because we would like to know whether the transport model proposed would be reasonable and reliable on the extrapolation to large tokamak devices such as ITER or not.

In the previous section, we have compared simulation results with experimental data from the viewpoint of their electron and ion temperatures themselves. Here, we discuss the simulation results how to scale the plasma temperatures as a function of the normalized gyro-radius ρ^* . We carry out transport simulations for two sets of dimensionally similar discharges, and compare the scaling of the temperatures as a function of the normalized gyro-radius. Here, we call this transport simulation as dimensionally similar simulation. We should pay attention to other non-dimensional parameters in this dimensionally similar simulation, because the plasma temperatures calculated in the transport simulation might be, in general, different from the experimental data.

In comparison of simulation results with the normalized gyro-radius scaling, we introduce the function $G(r)$ defined by

$$\chi_{\text{scl}} = \chi_{\text{B}} (\rho^*)^\alpha F(\beta, \nu^*, q, \dots) , \quad (4.25)$$

$$G_{\text{scl}}(r) = \frac{\chi_{\text{scl}}^{\text{Bt1}}/\chi_{\text{scl}}^{\text{Bt2}}}{\chi_{\text{model}}^{\text{Bt1}}/\chi_{\text{model}}^{\text{Bt2}}} \quad (\text{scl} = \text{B, WGB, GB}) . \quad (4.26)$$

where χ_{model} is the thermal diffusivity employed in the transport simulation, given in equations in Section 4.2.2, and scl means the Bohm(denoted by B, and $\alpha = 0.0$), Weak-Gyro-Bohm(denoted by WGB, and $\alpha = 0.5$) and Gyro-Bohm(denoted by GB, and $\alpha = 1.0$) scalings, respectively. Two different toroidal magnetic field strengths employed in dimensionally similar discharges are denoted with *Bt1* and *Bt2*.

First of all, let us discuss the validity of dimensionally similar simulation, using the Bohm diffusion case for #21795 and #21810 discharges, where the thermal diffusivity is assumed to be $\chi_{\text{model}} = \chi_{\text{Bohm}} = T_e/eB_T$ and the convection term in equations (4.3) and (4.4) defined by $(3/2)T\Gamma$ is neglected. In Figure 4.9(a), the simulation results for two different toroidal field strengths are compared, and as expected, the function $G(r)$ defined by equation (4.39) is uniquely unity in all minor radius for the Bohm scaling case($\alpha = 0.0$).

Next we have carried out transport simulation with the Bohm type model given by eq. (4.8), neglecting the convection term. Even though the Bohm-type model is employed, the transport characteristics becomes slightly different from the Bohm scaling, and the Weak-Gyro-Bohm feature appears, as shown in Figure 4.9(b1). The diffusion coefficient in this model is Bohm type, but has additional factor given by q^2/L_T^* , which is introduced to explain the global confinement characteristics ($\tau_E \sim I_p P^{-1/2}$). The deviation of the simulation results from the Bohm scaling, as shown in Figure 4.9(b1), can be accounted for by this factor.

Figure 4.9(b2) shows the differences of the safety factor q , the temperature scale length L_t^* and q^2/L_t^* value between two discharges. We can see that the disagreement of these non-dimensional parameters give rise to a deviation from the Bohm-type characteristics to the Weak-Gyro-Bohm one. If additional control technique for the profiles of the plasma current and the heat deposition can be applicable, we could fix these non-dimensional parameters as well as β and ν^* values, and carry out dimensionally similar experiments more strictly.

Finally we have considered the convection term in the simulation. As shown in Figure 4.9(c), the convection effect might recover the Bohm characteristics slightly. When we compare two simulation results and discuss on the ρ^* -scaling, we have to pay attention to other non-dimensional parameters such as beta value and normalized collisionality. In experiments these parameters are in agreement within $\pm 10\%$ difference, while the agreements of these parameters evaluated with simulation results are within $\pm 15\%$ difference.

From these considerations we could conclude that the simulations carried out for two discharges could be called as the dimensionally similar simulation, and comparison with dimensionally similar experiments might be valid and fruitful.

In comparison with experimental analysis, where the effective thermal diffusivity including the convection term is evaluated experimentally, we employ the effective thermal diffusivity defined by

$$\chi_{\text{eff},j} = \frac{\int_0^r (S_j) dV}{r \langle |\nabla r|^2 \rangle n_j \frac{\partial T_j}{\partial r}} \quad (j = e, i) , \quad (4.27)$$

where in the numerator the convection term is not discriminated. We compare simulation results with the ρ^* -scaling, introducing the function $H(r)$

$$H_{\text{scl}}(r) = \frac{\chi_{\text{scl}}^{\text{Bt1}} / \chi_{\text{scl}}^{\text{Bt2}}}{\chi_{\text{eff}}^{\text{Bt1}} / \chi_{\text{eff}}^{\text{Bt2}}} \quad (\text{scl} = \text{B, WGB, GB}) . \quad (4.28)$$

With different transport models, the dimensionally similar simulation has been carried out for two cases ($q_{\text{eff}} = 4.5$ and 6.0 series), and results are summarized in Figures 4.10 - 4.13, in comparison with experimental data. Before discussing simulation results, let us briefly summarize the experimental results. Experimental data shows the Weak-Gyro-Bohm characteristics for electrons, and lies between the Weak-Gyro-Bohm and the Bohm scalings for ions, as referred in Figs. 4.10(d)- 4.13(d).

Firstly, let us see the results of the Bohm-type model. For electrons, the simulation results are between the Weak-Gyro-Bohm and the Bohm scalings, this tendency is consistent with experimental characteristics. Ions also behaves the similar scaling with that for electrons. Compared with experimental data, simulation results might present a strong tendency of the Weak-Gyro-Bohm characteristics.

Let us turn to the CDBM model. As expected from the CDBM model, the simulation results show clearly the Gyro-Bohm characteristics for electrons and ions in the $q_{\text{eff}} = 4.5$ case. The CDBM model given by equation (4.10) is simply reduced as follows;

$$\begin{aligned} \chi &= \chi_{\text{B}} \rho^* F(q, L_t^*, s, \alpha, \kappa) \\ &\sim \chi_{\text{B}} \rho^* q^2 F(s, \alpha, \kappa) / (L_t^*)^{3/2} \end{aligned} \quad (4.29)$$

and is expected to behave a Gyro-Bohm characteristics. In addition, the dependences on the safety factor and the temperature scale length are almost the same with those of the Bohm-type model given by equation (4.8). However, the transport simulation results show the small deviation from the Gyro-Bohm characteristics, as shown in Figure 4.10(b). In Figure 4.14, the ratio of non-dimensional parameters, $q^2 / (L_t^*)^{3/2}$ and $F(s, \alpha, \kappa)$ between

shot No.21795 and 21810 are plotted, and the deviation of the value $F(q, L_t^*, s, \alpha, \kappa)$ is found to be small between two discharges. Consequently, we can observe the Gyro-Bohm characteristics which is inherent characteristics of CDBM model. While, in the $q_{\text{eff}} = 6$ case, the simulation results are deviating from the Gyro-Bohm scaling remarkably. In Figure 4.15(a) and (b), the beta values and the normalized collisionalities are depicted for $q_{\text{eff}} = 4.5$ and 6.0 cases. The agreements of these non-dimensional parameters are quite excellent in the $q_{\text{eff}} = 4.5$ case, while the difference of about 40 % can be seen on the beta values all over the region of the plasma column and the normalized collisionality deviate with each other at the outer region of the plasma column in the $q_{\text{eff}} = 6$ case. These disagreements of other non-dimensional parameters might account for the large deviation of the simulation results from the Gyro-Bohm scaling in Figure 4.12(b) and 4.13(b). Nevertheless, we could say that the CDBM model which theoretically predicts the Gyro-Bohm characteristics seems to be inapplicable for JT-60U L-mode plasmas.

Finally, we examine the Multi-Mode model. Although the simulation results especially for electrons show large fluctuations originated from the ion density gradient appeared in the thermal diffusivity of the trapped electron mode, the Gyro-Bohm characteristics can be seen in the simulation results for electrons and ions at the central region of the plasma columns. This characteristics might be consistent with theoretical prediction based on the multi-mode model, but is different from experimental results. Here we should remark that the ρ^* -scaling characteristics changes from the Gyro-Bohm scaling to the Bohm scaling as the minor radius increases. This might suggest that the proper combination of the ion temperature gradient mode and the resistive ballooning mode is applicable for JT-60U L-mode plasmas at the outer region of the plasma column.

4.2.6 Conclusion

Dimensionally similar discharges in JT-60U L-mode plasmas have presented the confinement characteristics between the Bohm and Gyro-Bohm scaling, which is denoted as the Weak-Gyro-Bohm scaling. To study this confinement characteristics of the ρ^* scaling experiments, transport simulations have been carried out with three different transport models; the Bohm-type, the Current-Diffusive-Ballooning-Mode and the Multi-Mode models.

For all models the electron stored energy is in agreement with experimental data within 15 % or less difference, and the standard deviation of the electron temperature profiles between experimental data and simulation results is at most 20~ 30 % difference.

Depending on the multiplication factor of the ion thermal diffusivity to the electron one, the simulation results for the ion temperature yield a large difference from the experimental data. In the Bohm model with $\chi_i = 2\chi_e$ the simulation results predict a lower ion temperature than the experimental data, while in the CDBM model with $\chi_i = \chi_e$ the ion temperature is quite higher in the simulation results. In the Multi-Mode model the ion temperature in the simulation results is higher, as well. This might be accounted for, when the multiplication factor is taken into account; i.e., the multiplication factor is two for the ITG mode and one for the TE and RB modes.

It might be difficult to discuss the validity of transport model by comparing the absolute values of the plasma temperatures between experimental data and simulation results, because the discrepancy of the plasma parameters sometimes caused by the numerical coefficient of the thermal diffusivity. To study physical characteristics of the transport model, comparison between two simulation results for dimensionally similar discharges is quite meaningful. Here we have examined simulation results from the viewpoint of the ρ^* scaling, and compared the ρ^* features observed in experiments. In the Bohm-type model it is found that the simulation results behave the Weak-Gyro-Bohm characteristics for electrons and ions, even though the Bohm-type thermal diffusivity is incorporated. This can be accounted for, by the factor q^2/L_T^* in the diffusion coefficient. In the CDBM model, the simulation results clearly show the Gyro-Bohm characteristics in the $q_{\text{eff}} = 4.5$ case. Unfortunately we could not see this feature in the $q_{\text{eff}} = 6.0$, because other non-dimensional parameters such as beta and normalized collisionality are different between two simulation results. In the Multi-Mode model, Gyro-Bohm characteristics has been yielded in the simulation results. From these considerations we could conclude that the Bohm-type model which has been empirically developed in JET L-mode plasmas might be applicable for JT-60U L-mode plasmas, as well, from the viewpoints not only of the absolute value of plasma temperatures but also of ρ^* scaling.

Table 4.2: Coefficient of the Multi Mode model.

	χ_e	χ_i
Trapped electron mode	$F_e^{\text{TE}} = 0.2$	$F_i^{\text{TE}} = 0.2$
η_i mode	$F_e^{\text{ITG}} = 3.0$	$F_i^{\text{ITG}} = 6.0$
Resistive ballooning mode	$F_{e1}^{\text{RB}} = 3.0$	
	$F_{e2}^{\text{RB}} = 4.0$	$F_i^{\text{RB}} = 4.0$

Table 4.3: Plasma parameters of JT-60U discharges.

Shot number	21795	21810	21796	21811
q_{eff}	4.5	4.5	6.0	6.0
$B_t(\text{T})$	2.4	4.0	2.4	4.0
$I_p(\text{MA})$	1.35	2.25	1.00	1.65
$\bar{n}_e(10^{19}\text{m}^{-3})$	1.3	2.5	0.94	1.9
Z_{eff}	2.5	2.5	2.5	2.3
$P_{\text{NBI}}^e(\text{MW})$	1.5	2.9	1.2	2.3
$P_{\text{NBI}}^i(\text{MW})$	2.0	4.8	1.5	3.9
$P_{\text{OH}}(\text{MW})$	0.5	1.0	0.3	0.5
$W_e(\text{MJ})$	0.37	0.91	0.24	0.67
$W_i^{\text{th}}(\text{MJ})$	0.30	0.78	0.15	0.50
$W_f(\text{MJ})$	0.41	0.56	0.44	0.66

Table 4.4: Recalibration factors in the transport coefficient defined as $\chi_{\text{sim}} \Leftarrow \chi_{\text{CDBM/MS}}/C_{\text{CDBM/MS}}$, introduced in CDBM and Mixed Shear models. The values in bracket denote the ratio of the recalibration factor between L- and H-mode plasmas.

		DIII-D					JET				
CDBM	Electron	3.51	—	(2.13)	→	7.46	1.97	—	(1.75)	→	3.44
	Ion	2.65	—	(2.59)	→	6.85	0.69	—	(3.43)	→	2.37
MS	Electron	2.95	—	(1.66)	→	4.90	1.53	—	(1.41)	→	2.16
	Ion	3.56	—	(3.26)	→	11.6	0.91	—	(2.84)	→	2.58

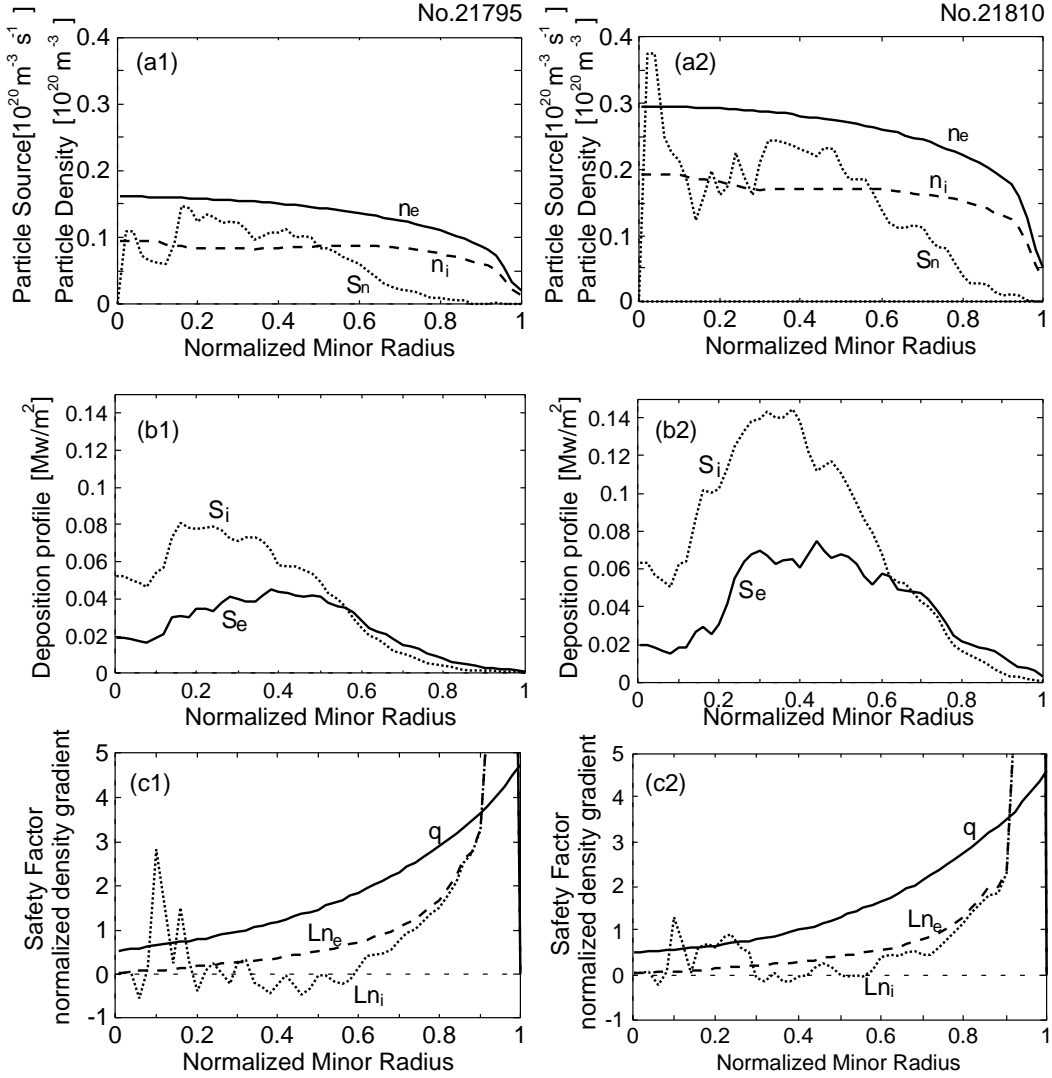


Figure 4.1: (a1), (a2) Density and particle source profile of Shot No.21795 and 21810. solid line : electron density, broken line : ion density, dotted line : particle source profile, Ion density is estimated from Z_{eff} and fast ion density. (b1), (b2) NBI heating power of Shot No.21795 and 21810, solid line : for electrons (S_e), broken line : for ions (S_i). (c1), (c2) Safety factor and normalized density gradient profile of Shot No. 21795 and 21810, solid line : safety factor, broken line : normalized electron density gradient, dotted line : normalized ion density gradient profile.

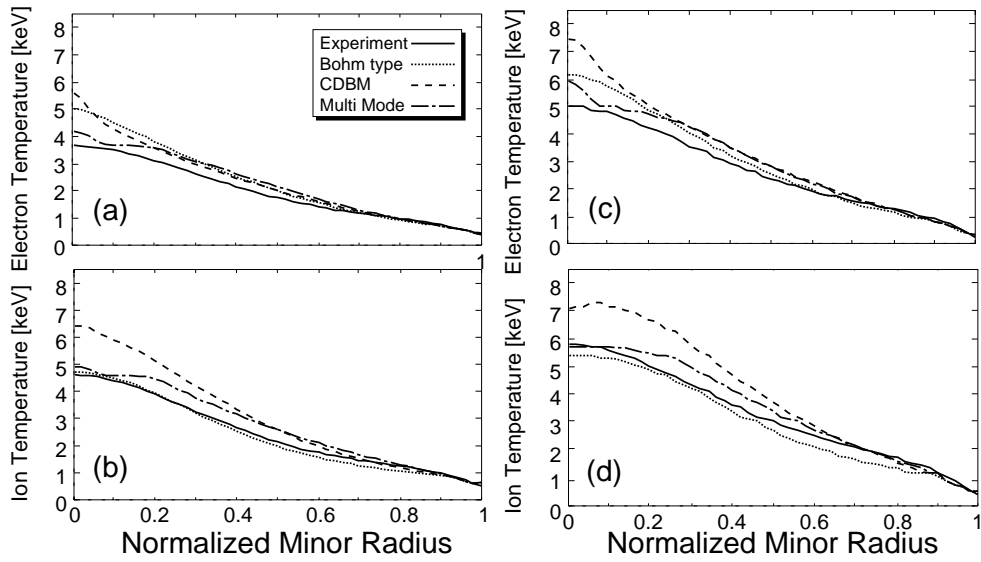


Figure 4.2: Electron and ion temperature profile on the group 1: (a) the electron temperature profile of #21795. (b) the ion temperature profile of #21795. (c) the electron temperature profile of #21810. (d) the ion temperature profile of #21810.

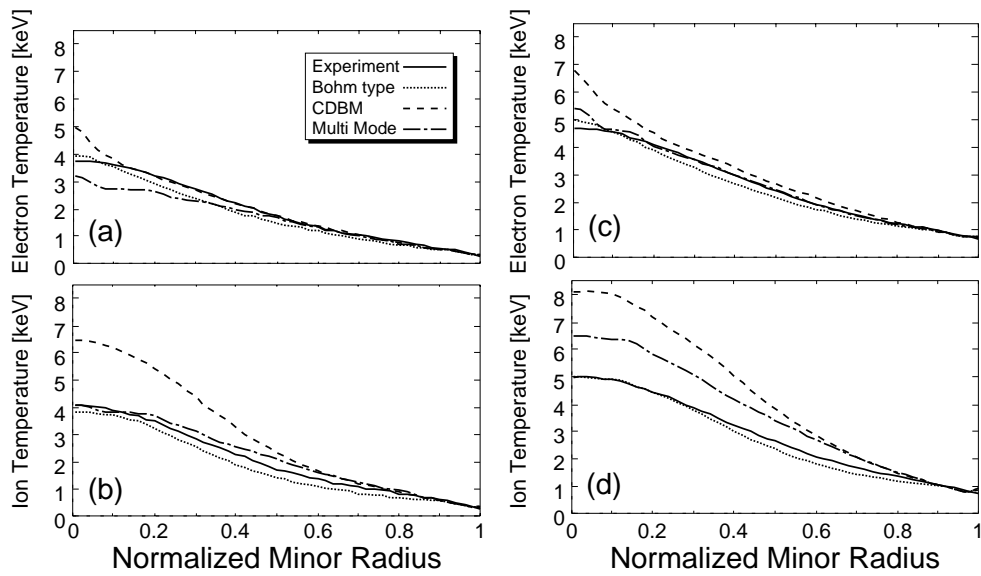


Figure 4.3: Electron and ion temperature profile on the group 2: (a) the electron temperature profile of #21796. (b) the ion temperature profile of #21796. (c) the electron temperature profile of #21811. (d) the ion temperature profile of #21811.

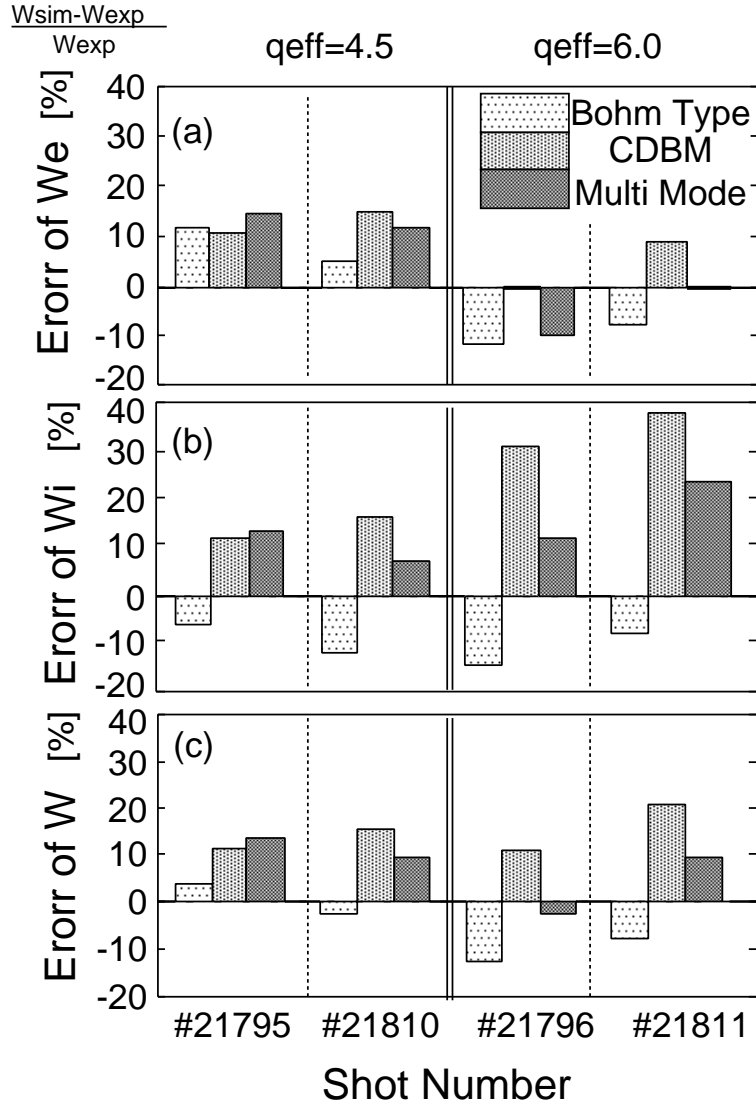


Figure 4.4: Error in the stored energy : (a) the electron stored energy W_e . (b) the ion stored energy W_i . (c) the total stored energy W_{total} .

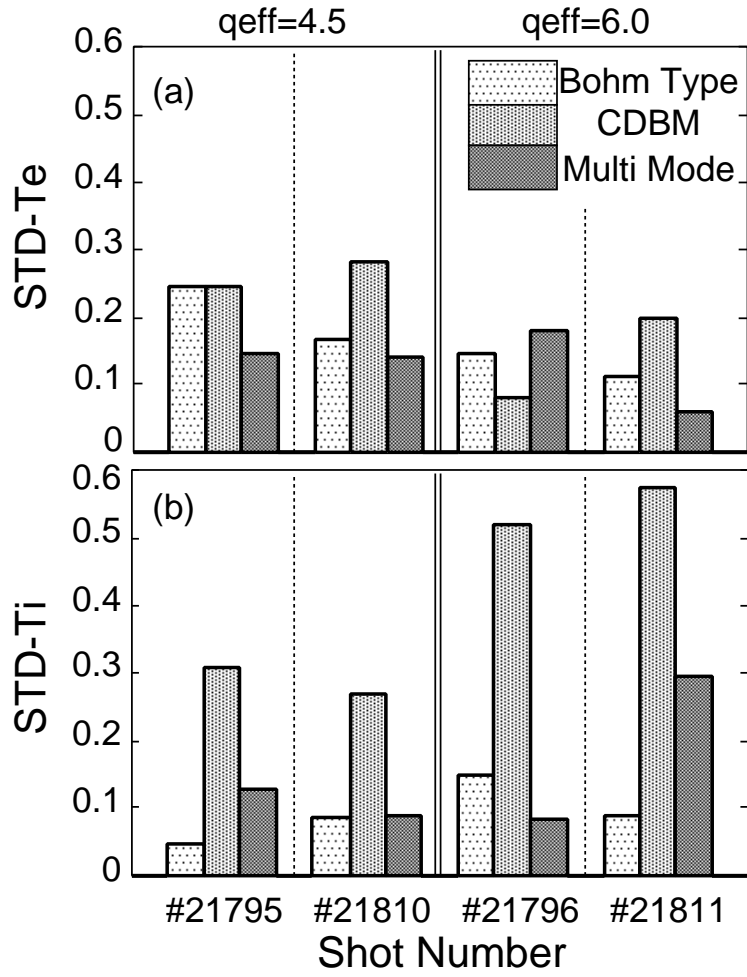


Figure 4.5: STD for each model: (a) STD-Te of each model. (b) STD-Ti of each model.

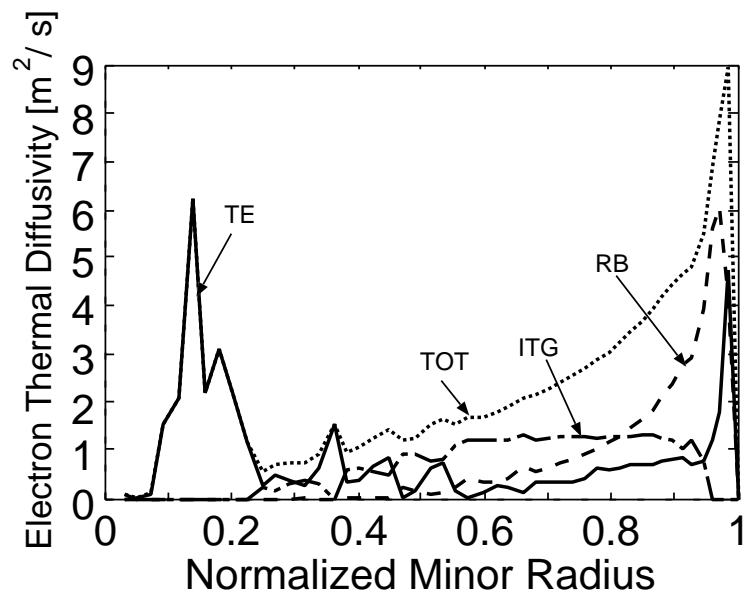


Figure 4.6: Electron thermal diffusivity of Multi Mode model of #21795

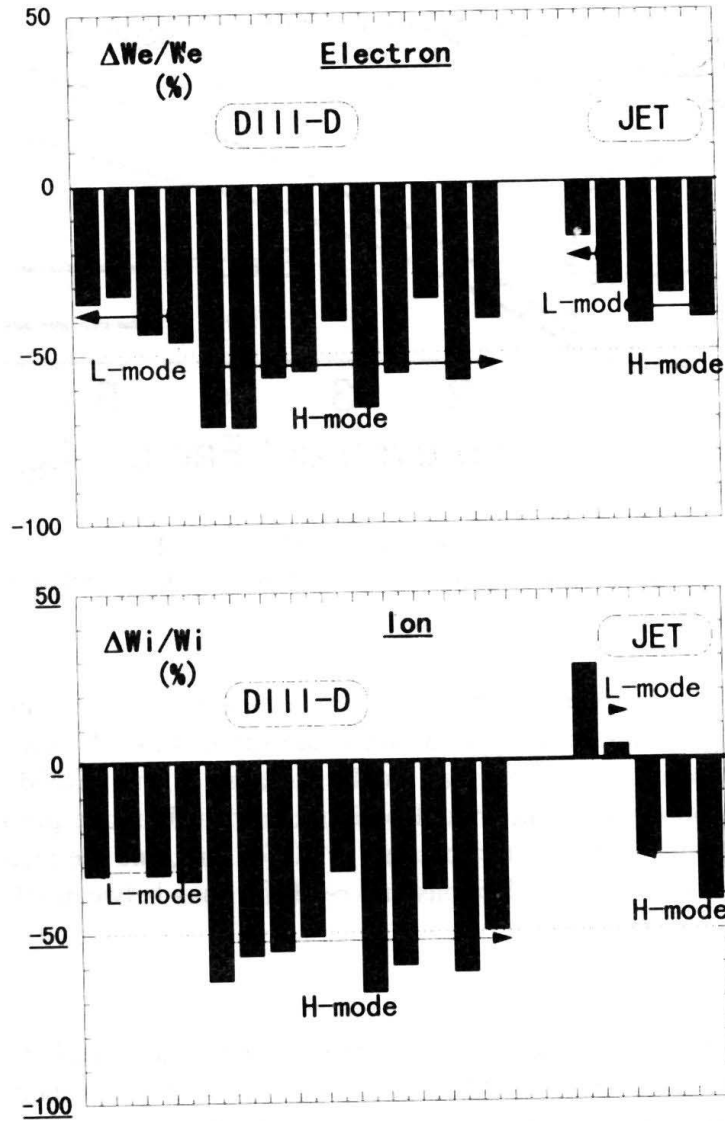


Figure 4.7: Simulation results with the CDBM model for L- and H-mode plasmas in DIII-D and JET. The offsets of the increment stored energy are plotted, where $\Delta W_{e,i}/W_{e,i}(\%) = W_{inc,sim}/W_{inc,exp} - 1$ and $W_{inc} = W - W_{pedestal}(r/a = 0.9)$.

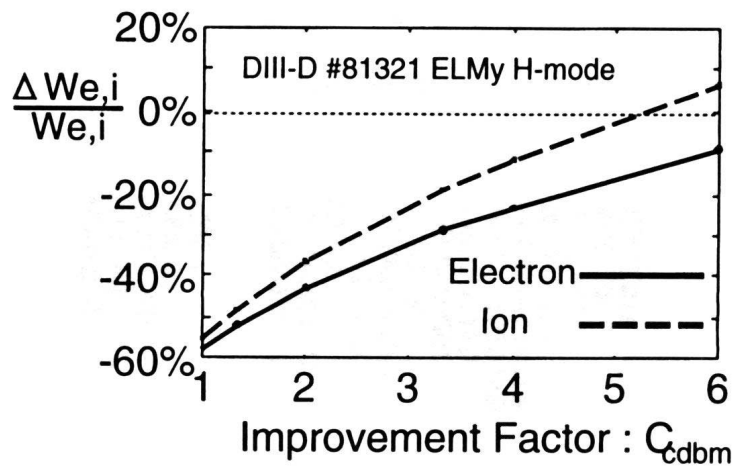


Figure 4.8: Transport coefficient is changed with a recalibration factor C_{CDBM} ($\chi_{\text{sim}} \leftarrow \chi_{\text{CDBM}}/C_{\text{CDBM}}$), and the offset of the increment stored energy is plotted as a function of a recalibration factor C_{CDBM} .

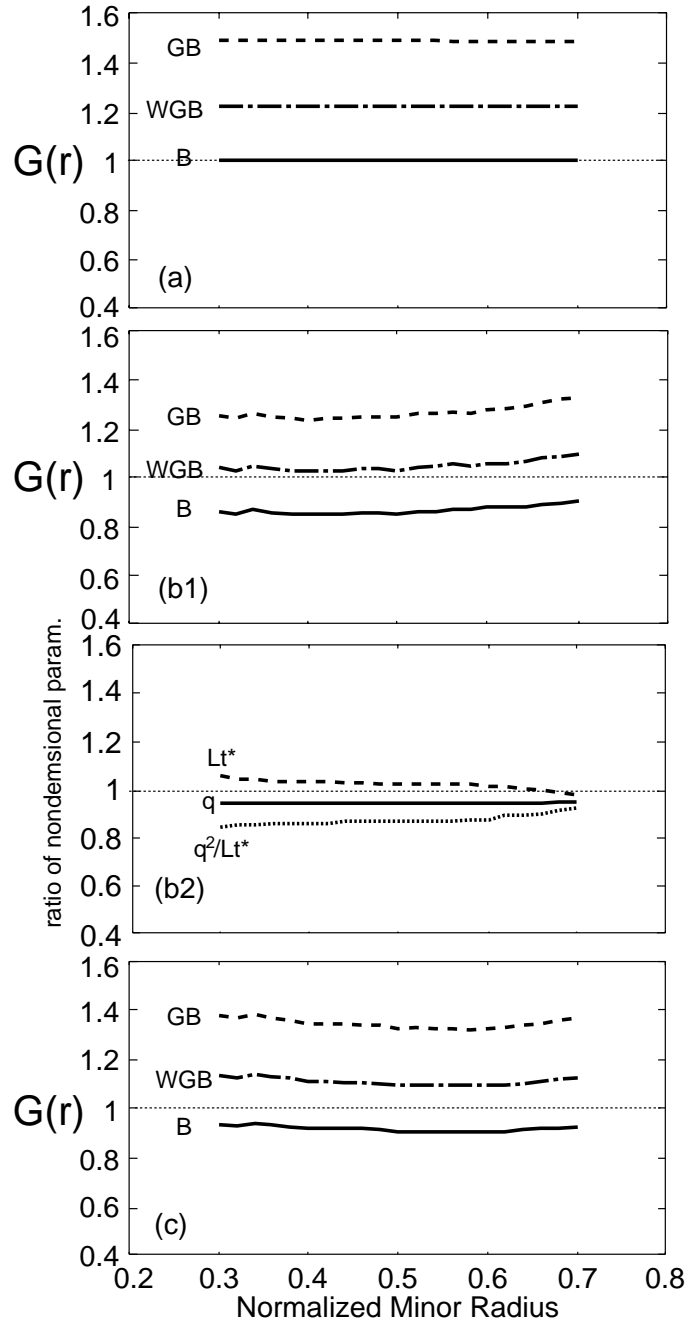


Figure 4.9: Dependence of ρ^* : (a) the feature of Bohm diffusivity with no convection term. (b1) the feature of Bohm Type model with no convection term. (b2) Ratio of non-dimensional parameters, q (solid line), L_T^* (broken line) and q^2/L_t^* (dotted line) between shot No.21795 and 21810. (c) the feature of Bohm Type model with convection term

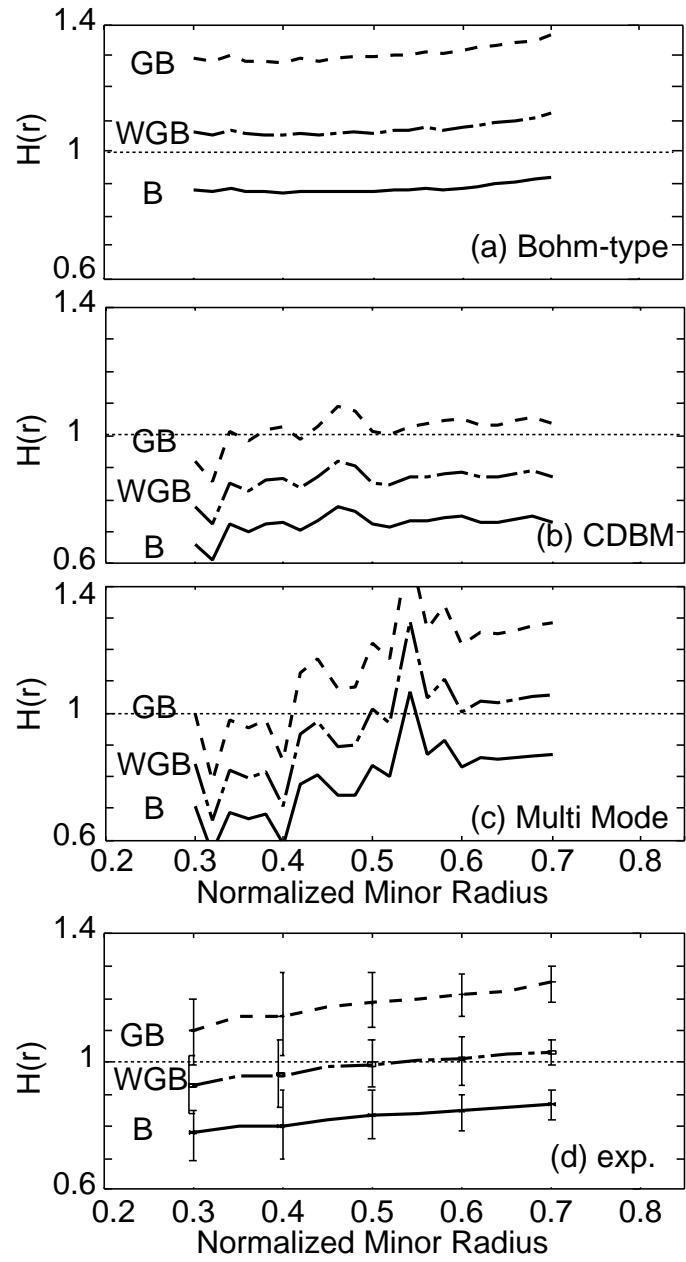


Figure 4.10: ρ^* dependence of the electron thermal diffusivity of #21795 and #21810: (a) Bohm-type model. (b) CDBM model. (c) Multi-Mode model. (d) the experimental results.

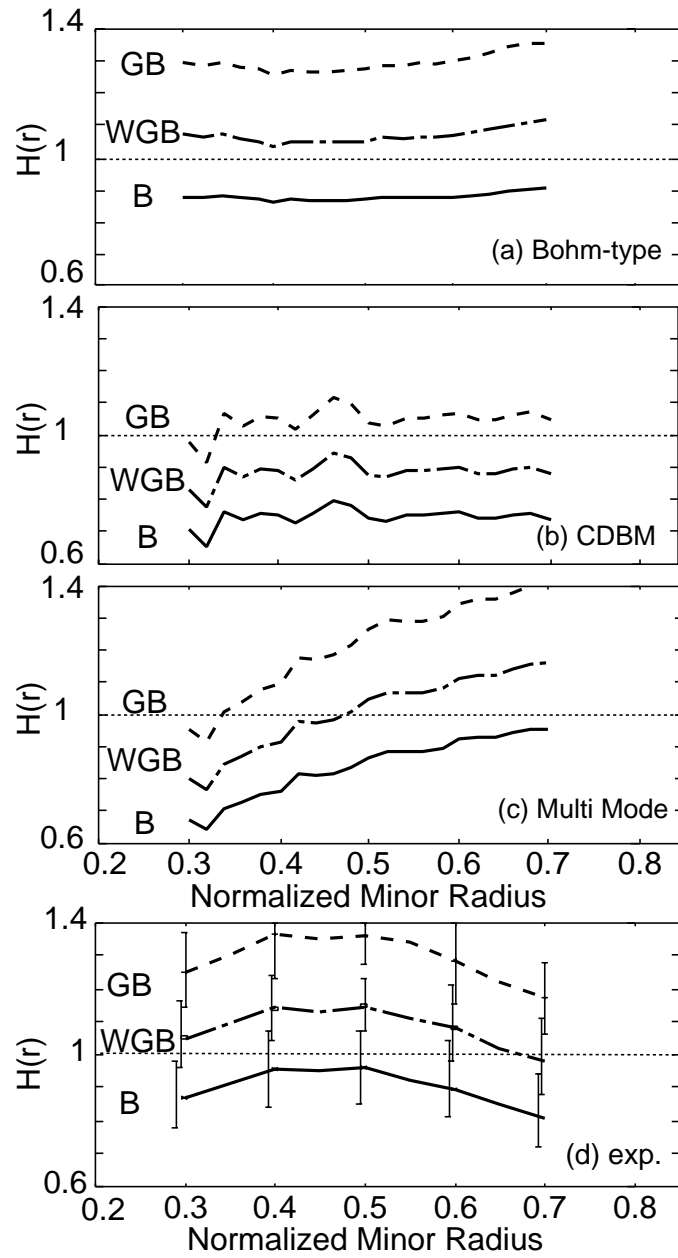


Figure 4.11: ρ^* dependence of the ion thermal diffusivity of #21795 and #21810: (a) Bohm-type model. (b) CDBM model. (c) Multi-Mode model. (d) the experimental results.

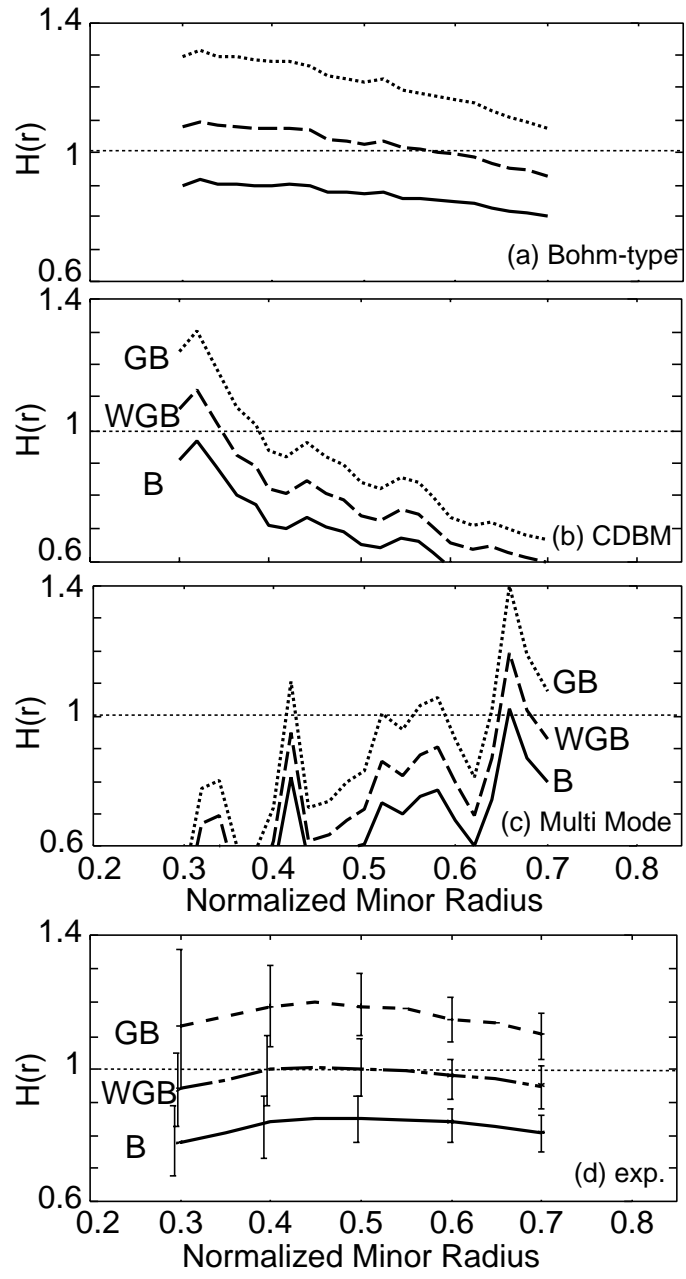


Figure 4.12: ρ^* dependence of the electron thermal diffusivity of #21796 and #21811: (a) Bohm-type model. (b) CDBM model. (c) Multi-Mode model. (d) the experimental results.

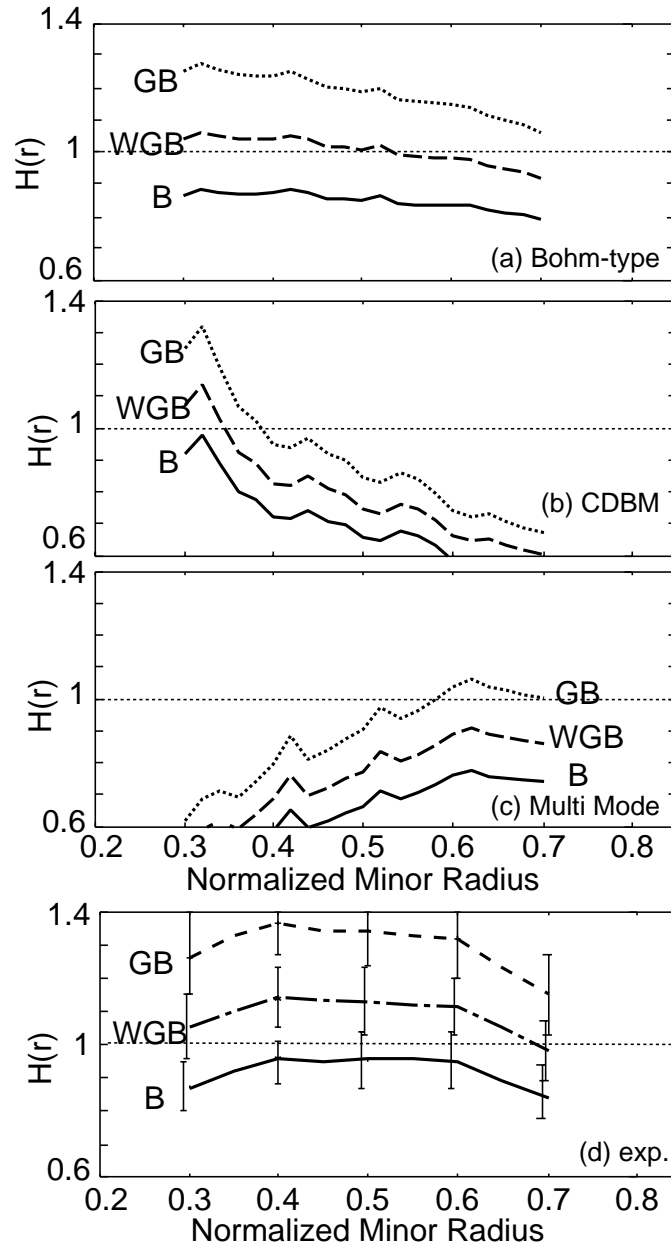


Figure 4.13: ρ^* dependence of the ion thermal diffusivity of #21796 and #21811: (a) Bohm-type model. (b) CDBM model. (c) Multi-Mode model. (d) the experimental results.

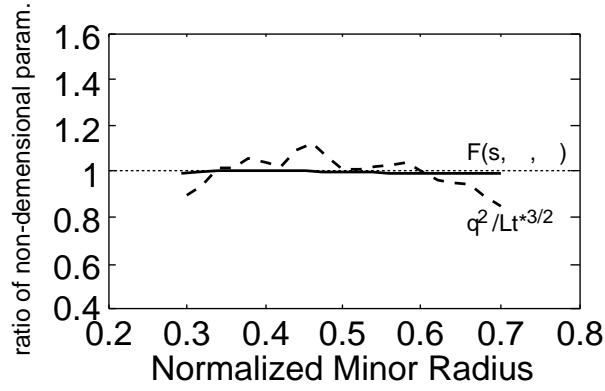


Figure 4.14: Ratio of non-dimensional parameters, $F(s, \alpha, \kappa)$ (solid line) and $q^2 / (L_t^*)^{3/2}$ (broken line) between shot No. 21795 and 21810

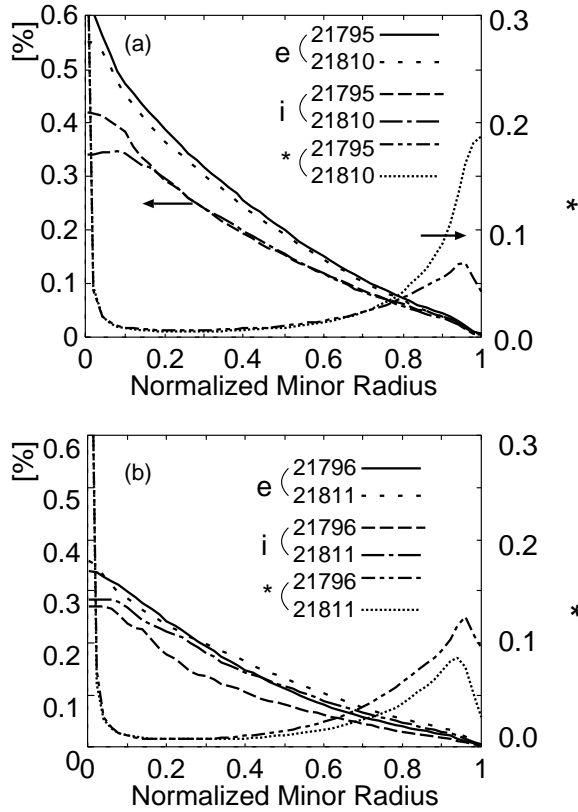


Figure 4.15: Comparison of nondimensional parameters, β_e , β_i and ν^* of simulation results with CDBM model for (a) : $q_{\text{eff}} = 4.5$ and (b) : $q_{\text{eff}} = 6.0$

4.3 L-H Transition Modeling

4.3.1 High Confinement Mode (H-mode)

At present, the High Confinement Mode (H-mode) is thought to be an attractive candidate for plasma operation of next generation experimental reactors and future fusion power plants. For about the past twenty years, much effort has been made to resolve the physics of the H-mode through both experimental and theoretical studies. In the H-mode phase, the radial electric field, which is related to the plasma flow within a flux surface through the radial force balance, is found to increase in the plasma edge region where a transport barrier is formed [4-21, 4-22]. According to experimental and theoretical understanding, the flow shear is considered to be important in reducing the turbulence, which results in a transport barrier in the plasma edge region [4-23, 4-24]. There are several theoretical models for the H-mode, but the time and spatial resolution of diagnostics have not been precise enough to determine the physical basis for generating the flow shear [4-25]. A reliable first principle way has not yet been obtained for predicting the L-H transition threshold power over a wide range of operating conditions and plasma configurations.

Comparisons between physical models using local plasma parameters in the edge region have been carried out recently [4-26, 4-27]. These studies found that local plasma parameters in the edge region are broadly consistent with several models of the L-H transition, but these models do not clearly specify the L-H transition conditions. Physical models should also be compared with L-H transition threshold power scaling laws defined in terms of global plasma parameters in order to understand the implications of the L-H transition threshold power scaling for power requirements in future fusion experiments. The relationship between physical models and L-H threshold power is roughly examined as in ref. [4-3]. Although P_{th} of Shaing model is not considered in ref. [4-25], in case of $P_{th} \propto B_t^{\alpha_B} n_e^{\alpha_{n_e}} I_p^{\alpha_{I_p}}$, the B_t , n_e and I_p dependences of P_{th} (α_B , α_{n_e} and α_{I_p}) are supposed $\alpha_{B_t} > 0$, $\alpha_{n_e} > 0$ and $\alpha_{I_p} < 0$ because the transition condition of Shaing model is originally $\nu_{*i} < \nu_c$ (or $n_e R q / \epsilon^{3/2} T_i^2 < c$) where ν_{*i} , ν_c and c are normalized collisionality, critical ion collisionality and a constant, respectively [4-24, 4-28]. This assumption is the same tendency with $P_{th} \propto B_t^{1.4} n_e^{0.5} I_p^{-0.7}$ proposed by Itoh [4-25, 4-29].

In this study, the radial effect of orbit loss is taken into Shaing model and the comparison with P_{th} scaling as for global parameter dependence are carried out by 1.5-D transport code. We investigate not only the validity of the transition model under typical plasma conditions, but also the sensitivity to boundary conditions and anomalous

diffusivities.

4.3.2 Shaing L-H Transition Model

The basic concept of this model is the determination of poloidal flow from a balance of the torque caused by ion orbit loss against the neoclassical viscous force, which is extended to the conditions $V_p B / v_t B_p \sim 1$, where V_p, B, B_p and v_t are the poloidal flow velocity, toroidal and poloidal magnetic fields, and the ion thermal velocity, respectively [4-24, 4-28]. The momentum balance equation for ions is expressed as $\langle \mathbf{B} \cdot \nabla \cdot \mathbf{\Pi}_i \rangle = \langle \mathbf{B} \cdot \mathbf{S}_{orb}^i \rangle$, where the left hand side is the extended viscous force parallel to \mathbf{B} and the right hand side is the torque generated by ion orbit loss. The viscous force normally has contributions from both passing particles and trapped (banana) particles in standard neoclassical theory, but at the edge where the L-H transition occurs we have to consider modifications to the viscosity under the conditions of ion orbit loss. The viscous force is defined as $\langle \mathbf{B} \cdot \nabla \cdot \mathbf{\Pi}_i \rangle = n_i m_i B^2 \mu_i U_{\theta i}$, where n_i, m_i, B are ion density, ion mass and magnetic field, and $U_{\theta i} = (v_i / B) [V_{\parallel} / v_i - c E_r / (B_p v_i) + c p'_i / (n_i v_i B_p)]$. V_{\parallel}, v_i, E_r and p'_i are the parallel flow, ion velocity, radial electrical field and gradient of the ion pressure profile. The viscosity coefficient, μ_i , including ion orbit loss effects is expressed as:

$$\mu_i = \frac{\kappa_b^i \kappa_{ps}^i}{(\kappa_b^i + \kappa_{ps}^i)} [1 - \exp(-C)] + \kappa_{ps}^i \exp(-C) \quad (4.30)$$

$$C = \left[C_1 \nu_*^{0.25} + C_2 \frac{a - r}{\Delta \rho_{orb}} \right]^2 \quad (4.31)$$

where $\kappa_b^i, \kappa_{ps}^i$ express the contributions to the viscosity by banana and passing particles, respectively, ν_* is the normalized collisionality, $\Delta \rho_{orb}$ is the ion poloidal Larmor radius, r is the local minor radius, a is the minor radius of the plasma boundary, and C_1 and C_2 are numerical constants ($C_1 = 0.56$ and $C_2 = 0.11$ are applied in this study). In this model we have converted the original lumped parameter model to a local model by having only the plateau-Pfirsch-Schluter contribution at the plasma edge ($r = a$) where $C = 0$, and matching the standard neoclassical viscosity coefficient [4-30] deeper in the plasma where C is large.

The orbit loss term is expressed as

$$\langle \mathbf{B} \cdot \mathbf{S}_{orb}^i \rangle = -\frac{\langle B^2 \rangle}{B_{t0}} m_i v_{ti} \sqrt{\frac{2\epsilon}{|S_i|}} \left. \frac{dn_i}{dt} \right|_{orb} \exp(-C), \quad (4.32)$$

where $\left. \frac{dn_i}{dt} \right|_{orb}$ is the ion orbit loss rate and its definition is in ref [4-28]. This definition is based on the particle loss rate in the presence of a velocity-space loss cone.

4.3.3 Simulation Results

The improved confinement in the H-mode phase is incorporated in the thermal diffusivities induced by plasma fluctuations as follows,

$$\chi_{e,i} = \chi_{e,i}^{\text{neo}} + \chi_{e,i}^{\text{ano}}/F_{\text{H}} \quad (4.33)$$

where $\chi_{e,i}$ is the total thermal diffusivity and $\chi_{e,i}^{\text{neo}}, \chi_{e,i}^{\text{ano}}$ are neoclassical and anomalous diffusivities, respectively. Subscripts e, i indicate the species, electron and ion, respectively. The parameter F_{H} is the improvement factor for H-mode. Although F_{H} should be dependent on the flow shear parameter, we apply a constant value, $F_{\text{H}} = 10.0$, for simplicity once the L-H transition condition is satisfied at each mesh point.

We emphasize that our focus in this study is on the qualitative agreement of the physical mechanism for the L-H transition and not on the quantitative agreement between experimental data and calculated results. In order to avoid ambiguity in the effects on particle diffusivity, particle profiles are specified, which is consistent with the way transport model testing has been done for the ITER Physics R&D expert group [4-31]. The anomalous thermal diffusivity coefficient is assumed to be given by $\chi_{e,i}^{\text{ano}} = C_{e,i}(1.0 + r^2/a^2)/\tau_E^{\text{ITER89P}}$.

It is possible that boundary conditions at the separatrix can have a strong impact on the L-H transition condition because the H-mode transport barrier is formed in the plasma edge region. In this study the boundary condition for density is

$$n_e^{\text{edge}} = n_i^{\text{edge}} = 0.00236n_e^{1.08}\kappa^{1.11}B_T^{0.78}, \quad (4.34)$$

which is proposed by the ITER Physics R&D Divertor group [4-32]. The boundary conditions for temperature are $T_e^{\text{edge}} = 50$ [eV] and $T_i^{\text{edge}} = 100$ [eV] as observed in DIII-D [4-33], but these conditions may not be consistent with all experimental results, such as ASDEX-U experimental results[4-34]. The sensitivity of edge temperature value is also examined in the following section.

Figures 4.16 show typical calculated results for the L-H transition. Figure 4.16 (a) is the time evolution of the NBI heating power, volume averaged electron temperature and poloidal Mach number at $r/a = 0.99$, and Figure 4.16 (b) is the time evolution of the electron temperature profile. NBI heating power increases at $t = 527$ [msec] and the L-H transition occurs at $t = 570$ [msec]. The time scale for the L-H transition is of the order of μsec , which is as same as a collision time and corresponds to the characteristic time step in the calculations. The averaged electron temperature increases on the confinement time scale, which is on the order of msec.

4.3.4 Comparison with L-H transition threshold power scaling law

At present, L-H transition threshold power scaling laws are often applied to the design of next generation experimental devices and future power plants. This semi-empirical approach is based on a multi-machine ITER threshold database [4-31]. One of the expressions, supported by dimensional constraints, is given by

$$P_{th}^{LH} = 2.76M^{-1}B_t^{0.96}n_{20}^{0.77}R^{1.23}a^{0.76}, \quad (4.35)$$

where the units of P_{LH}^{th} , M , B_t , n_{20} , R , and a are MW, AMU, T, 10^{20} m^{-3} , m and m, respectively.

Even though this scaling law is supported by dimensional considerations, the physical basis for the scaling is not known. To improve the accuracy of prediction over that of such scaling laws, we need to resolve their physical uncertainty, for example, reasons for the dependence on B_t and n_{20} or for the independence of I_p .

As a first step toward developing a physical meaning, the L-H transition threshold power estimated by physical models should be compared with scaling laws. In this study, we examine Shaing L-H transition model near the plasma edge over the range of $1.5 < B_t < 2.75$ [T], $1.2 < I_p < 2.2$ [MA], $1.5 \times 10^{19} < \langle n_e \rangle < 3.0 \times 10^{19} \text{ [m}^{-3}]$ and plasma surface safety factor $3.0 < q_a$.

Figure 4.17 (a) shows the B_t dependence of the calculated L-H transition power normalized by B_t . This result is for $I_p = 1.4$ [MA], $\langle n_e \rangle = 3.0 \times 10^{19} \text{ [m}^{-3}]$ ($3.0 < q_a < 5.2$) and shows a linear dependence on B_t , which is consistent with the L-H transition scaling law. Figure 4.17 (b) shows the $\langle n_e \rangle$ dependence of the calculated L-H transition power normalized by $\langle n_e \rangle$ for $B_t = 2.5$ [T], $I_p = 2.0$ [MA] ($q_a = 3.6$) and it is also almost linear, which is a little larger than that of L-H transition threshold power scaling law mentioned above, but the linear dependence on n_e is acceptable from the dimensional analysis point of view [4-31]. At last, we have to examine the independence of plasma current I_p . Figure 4.17 (c) shows the I_p dependence of the calculated L-H transition power with ion orbit loss (solid line, $C_2=0.11$) and without it (dashed line, $C_2 = 0.0$) in the case of $B_t = 2.5$ [T] and $\langle n_e \rangle = 3.0 \times 10^{19} \text{ [m}^{-3}]$. P_{th} for $1.6 < I_p < 2.2$ [MA] is almost constant, but for $I_p < 1.6$ it increases with I_p . The independence of I_p for the L-H transition power threshold power in the range of $1.6 < I_p < 2.2$ is a consequence of equation (4.31). Because the normalized collisionality, ν_* , decreases with I_p , this would normally result in the decrease of P_{th} like dashed line in Figure 4.17 (c), but

the poloidal Larmor radius decreases with I_p and results in a decrease in the orbit loss represented by the $(a - r)/\rho_p$ term in equation (4.31) causing P_{th} to increase like solid line in Figure 4.17 (c). Consequently, the two effects that are dependent on I_p cancel each other and the I_p independence can be reproduced. This effect is not investigated without 1.5-D transport code. According to comparison between with orbit loss effect and without it in Figure 4.17, the power of C_2 should be optimized in order to get an I_p independence of P_{th} . We need more optimized parameters C_1 and C_2 or better modeling than represented by equation (4.31) in order to demonstrate the independence of I_p in all regimes. Figure 4.17 expresses the possibility that Shaing L-H transition model based on ion orbit loss can reproduce the L-H power threshold scaling law, but we have to consider the assumptions applied in the calculation of P_{th} , that is, anomalous diffusive coefficients, temperature boundary conditions, given density profile and so on. These factors also may have critical effects on each global parameter dependence of P_{th} .

Figure 4.18 shows a comparison between the B_t dependence for the calculated P_{th} for the $\tau_E^{ITER89L}$ modified case ($\chi_{e,i} \sim B^{-0.2}$) and a Bohm type model case ($\chi_{e,i} = C_{e,i} \nabla P_e a q^2 / n_e B_t \sim B^{-1}$). The Bohm type model also reproduces the temperature profile of JT-60U L-mode discharges well [4-35]. The absolute values differ by about a factor of two, but the B_t dependence is almost the same in each case. We stress that the thresholds have almost the same B_t dependence in spite of the fact that the diffusion coefficients have different B_t dependences. As noted in the discussion of the I_p independence in Figure 4.17 (c), the B_t dependence of the thermal diffusion coefficient does not affect P_{th} dependence.

The consistency of the constant boundary condition ($T_i^{edge} = 2T_e^{edge} = 100[\text{eV}]$) with experimental observations is ambiguous. We examine the sensitivity of the threshold power to the boundary conditions by using $T_e^{edge} \sim n_e^{edge-0.3} B_t^{0.8} I_p^{0.5}$ as proposed by the ASDEX team [4-34]. Two cases are considered here. One is the constant $T_i^{edge} = 2T_e^{edge} = 100 [\text{eV}]$ case and the other is $T_i^{edge} = 2T_e^{edge} \propto B_t^{0.8}$ case with $T_i^{edge} = 2T_e^{edge} = 100 [\text{eV}]$ at $B_t = 2.0 [\text{T}]$. Figure 4.19 shows the effect of the temperature boundary condition on the B_t dependence of P_{th} for these two cases. The constant $T_{e,i}^{edge}$ case (solid line) is the same result as that in Figure 4.18. In the case of $T_{e,i}^{edge} \propto B_t^{0.8}$ (broken line), the B_t dependence of P_{th} becomes weaker than that of the constant $T_{e,i}^{edge}$ case and approximately yields $P_{th} \propto B_t^{0.67}$, which results from a decrease in the heating power to satisfy the L-H transition condition. This case shows a weaker B_t dependence than that of the L-H transition power threshold scaling law, but it is still within the uncertainty of the parametric dependence of $T_{e,i}^{edge} \propto B_t^{0.8}$. From the standpoint of verifying the L-H

transition model, the boundary condition at the separatrix is found to be important, and more precise data and experimental analyses, such as n_e^{edge} scaling studies proposed by the ITER R&D Divertor Group, are required to examine the L-H transition model more precisely.

4.3.5 Summary

We have carried out 1.5-D time-dependent transport simulations including Shaing L-H transition model. The calculated heating power needed for the L-H transition is the same order as in experimental results and the time scales for bifurcation of the poloidal Mach number and growth of the volume averaged temperature are also in agreement with experimental observations.

We have also compared the dependence of the power threshold on each plasma parameter with an L-H transition scaling law. Shaing L-H transition model agrees with the B_t and n_e dependence of the scaling law, but the I_p independence still needs to be examined more closely because of competing effects that may not cancel for the full range of H-mode experiments. In addition, we examined the sensitivity to thermal diffusivity and temperature boundary conditions. The effect of thermal diffusivity on the B_t dependence of P_{th} is weak in spite of different B_t dependencies in the thermal diffusion models. As for temperature boundary conditions, Shaing L-H transition model reproduces a B_t dependence similar to that of the L-H transition threshold power scaling law under the condition of $T_{e,i}^{edge} \sim B_t^{0.8}$. Though quantitative investigation is still needed to be carried out, Shaing L-H transition model based on ion orbit loss concept qualitatively has the potential to reproduce the L-H transition threshold power scaling law. It should be applied to individual scans on single machines and to a variety of experimental configurations for more detailed validation.

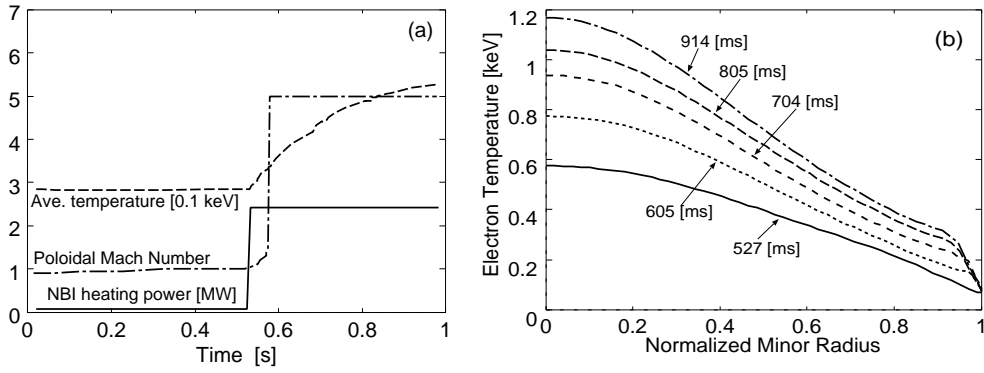


Figure 4.16: Time evolution of: (a) NBI heating power, poloidal Mach number at $r/a = 0.99$ and volume averaged electron temperature; and (b) the electron temperature profile.

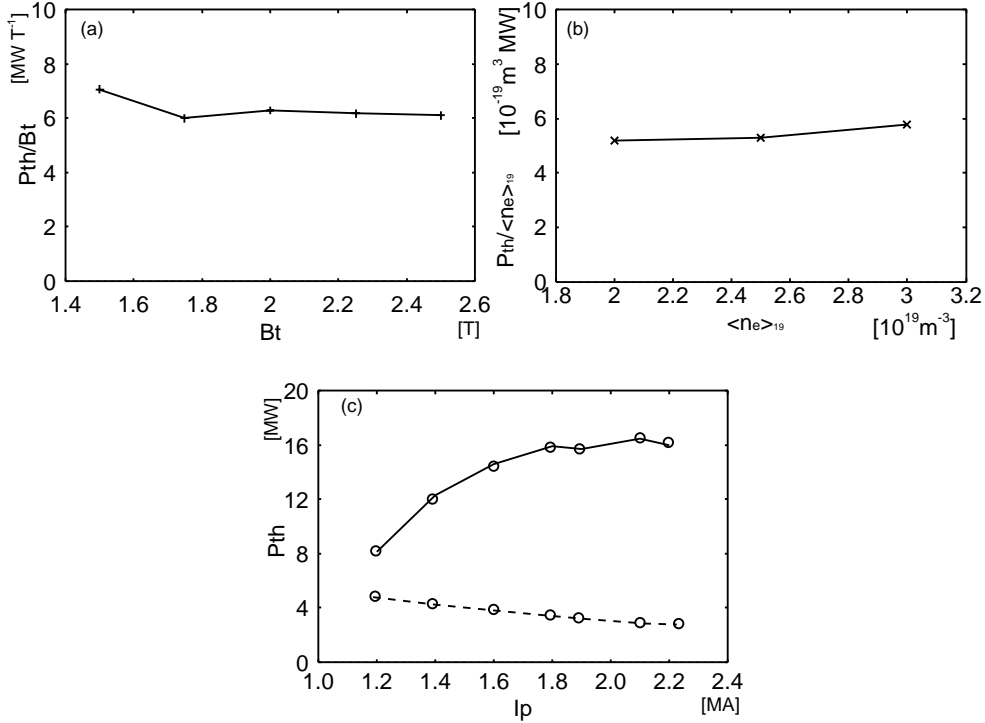


Figure 4.17: (a) Calculated P_{th} normalized by B_t . This result is for $I_p = 1.4$ [MA], $\langle n_e \rangle = 3.0 \times 10^{19}$ [m⁻³] ($3.0 < q_a < 5.2$). (b) Calculated P_{th} normalized by n_e for $B_t = 2.5$ [T], $I_p = 2.0$ [MA] ($q_a = 3.6$). (c) I_p dependence of calculated P_{th} for $B_t = 2.5$ [T] and $\langle n_e \rangle = 3.0 \times 10^{19}$ [m⁻³]. Solid line is derived from viscosity with ion orbit loss ($C_2 = 0.11$) and dashed line is without ion orbit loss ($C_2 = 0.0$).

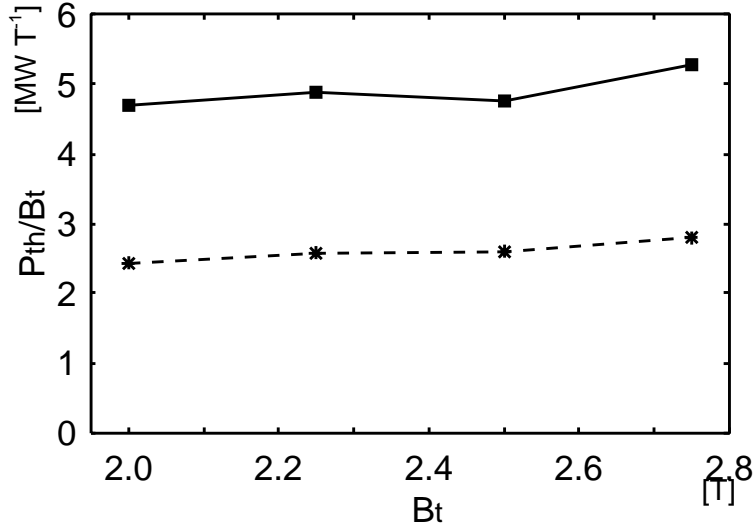


Figure 4.18: The effect of the anomalous thermal diffusion model: solid line is P_{th} normalized by B_t for $\tau_E^{ITER89L}$ modified model and broken line is for Bohm type model. The plasma parameters are $I_p = 1.6$ [MA] and $\langle n_e \rangle = 2.5 \times 10^{19}$ [m⁻³]

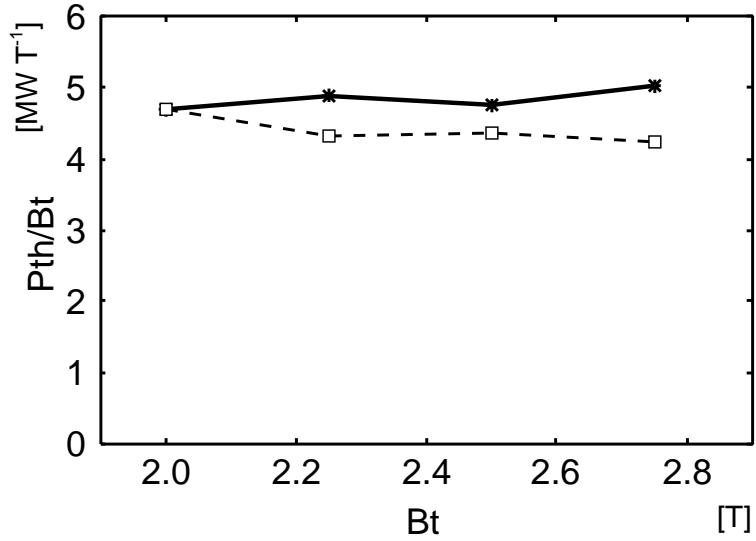


Figure 4.19: The effect of boundary conditions: solid line is P_{th} normalized by B_t for constant $T_{e,i}^{edge}$ and broken is line for $T_{e,i}^{edge} \sim B_t^{0.8}$. The plasma parameters I_p and n_e are the same as that of Figure 4.18.

4.4 Edge Plasma Transport Modeling

4.4.1 Introduction

Consistency of the edge plasma operation with the core plasma operation is an important issue for the design of ITER and the future fusion power plant. In case of the ITER divertor modeling, the fitting scaling laws for divertor plasma property are built with B2-Eirene code, and these are used as boundary conditions for the core plasma analysis[4-36, 4-37]. At present, such method is useful because each transport time scale for core and edge plasmas is different. On the other hand, that method is not applicable to analyze the broad region of plasma parameters for the future fusion power plant, because 2D divertor code such as B2-Eirene code requires the precise plasma geometry and heavy CPU time. For example, the core plasma conditions to generate net electric power are clarified[4-38]. Taking these core plasma conditions into account, we can consistently understand the operation conditions of the edge plasma for the fusion power plant. When we analyze such broad parameter region for the future fusion power plant, a simple model for the core-edge plasma transport is very useful to understand the overall C-S-D characteristics and to investigate operational region of future fusion reactors, especially, in the wide-range of parameter space. In this study, a simple Core-SOL-Divertor (C-S-D) model is developed to investigate the core and edge plasma operational space. Especially, we discuss how to integrate the C-S-D model with the 0D core plasma model and the two-point divertor model.

4.4.2 Physical models

Core plasma model

In the present paper, we apply the 0D plasma model based on ITER physics guidelines to the core plasma transport[4-39]. This model has been widely used in the ITER design and other reactor designs, when one roughly estimates the operational region for plasma parameters of a tokamak reactor as seen in ref. [4-40]. The global power and particle balance equations are as follows:

$$\frac{dW_p}{dt} = -\frac{W_p}{\tau_E} + P_\alpha + P_{OH} + P_{aux} - P_{Brad} - P_{sync} , \quad (4.36)$$

$$\frac{dn_j}{dt} = -\frac{n_j}{\tau_{pj}} + S_j , \quad (j = e, He) \quad (4.37)$$

where W_p is plasma thermal stored energy, and P_α , P_{OH} , P_{aux} , P_{Brad} and P_{sync} are the total powers of alpha particle heating, ohmic heating, additional heating, Bremsstrahlung loss and synchrotron radiation loss. The scaling law of the L-mode energy confinement time $\tau_E^{ITER89L}$ is applied to the energy confinement time $\tau_E = f_H \tau_E^{ITER89L}$, where f_H is the confinement improvement factor for H-mode. The particle confinement time τ_{pj} is defined by $\tau_{pj} = C_{pj} \tau_E$, where C_{pj} is the correction factor for each species. The fuel ion density is obtained by the charge neutrality condition. The L-H transition condition is installed by the same fashion as in ref. [4-41] in order to examine the consistency between H-mode and SOL conditions. We apply the experimental scaling law $P_{thr} = 2.76 M^{-1} B_t^{0.92} n_{20}^{0.77} R^{1.23} a^{0.76}$ [4-31] to the threshold power for H-mode, where M , B_t , n_{20} , R , and a are ion mass number, toroidal magnetic field, averaged electron density, major radius, and minor radius, respectively.

SOL-divertor model

The two-point model under the steady state condition can be applicable with time dependent core transport model, because the time scale of core plasma transport is much longer than that of SOL-divertor plasma transport. Figure 4.20 shows the basic features of density $n(z)$, temperature $T(z)$, and Mach number $M(z)$ along the field line in the edge region. The two-point model is constructed under the condition of constant temperature along the magnetic field in the SOL region. This two-point model also contributes to the parameter survey for the operational region of the SOL-divertor plasma for ITER and other reactor designs as seen in ref. [4-42]. Recently, this model is upgraded as the five point model to analyze the in-out divertor asymmetry [4-43]. Physical relationships of the two-point model in the present paper are as follows [4-44]:

$$\left(1 - f_{mom}^{div}\right) n_s T_s = \left(1 + M_d^2\right) n_d T_d , \quad (4.38)$$

$$\frac{7}{2} (1 - f_{imp}) L_s q_\perp = n_d M_d C_s (T_d) \Delta \left[\epsilon + (\gamma' + M_d^2) T_d \right] , \quad (4.39)$$

$$\Delta = \frac{5}{2} \chi_\perp \frac{n_s T_s}{q_\perp} , \quad (4.40)$$

$$\frac{1}{2} L_d^2 q_\perp = \frac{4\kappa_0 \Delta}{49} T_s^{7/2} \left[1 - \left(\frac{T_d}{T_s} \right)^{7/2} \right] , \quad (4.41)$$

where n and T are density and temperature. The subscript "s" and "d" express the upstream SOL and divertor region, respectively. The heat flux from the core plasma, temperature decay length, and Mach number at the divertor plate are defined by q_\perp , Δ ,

and M_d , respectively. The coefficients $f_{\text{mom}}^{\text{div}}$ and f_{imp} are the fraction of momentum loss and impurity radiation loss. The coefficient γ (~ 7.0) is the sheath energy transmission coefficient, and the heat load ϵ ($\sim 21.8\text{eV}$) on the plate comes from the recombination and radiation process [4-45]. Each equation is based on the following physics: 1. momentum balance at stagnation point and divertor plate of equation(4.38), 2. global energy balance in SOL and divertor regions of equation (4.39), 3.radial energy transport in SOL region of equation (4.40), and 4. electron thermal conduction along the field lines of equation (4.41).

4.4.3 Particle balance to determine the upstream SOL density

In order to integrate the core and edge plasma model, the upstream SOL density should be given in a self-consistent manner both for the core plasma and for the edge plasma. For this purpose, the particle balance equation in the SOL and divertor regions is used as shown in Figure 4.21. We assume that all neutral particles originate at the divertor plate at the rate proportional to the total particle flux to the divertor plate. Consequently, total neutral source rate at the edge region including gas puff term is as follows:

$$N_n = \frac{1}{2} \left(1 - \frac{1}{e^2} \right) n_d M_d C_s 2\pi R \Delta_n \sin(\psi) + N_{\text{puff}} , \quad (4.42)$$

where Δ_n is the density decay length. We assume that $\Delta_n = 2\Delta$. ψ is the angle of the magnetic field to the divertor plate. The term $(1 - 1/e^2)$ comes from the integration of the radial direction (from the separatrix to the density decay length Δ_n) on the divertor plate. By using the simple neutral model and the particle flux across the separatrix, Γ_{core} , from the 0-D core plasma calculation, the particle balance equation for the SOL-divertor region becomes

$$\Gamma_{\text{core}} S_{\text{core}} + N_n^{\text{sol}} + N_n^{\text{div}} = \frac{1}{2} \left(1 - \frac{1}{e^2} \right) n_d M_d C_s 2\pi R \Delta_n \sin(\psi) , \quad (4.43)$$

where $N_n^{\text{div}} = f_{\text{ion}}^{\text{div}} N_n$ and $N_n^{\text{sol}} = f_{\text{ion}}^{\text{sol}} N_n$. $f_{\text{ion}}^{\text{div}}$ and $f_{\text{ion}}^{\text{sol}}$ are the ionization fraction in the divertor and the SOL region, respectively. S_{core} is the core plasma surface normal to the particle flux. The ionization fraction in the divertor region, is modeled by

$$f_{\text{ion}}^{\text{div}} = 1 - \exp \left(- \frac{L_d \sin(\psi)}{\lambda_{\text{ion}}^{\text{div}}} \right) , \quad (4.44)$$

where $\lambda_{\text{ion}}^{\text{div}} = v_n / (n_d \langle \sigma v \rangle_{\text{ion}})$ is defined by the ionization cross section $\langle \sigma v \rangle_{\text{ion}}$, which is the strong function of T_d , and the neutral velocity $v_n = \sqrt{T_n/m}$. In the present paper,

the constant neutral temperature $T_n = 3$ eV is assumed. The ionization fraction in the SOL region is defined by

$$f_{\text{ion}}^{\text{sol}} = \frac{A_{\text{sol}}}{A_{\text{core}} + A_{\text{sol}} + A_{\text{pump}}}, \quad (4.45)$$

where A_{core} , A_{sol} and A_{pump} are the effective areas for the core region, the SOL region, and the pumping effect from the divertor region, respectively. In the present paper, the effective areas of A_{core} and A_{sol} are assumed by the each cross section area on the plasma midplane, i.e., $A_{\text{core}} = 2\pi Ra$ and $A_{\text{sol}} = 2\pi R\Delta_n$. The effective area of A_{pump} is defined by $A_{\text{pump}} = C_{\text{pump}}/(v_n/4)$, where C_{pump} is the speed of the pumping system[4-46], but pumping effect is not considered in this paper($C_{\text{pump}} = 0.0$). To specify these parameters more precisely, numerical analysis by multi-dimensional Monte Carlo neutral transport code will be done in the future.

To check the validity of this C-S-D model, comparison with the edge transport code (B2-EIRENE) is carried out. We focused on the JT-60U L-mode discharge in the high recycling state (Table 4.5)[4-47, 4-48]. The density and temperature of divertor-SOL region against the total particle flux across the separatrix Φ_p are shown in Figure 4.22 (a) and 1(b), where superscripts of "CSD" and "B2" corresponds C-S-D model and B2-EIRENE code, respectively. Qualitatively, the result of the C-S-D model is similar to that of B2-EIRENE. Quantitatively, the difference of temperature becomes large over $\Phi_p = 1.5 \times 10^{22} \text{ s}^{-1}$, mainly because B2-EIRENE result corresponds to the detached plasma state, which is not considered in the present C-S-D model. On the other hand, when n_s^{CSD} is equal to n_s^{B2} at about $\Phi_p = 1.3 \times 10^{22} \text{ s}^{-1}$, other parameters of the C-S-D model are also similar to those of B2-EIRENE. From this comparison, it is shown that the results by the C-S-D model are reasonable in qualitative sense. Around $\Phi_p = 1.0 \times 10^{22} \text{ s}^{-1}$ density of the C-S-D model suddenly increases in Figure4.22 (a) and temperature decreases sharply in Figure 4.22 (b), which is considered to be the transition from low to high recycling state[4-49]. That transition is confirmed by the sudden increase of the ionization fraction in the divertor region by the C-S-D model (Figure 4.22 (c)). The further quantitative validation of the C-S-D model including the low to high recycling phenomena remains to be done.

4.4.4 Application of C-S-D model to ITER

We apply the C-S-D model to the LH transition phase of ITER. The time evolution of core plasma parameters with the C-S-D model is shown in Figures 4.23 and 4.24. The density

increases at $t = 95$ sec in the L-mode state, and the auxiliary heating is added from $t = 100$ sec. The LH transition occurs at $t = 104$ sec when the total input power within the separatrix P_{in} becomes larger than LH threshold power P_{thr} as shown in Figure 4.24. These results around the LH transition phase are almost the same as the reference time evolution of ITER inductive operation[4-50].

The time evolution of SOL-divertor parameters with the C-S-D model is shown in Figure 4.25. The coefficients of C_{pj} and f_{ion}^{div} are calibrated so as to reproduce the $n_s \sim 0.33 \times 10^{19} \text{ m}^{-3}$, which is the reference upstream SOL density of ITER[4-50]. In Figure 4.25, there is an oscillation of n_d at the LH transition, which is caused from the oscillation of the particle and heat fluxes due to the change of core plasma confinement time. We should make clear whether such oscillation of divertor density at LH transition is observed in the experiment. If so, we should investigate whether this n_d oscillation has any effects on the divertor operation.

4.4.5 Summary

The C-S-D model has been developed to investigate overall and integrated feature, and it is applied to the LH transition phase of ITER. It is found that there is possibility of the oscillation of the divertor density n_d at the LH transition for ITER. If such n_s oscillation at the LH transition is observed in the experiment, we should investigate the effect of n_s oscillation on the divertor operation of ITER.

Table 4.5: Main plasma parameters of JT-60U L-mode discharge[4-47, 4-48]

JT-60U		
R/a	(m)	3.4/0.8
κ_{95}/δ_{95}	(-)	1.5/0.5
B_t	(T)	3.5
I_p	(MA)	1.8
Q_{in}	(MW)	2.5
L_s/L_d	(m)	50/3.0
f_{imp}	(-)	0.3

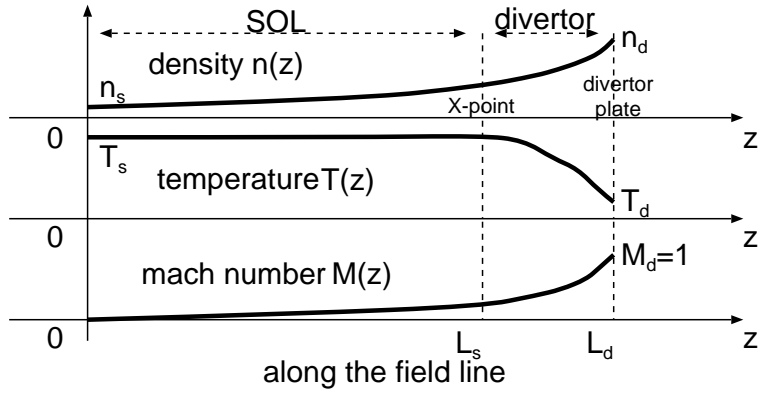


Figure 4.20: The density, temperature and Mach number along the field line in the SOL-divertor region.

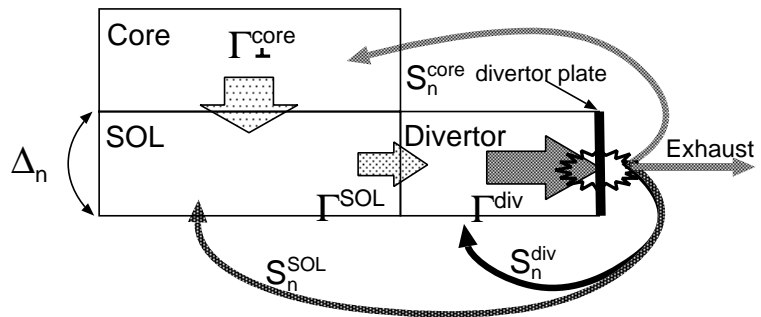


Figure 4.21: The model of the steady state particle balance.

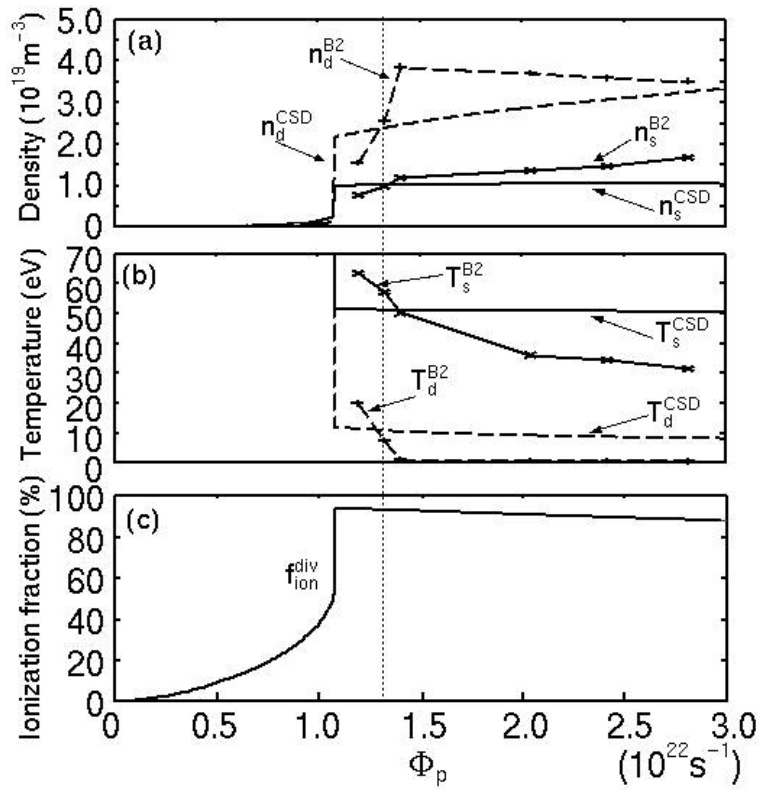


Figure 4.22: The SOL-divertor parameters vs. the total particle flux Φ_p : (a) density, (b) temperature by the C-S-D model and the B2-EIRENE, and (c) is the ionization fraction in the divertor region by the C-S-D model.

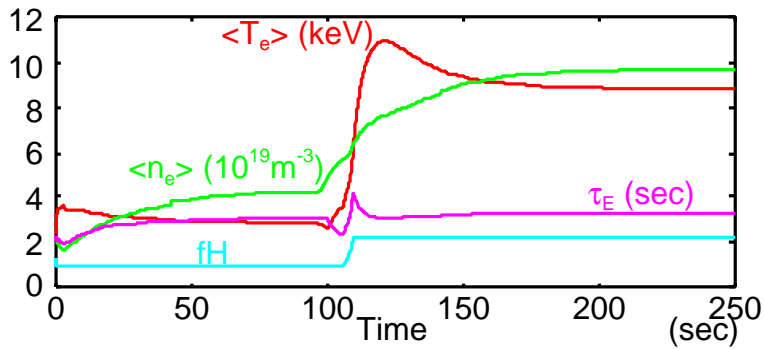


Figure 4.23: Time evolution of the ITER plasma parameters.

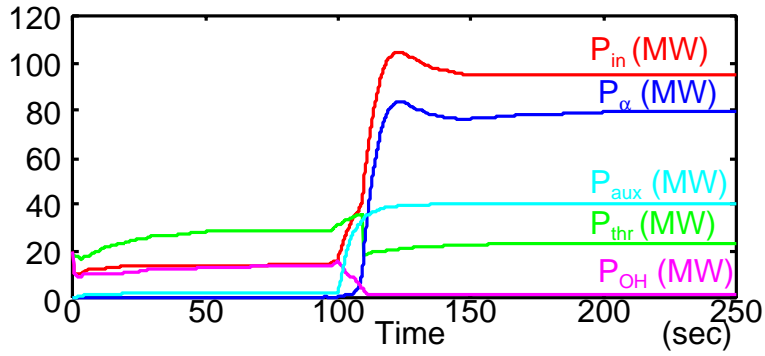


Figure 4.24: Time evolution of the ITER power balance.

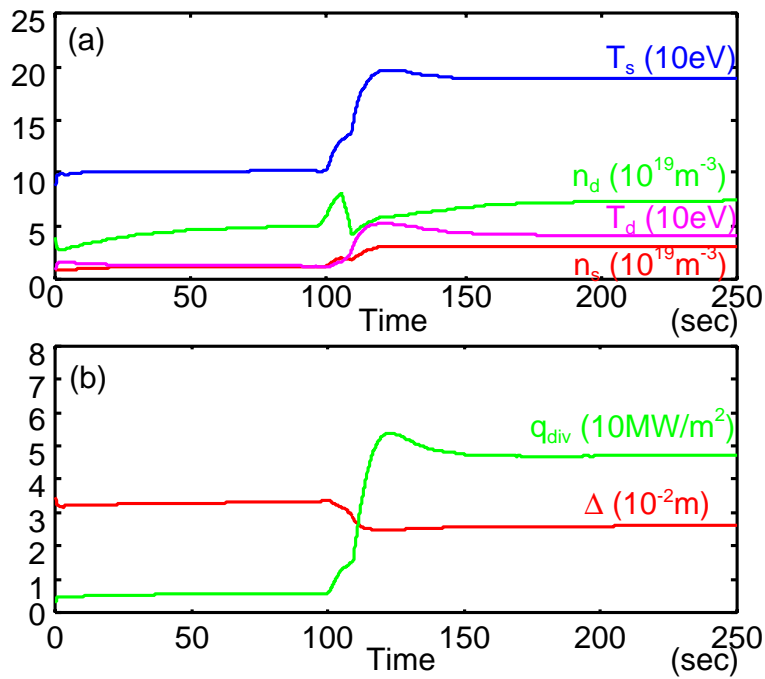


Figure 4.25: Time evolution of the SOL-divertor parameters for the C-S-D model: (a) density and temperature, (b) heat flux to the divertor plate and SOL width

4.5 MHD and Current Drive Analysis for Demonstration Power Plant

4.5.1 Mission of the electric demonstration plant

As discussed in Section 4.1, the critical issue of the electric demonstration plant Demo-CREST is considered as 'MHD & Current Drive' at present, because the electric demonstration plant Demo-CREST has a unique mission. While a commercial reactor usually has a rated operation point, the electric demonstration plant such as Demo-CREST requires a operation path from ITER-like plasma performance to advanced plasma one in order to achieve the outlook for the commercial power plant. Establishment of this operation path is considered as the mission of the electric demonstration plant. In this section, the operation path consistent with MHD stability and current profile alignment by single NBI system is confirmed by the MHD stability analysis code and current drive analysis code.

4.5.2 MHD and current drive analysis

The first point to be confirmed is the MHD stability of operation points (OP1-OP4) for Demo-CREST. MHD stability analyzed in this section are low n ideal kink stability, high n ballooning stability, and the Mercier criterion, and the 2-D MHD stability analysis code EQLAUS/ERATO[4-51, 4-52] is applied to this analysis. The second point is the consistency of current profiles between driven current, bootstrap current, and total plasma current. That consistency is examined with the current drive analysis code DRIVER88[4-53]. In this section, a plasma elongation $\kappa = 1.85$ and triangularity $\delta = 0.35$, which is a little smaller than that of 0D analysis in the previous section, are applied respectively. In addition, a safety factor on plasma surface is assumed about 5.0 except for the advanced plasma case toward a commercial power plant.

The result of MHD stability and current drive analysis is shown in Figure 4.26. The operation parameters of OP1-OP4, which are also confirmed with the DRIVER88 about current drive property, are listed in Table 4.6. In the Demo-CREST, plasma performance is improved from OP1 to OP4, step by step. The conducting wall is located at $a_{\text{wall}} = 1.3a_p$, which is considered to be outside the breeding blanket in the first phase. The stability limits for $n = 1, 2$ kink mode (ballooning mode) are delineated with broken lines (one-point dashed line) in Figure 4.26. The operation points corresponding to OP1-

OP4 are also plotted in Figure 4.26. All operation points are in the stable region. The normalized beta value for Demo-CREST can be raised up to about 3.5 with a normal shear configuration by increasing the central safety factor. An increase of the central safety factor with a constant surface safety factor implies that the current profile broadens for the high β_N . This operation method from OP1 to OP4 is consistent with increase of bootstrap current, which is mainly induced in the periphery region. At the same time, the plasma density is increased from OP1 to OP4 as listed in Table 4.6. The operation points with reversed shear configuration, which are surrounded with the dotted line, are also plotted in Figure 4.26 and these points are discussed in the following section.

The current drive analysis is carried out for the stable operation points, OP1-OP4 described in Figure 4.26. Those stable equilibrium data include the alpha and beam component of plasma pressure profile. The optimized profiles of safety factor, plasma current, and plasma pressure corresponding to respective reference operation points are shown in Figure 4.27. At the initial operation point OP1 corresponding to $\beta_N = 1.9$, the fraction of bootstrap current is small. With increasing β_N , more bootstrap current is induced in the plasma edge region. Consequently, the fraction of bootstrap current increases, and beam pressure and driven current decrease. On the other hand, current drive power is almost constant as shown in Table 4.6, because of increase of plasma density. The NBI deposition profiles of operation points OP1-OP4 are also described with two beam input regions of on- and off-axis beam on plasma cross section in Figures 4.28. These results are consistent with the driven current profile, which is needed to sustain the stable current profile. Figure 4.28 reveals that less off-axis beam power is required than about 30 MW in the range of $1.9 \leq \beta_N \leq 3.4$. Under the present assumption for NBI input power per unit system, off-axis beam power will be satisfied with one unit NBI system.

4.5.3 Prospect toward the commercial plant

The prospect toward a commercial plant should be obtained with the electric demonstration plant Demo-CREST, because of the single step to the commercial plant. In this section, we consider CREST[4-54] as the commercial plant. The plasma parameters are shown in Table 4.6.

As mentioned in Section 3.3.2, the way to improve the plasma performance in Demo-CREST is to increase the energy multiplication factor with a constant fusion power. Simply speaking, the fraction of bootstrap current should be increased with higher β_N

and total current drive power should be decreased. Accordingly, the reversed shear configuration is supposed to be suitable. In the Demo-CREST design, the reversed shear configuration with $\beta_N = 4.0$, $\kappa = 1.85$, and $\delta = 0.35$ is confirmed as the operation point of OPRS in Figure 4.26 and Table 4.6. The profiles of safety factor, current, pressure and beam deposition for OPRS are shown in Figure 4.29. This improvement results in increase of $Q \sim 15$ with the same fusion power. When the plasma elongation $\kappa = 2.0$ and triangularity $\delta = 0.5$ will be taken in Demo-CREST, $\beta_N \sim 5.0$ of operation point CREST-like can be theoretically obtained as shown in Figure 4.26, because the plasma shape of Demo-CREST can be similar to that of CREST. It should be noticed that the conducting wall has to be located at $a_w = 1.15a_p$ so as to avoid the low n kink instability. The location of $a_w = 1.15a_p$ is in the breeding blanket. Consequently, the blanket system has to be replaced with the advanced one for the reversed shear configuration. Of course, steady state operation of reversed shear plasma with $\beta_N \geq 4.0$, which is probably difficult for the ITER with the wall location $a_w \sim 1.35a_p$ [4-55], has to be experimentally confirmed with another support device, e.g. JT-60 superconducting tokamak proposed in Japan[4-56].

Simultaneously, the thermal efficiency has to be also increased with the advanced blanket system to examine the economic prospect toward the commercial plant. When it increases up to 40%, the net electric power of operation point OPRS can roughly result in more than 1000 MW. Which kind of blanket system should be selected will depend on the progress of its R&D activity, i.e., through the ITER and IFMIF program[4-57]. The advanced blanket system with an inner conducting wall for $\beta_N \geq 4.0$. and $\eta_e = 40\%$, which can also keep tritium breeding ratio $TBR > 1.0$, is discussed in [4-58].

The consideration above implies that there should be two development phases of Demo-CREST to get the prospect to the commercial plant. The first phase is named “Demonstration phase”, and the latter is “Development phase”. The Demonstration phase corresponds to the demonstration of net electric power generation as a power plant, which is the second stage mentioned in Section 1.4. The technologies applied in the initial phase are established in the ITER program. During this phase, we have to establish how to operate efficiently and how to maintain the system including the replacement of a blanket system. The second phase corresponds to the demonstration of advanced technologies for the economic prospect. During the initial phase, plasma physics and engineering technologies are supposed to be advanced in the ITER and IFMIF programs. Such technologies, e.g., high beta reversed shear operation, advanced blanket system with advanced materials for high thermal efficiency, simple maintenance methods, should be

demonstrated in the second phase. This Development phase mainly corresponds to the third stage in Section 1.4. It is advantageous for a tokamak fusion reactor to improve both of plasma and engineering performance by only replacing the blanket system. With this operation plan of Demo-CREST, the physical and engineering elements required in the design of CREST can be demonstrated in Demo-CREST. This is why we can combine the usual demo and proto-type stages into a single step of Demo-CREST. We propose the development path with ITER, Demo-CREST, and CREST as an example for early realization of net electric generation by fusion energy. To complete this development path, the required development element concerning plasma physics, engineering technology and maintenance process in each stage is being assessed precisely.



4.5.4 Summary

In this section, MHD stability and current drive analysis were carried out to confirm the operation path from the ITER-like plasma ($\beta_N \sim 1.9$) to the CREST-like plasma ($\beta_N \sim 4.0$) with the same NBI heating system. To achieve the CREST-like plasma, two operation phase is considered as shown in Table 4.7. The initial phased named “Demonstration phase” focuses on the demonstration of net electric generation as a power plant. The latter phase named “Development phase” focuses on improving plasma performance and reactor technology similar to the commercial reactor CREST. In the development phase, the advanced blanket system with conducting shell for kink mode will be replaced from the conventional one based on the ITER test blanket module. With such development method, operation path consistent with MHD stability and current profile control is confirmed, and the net electric power similar to CREST can be finally achieved as shown in Table 4.7.

Table 4.6: Representative operation points of Demo-CREST confirmed by EQLAUS/ERATE[4-51, 4-52] and DRIVER88[4-53].

		OP1	OP2	OP3	OP4	OPRS	CREST
β_N	(-)	1.9	2.5	3.0	3.4	4.0	5.5
R_p/a_p	(m)	7.25/2.13	←	←	←	←	5.4/1.59
κ/δ	(-)	1.85/0.35	←	←	←	←	2.00/0.50
I_p	(MA)	15.9	15.4	15.6	14.7	13.2	12.0
f_{bs}	(-)	0.24	0.34	0.40	0.50	0.73	0.83
q_ψ	(-)	5.0	5.0	5.0	5.2	6.5	4.3
q_0/q_{min}	(-)	1.3/-	1.7/-	2.1/-	2.3/-	3.8/3.6	2.9/2.4
β_p	(-)	1.11	1.55	1.86	2.15	2.84	2.5
B_t	(T)	8.0	8.0	8.0	7.8	8.0	5.6
$\langle T_e \rangle$	(keV)	17.9	18.7	20.7	18.4	17.3	15.4
$\langle T_i \rangle$	(keV)	18.8	19.5	21.5	19.2	18.2	16.4
Z_{eff}	(-)	1.7	1.7	2.1	2.1	2.1	2.2
$\langle n_e \rangle$	($10^{20}m^{-3}$)	0.625	0.789	0.873	1.05	1.21	2.1
fn_{GW}	(-)	0.56	0.73	0.80	1.0	1.3	1.3
H/HH_{98}	(-)	1.5/0.96	1.7/1.1	1.9/1.2	2.0/1.2	2.4/1.4	3.2/1.3
E_b	(MeV)	1.5	1.5	1.5	1.5	1.5	2.5
P_{NBI}	(MW)	188	190	185	191	107	97
on axis		164	163	157	166	93	35
off axis		24	27	28	25	14	62
P_f	(MW)	1260	1940	2460	2840	3160	2970
Q	(-)	6.7	10.2	13.3	14.9	29.7	31
P_e^{net}	(MW)	30	230	390	490	1050	1163

Table 4.7: Development of net electricpower in Demo-CREST

		Development of reactor technology 			
		ITER Major radius 6.2m Max. magnetic field 13T	Demo-CREST Major radius 7.3m Max. magnetic field 16T		CREST Major 5.4m Max. magnetic field 13T Thermal efficiency 41%
			<u>Demonstration phase</u> Thermal efficiency 30%	<u>Development phase</u> thermal efficiency 40%	
Development of plasma 	ITER Reference plasma	(demonstration of burning plasma)	0MWe		
	ITER Advanced plasma	(development of the plasma required for a power plant.)	500MWe	900MWe	
	CREST Advanced plasma			1100MWe	1200MWe (COE: 60mill/kWh)

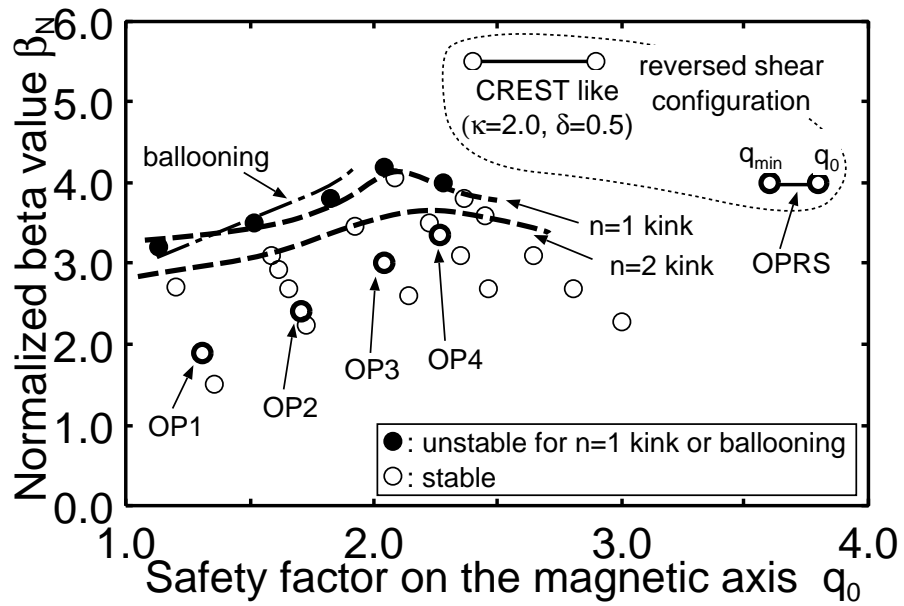


Figure 4.26: MHD stability analysis result on β_N - q_0 space. Stable points of Demo-CREST are plotted with open circles (\circ). Unstable points are black circles (\bullet), and stability limits for n=1,2 kink mode and ballooning mode are delineated with broken lines. Operational points with reversed shear configuration, OPRS and CREST like, are also plotted in the dotted region.

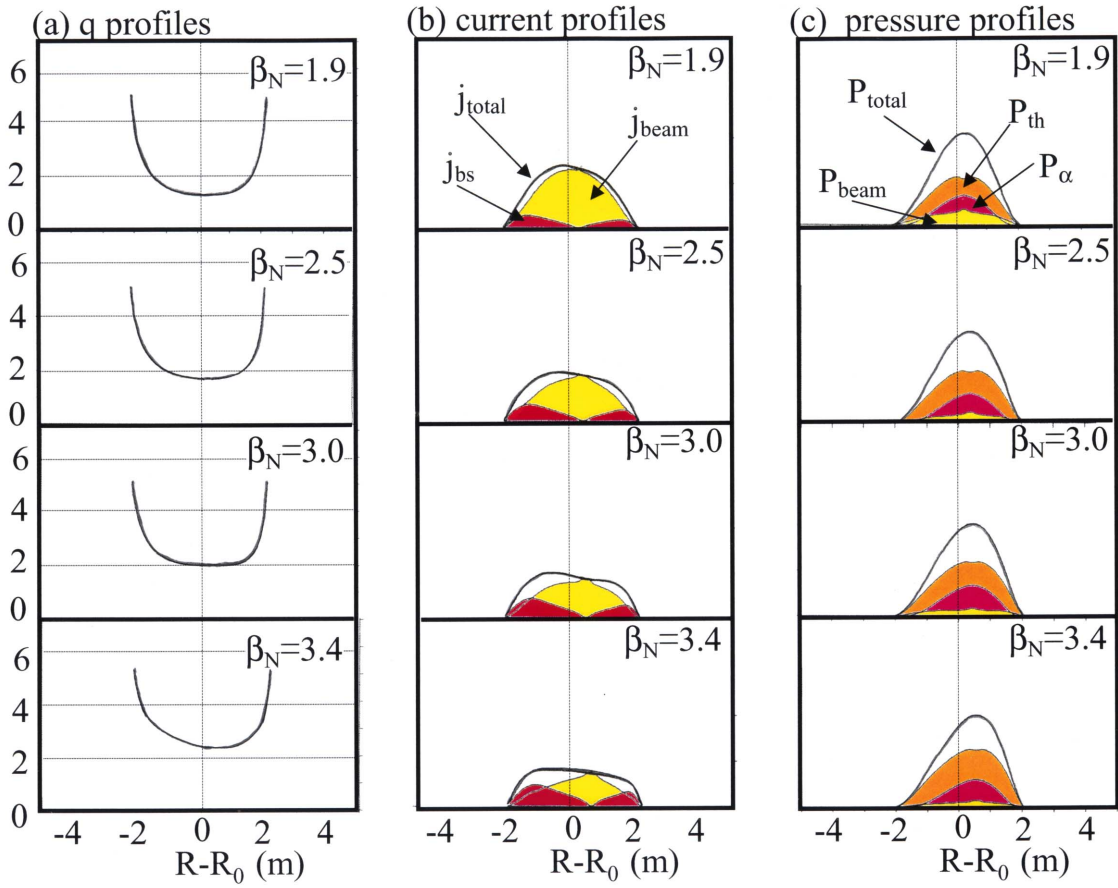


Figure 4.27: Safety, current, and pressure profiles for operation points (from OP1 to OP4) of Demo-CREST.

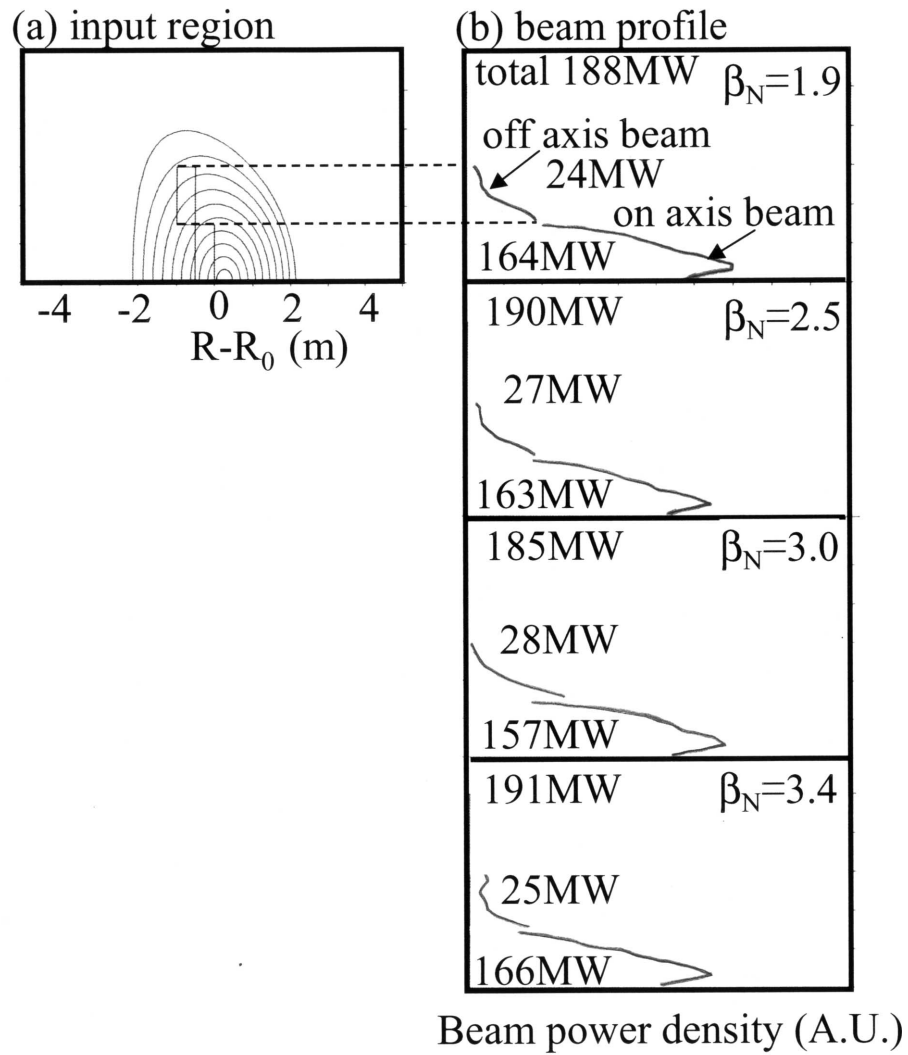


Figure 4.28: NBI deposition profile for each operation point of Demo-CREST.

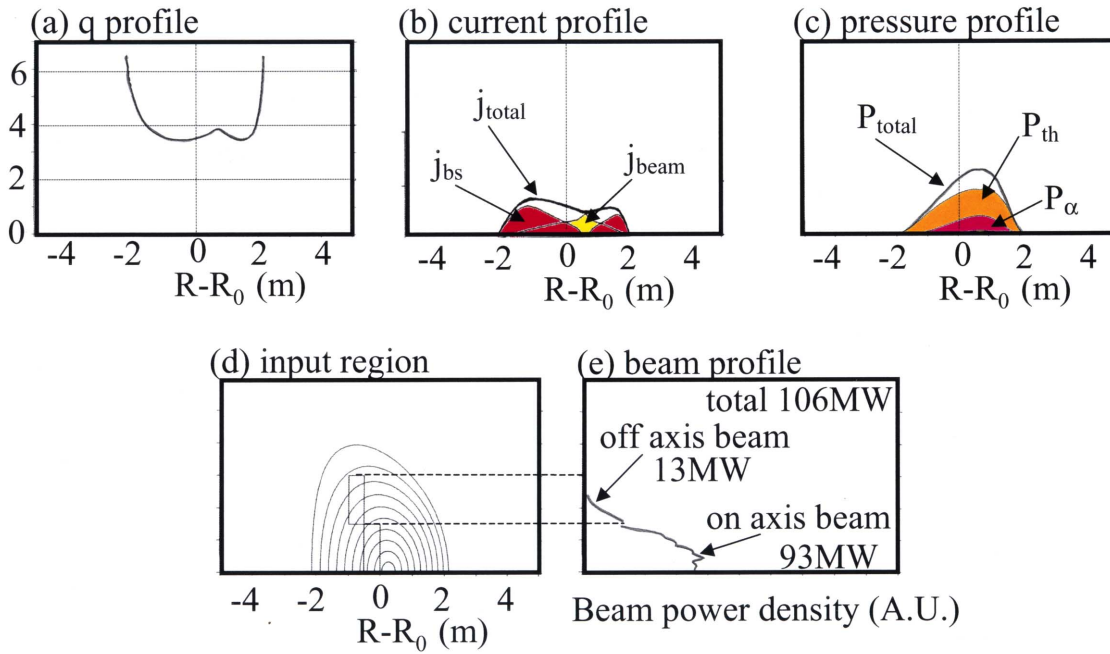


Figure 4.29: Profiles of safety factor, current, pressure, and beam deposition for a reversed shear configuration with $\beta_N = 4.0$ of Demo-CREST.

4.6 Operation Condition Analysis for Highly Elongated Advanced Plasma

4.6.1 Consistent control of current profile and plasma elongation

The economical and environmental attractiveness are required for fusion power plants. Our economical analysis for fusion power plants reveals that the most important plasma parameter is the normalized beta value β_N , and that the normalized beta value is needed to be about 5.0 in order to achieve the competitive cost of electricity[4-59, 4-38]. The reversed shear plasma has the potential to realized such high β_N [4-60], and experimentally was confirmed by TFTR and D-IIID[4-61, 4-62]. The plasma shape control also has a great impact on the plasma performance. High elongation is essential for the high β_N , and high triangularity has also found to be a good effect on the plasma performance from the experimental view point, for example, DIII-D and JT-60U[4-63, 4-64, 4-65].

Recently, several conceptual designs of the future DEMO or the commercial fusion reactor based on the reversed shear and high elongated plasma, that is, Advanced Tokamak, are proposed such as CREST[4-54], ARIES-AT[4-66] and A-SSTR2[4-67]. They includes the scope of an economical and safety view points in order to be accepted as one of the attractive energy sources in the future. In the former two designs, it is supposed to be possible to achieve high $\beta_N = 5 \sim 6$ as the result of the full potential exertion of the reversed shear plasma. In the last design, it is a little more conservative than the formers, but it is also based on the reversed shear plasma and other advanced engineering techniques, that is, high toroidal magnetic field with a high temperature superconductor.

On the other hand, the pursuit of the advanced plasma makes the plasma operation difficult such as the current profile control, the plasma shape control and the plasma position control. The analytically simulated result for the positional instability considering the passive and active coils shows that the elongation is attainable to 2.3 in the reversed shear discharge of the triangularity $\delta = 0.5$ and the internal inductance $l_i = 0.3$ [4-68]. This result is considered as the ideal case for control of the positional instability. Indeed, its consistency with the engineering condition such as blanket design (tritium breeding ratio, the position and shape of the stabilizing coils and so on) should be confirmed in the design of the future devices, the upper limit of the elongation in ref.[4-68] is considered as a challenging guidepost. This result also implies that the simultaneous control of plasma shape and current profile is inevitable during the plasma ramp-up phase, be-

cause a discharge usually starts from the circle plasma and the peaked current profile. The controllability and operation space of the plasma elongation and the plasma current profile is considered as a key issue in the future devices.

CREST is a cost competitive fusion reactor concept design based on the reversed shear plasma configuration with the major radius 5.4 (m), the aspect ratio 3.4, the elongation 2.0, the triangularity 0.5, the total plasma current 12 (MA) and normalized beta value 5.5[4-54]. Figure 1.5 shows the bird's-eye views for CREST. In the CREST design, positional instability is stabilized by the control coils which are located just outside the outer shield, but the stability margin with active and passive control coils is not large. On the other hand, because of the nature of a reversed shear configuration, the kink stabilizing shell is installed into the tritium breeding blanket, and it is supposed to be effective on positional instability from the theoretical view point. The effect of the kink stabilizing shell has the possibility to enlarge the stability margin for positional instability and to enlarge the plasma elongation. In this study, the detailed analysis including the kink stabilizing shell is carried out, and we make clear the possibility of elongation over 2.0. Furthermore, the operational space for the positional instability on the plasma elongation and the internal inductance space during the current ramp-up phase is also discussed.

4.6.2 Analysis method

In the present paper, we consider only the vertical motion of plasma column for simplicity. The equation of motion of displacement for the plasma column in the vertical direction, Z_p , is described as follows,

$$M_p \frac{\partial^2 Z_p}{\partial t^2} = -2\pi R_p I_p \left(-\frac{nB_{Z0}}{R_p} Z_p + \sum_i \nu_i I_i \right) \quad (4.46)$$

where M_p and R_p are the plasma mass and the major radius of the plasma column, I_p and I_i are the total plasma current and the current of the i -th eddy current mode, ν_i is the average radial field of the unit current of the i -th eddy current mode which defined as follows,

$$\nu_i = -\frac{M'_{pi}}{2\pi R_p} \quad (4.47)$$

where M'_{pi} is the Z -derivatives of mutual inductance between the plasma and the i -th eddy current mode. The circuit equation of the eddy current modes is

$$\tau_i \dot{I}_i + I_p M'_{pi} \dot{Z}_p + I_i = 0 \quad (i = 1, \dots, N). \quad (4.48)$$

By the Laplace transformation of equations(4.46) and (4.48), we derive the stability criterion for the vertical instability as follows,

$$n + n_s > 0 \quad (4.49)$$

$$n = - \int_p \frac{\partial B_R^{ext}}{\partial Z} \frac{j_p R}{I_p B_{Z0}} ds \quad (4.50)$$

$$n_s = \sum_i \frac{n_i s \tau_i}{1 + s \tau_i} \quad (4.51)$$

$$n_i = -M_{pi}'^2 I_p / 2\pi B_{Z0} \tau_i \quad (4.52)$$

where τ_i is the time constants for the eddy current mode,

B_R^{ext} and B_{Z0} are the equilibrium radial external field and the vertical field at the plasma center, which is calculated by the plasma equilibrium code, TOSCA[4-69]. The stability for the positional instability is estimated by the eddy current analysis code, EDDYCAL[4-70].

4.6.3 Analysis Results for CREST

The CREST design is a proposition of a fusion power plant based on the maximum β_N derived theoretically with the reversed shear configuration, which shows the possibility to realize a cost competitiveness with another energy sources[4-54]. The main parameters of CREST are listed in Tab.1.1 and the poloidal cross section of CREST is shown in Figure 4.30. CREST plasma is sustained by NBI current drive and MHD stability for ideal kink for $n = 1, 2$ and 3, ballooning and Mercier modes is confirmed by a 2-D ideal MHD code, EQLAUS/ERATO[4-51, 4-52]. As for positional instability, five control coils are located just out side the shielding blanket and the stability margin of positional instability, $m_s = -(n_s + n_i) / n_i$, is about 0.1 for CREST. The larger m_s value is more favorable.

As mentioned in Section 4.6.1, kink conducting shells are installed in CREST as shown in Figure 4.30. The detailed analysis of positional instability is carried out including these kink conducting shells. Figure 4.31 shows the dependence of shell stabilizing factor, n_s , on the growth rate of the positional instability for CREST. The kink stabilizing shells are made of Zr because shell is located in the breeding blanket and Zr has the good penetration of neutron for keeping tritium breeding ratio (TBR) high. The control coils, which are made of Cu, are also located just out side the outer shield. These resistance and thickness are listed in Table 4.8. The stability condition is obtain only by the control coils around the growth ratio, $\gamma_{th} \sim 4$. The shell stabilizing effect follows in the range

of $\gamma > 10$ and contribute to increase the stabilizing margin, $m_s = -(n + n_s)/n$. The stabilizing margin with the kink shell effect is about 5 times as large as that without the kink shell effect.

In the advanced tokamak reactors such as CREST, the bootstrap current is the large part of the total plasma current. Consequently, total plasma current profile results in a hollow profile. However, we dare to suppose that the current profile is controllable and examine the effect of current profile on the positional instability for CREST. Figure 4.32 shows the analysis results for the peaked current profile with internal inductance, $l_i = 0.9$. γ_{th} increased about 400, which means the power for the active position control is not negligible in comparison with NBI current driving power. The indispensable prerequisite for the growth rate, γ_{th} , is roughly considered as $\gamma_{th} \leq 50$ [1/s][4-71]. According to this results, the current profile in the advanced tokamak with high beta and high elongation such as CREST is supposed to be needed to control at the plasma ramp-up phase because the initial plasma current profile is peaked.

4.6.4 Criterion for current profile control at the ramp-up phase

As long as we consider the tokamak configuration as the future fusion reactors, the fraction of the bootstrap current will be large because of the reduction of the power for driving the plasma current, which means that the current profile is mainly determined by the bootstrap current resulted from the plasma transport phenomena in the steady state. Increase of bootstrap current results in more hollow current profile, which is effective on positional instability. But as mentioned in the previous section, plasma position is found to be unstable in case of the peaked current profile, which means that we have to pay attention to the current profile control during plasma ramp-up phase because the plasma current is peaked at the beginning of discharges. In order to confirm the stable plasma ramp-up, firstly, we have to make a series of equilibriums during plasma ramp-up phase in order to confirm the plasma ramp-up scenario.

In CREST case, a plasma heating and current driving method is NBI (Neutral Beam Injection). The heating area with NBI are fixed in the plasma poloidal cross section. The one is plasma upper region with 35MW and the other is plasma lower region with 65MW as shown in Figure 4.33. The lower region enables to achieve the high confinement plasma earlier than the upper region because of higher heating power. The thermal control is also important problem because CREST is relatively compact, which is almost as same as ITER-FEAT, and its fusion power is 5 times as large as that of ITER-FEAT.

That means that the transform from limiter configuration to divertor one is needed as earlier as possible. Considering two requirements mentioned above, a series of plasma equilibrium is established as shown in Figure 4.34. The initial plasma with elongation 1.0 is discharged around 65 [MW] NBI heating region and plasma elongation is gradually increased as shown in Figure 4.34. Poroidal beta value and total plasma current are gradually increased from 0.2 to 2.5 and from 1.0 to 12.0 [MA], respectively. The configuration change from limiter configuration to divertor one occurs at around $\kappa = 1.5$

Under the condition that the time evolution of plasma equilibrium in the ramp-up phase is as in Figure 4.34, the analysis of positional instability is carried out and stable region in the $\kappa - l_i$ plane is made clear as shown in Figure 4.35. The unstable region is $\kappa \geq \sim 1.5$ and $l_i \geq \sim 0.7$. The initial point is considered to be around $\kappa \sim 1.0$ and $l_i \sim 1.0$ and the steady state operating point is $\kappa \sim 2.0$ and $l_i \sim 0.55$. We find the criterion for plasma profile control of CREST at the current ramp-up phase considering only the positional instability. We have to change from the peaked plasma current profile to the hollow one before attaining elongation $\kappa = 1.5$. As mentioned in Section 3.2, the fraction of bootstrap current has the great impact on the total plasma current profile as for the advanced tokamak such as CREST. The route from the initial plasma ($\kappa \sim 1.0$ and $l_i \sim 1.0$) to operated plasma ($\kappa \sim 2.0$ and $l_i \sim 0.55$) is closely concerned to the plasma transport process, especially, the plasma confinement. To find the way to operate without acrossing instable region, we have to carry out the transport analysis and examine the consistency between dominated parameters, κ and l_i , and plasma confinement. This restriction is not specialized only to CREST but common problem to the advanced tokamak with a high β_N and highly elongated plasma.

4.6.5 Summary

The stabilizing method for the positional instability such as the installation of control coils and shells has to keep the consistency with engineering factors, for example, tritium breeding ratio, the structure of blankets and so on. In this section, we derive the criterion for the control of the current profile of CREST which can lead the stable ramp-up scenario, which is to change from the peaked current profile to the hollow current profile before attaining the plasma elongation, $\kappa = 1.5$. The operation guideline is applicable not only CREST plasma but also other elongated plasma for a commercial power plant such as ARIES-AT, while stable operation boundary for plasma elongation has to be optimized.

Table 4.8: Resistivity and thickness for control coils and shell

	Control Coils	Shell
Material	Cu	Zr
Resistivity [$\Omega \cdot m$]	1.55e-08	8.8e-07
Thickness [m]	0.05	0.01

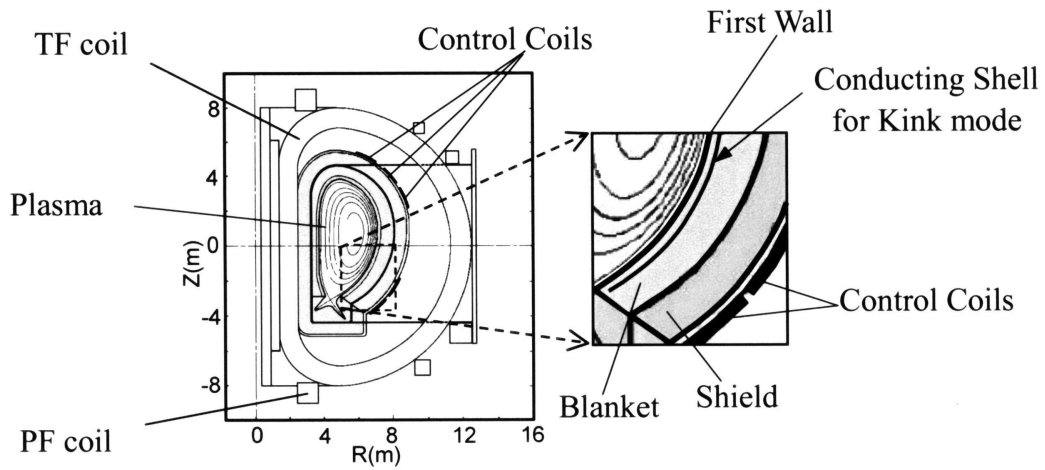


Figure 4.30: Cross section of CREST

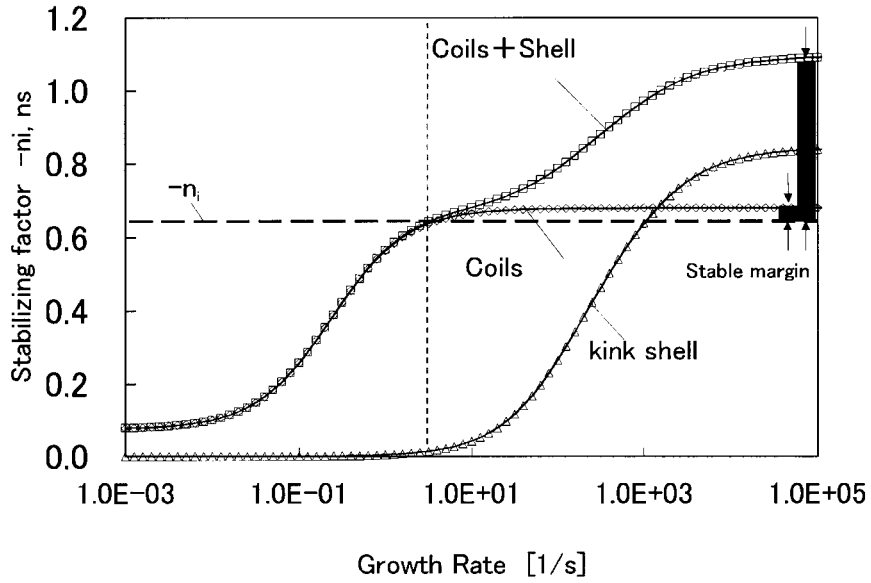


Figure 4.31: The relationship of stabilizing factor and growth rate of positional instability

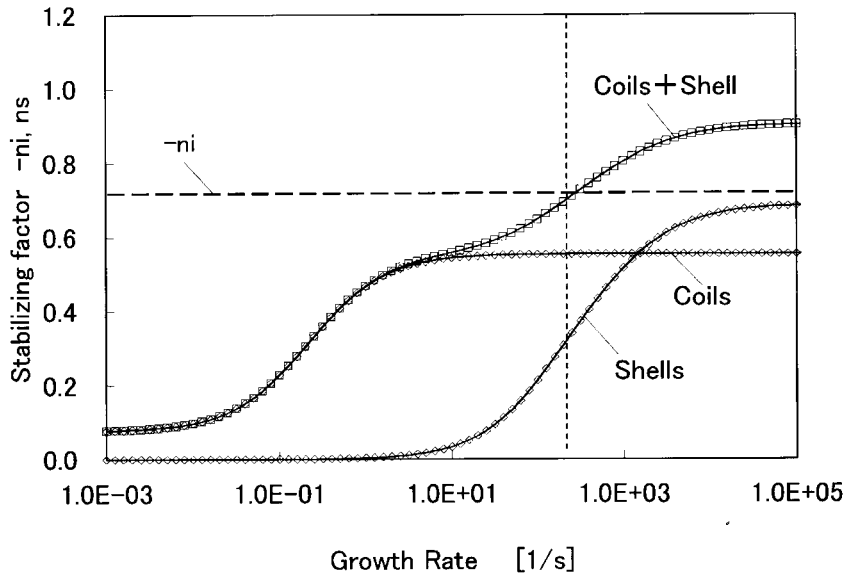


Figure 4.32: n_s v.s. growth rate at $l_i = 0.90$

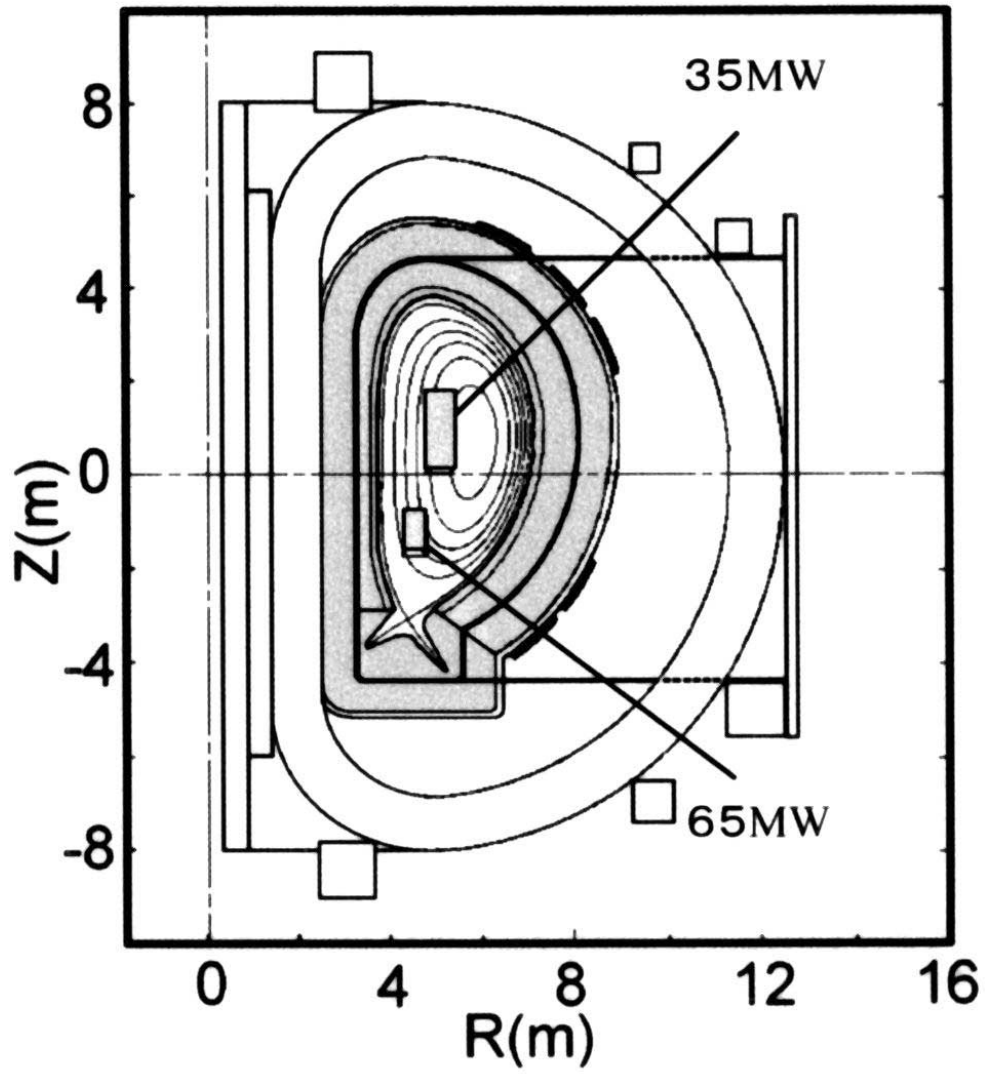


Figure 4.33: NBI heating region of CREST

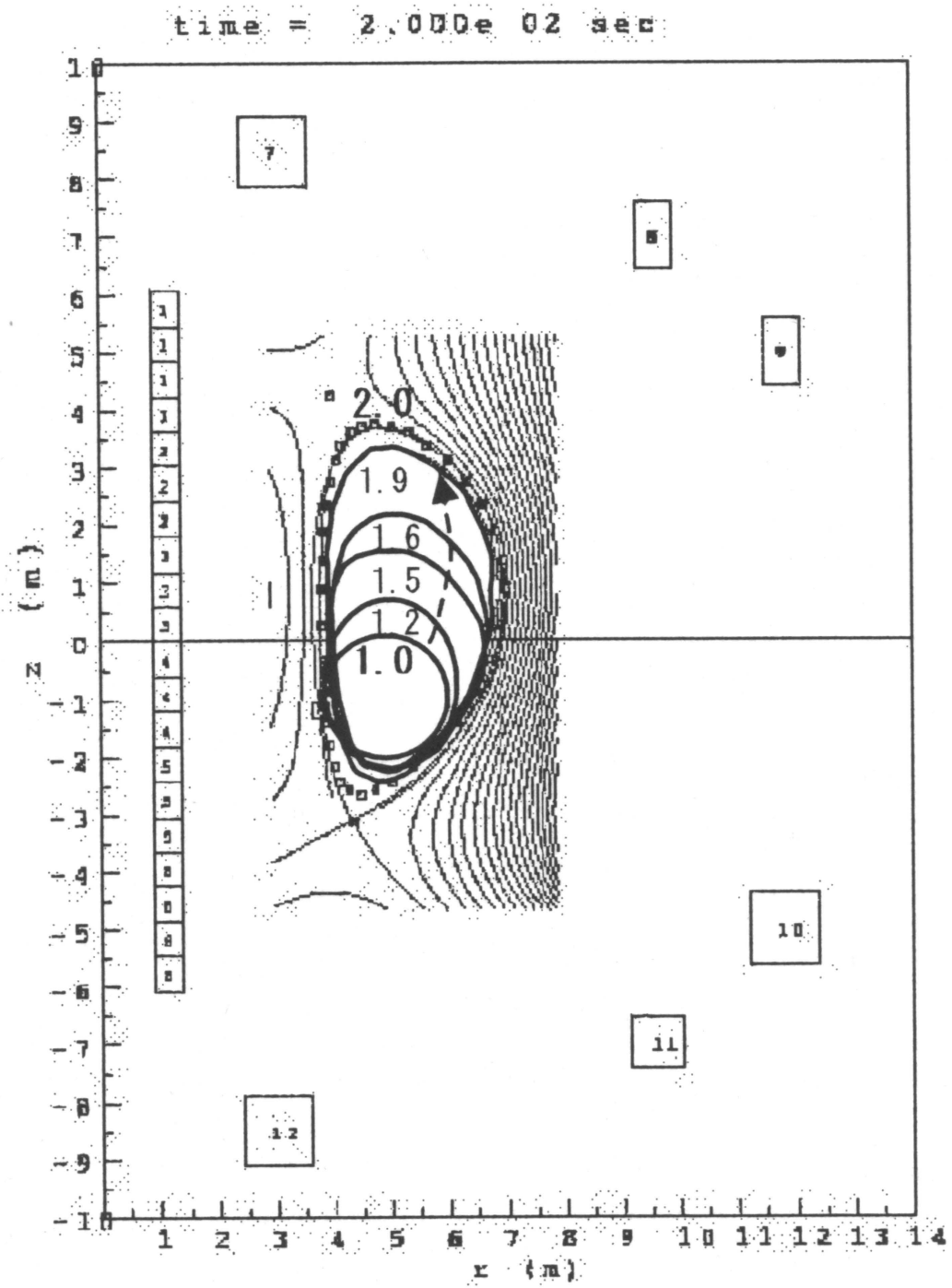


Figure 4.34: Current ramp up configuration in CREST

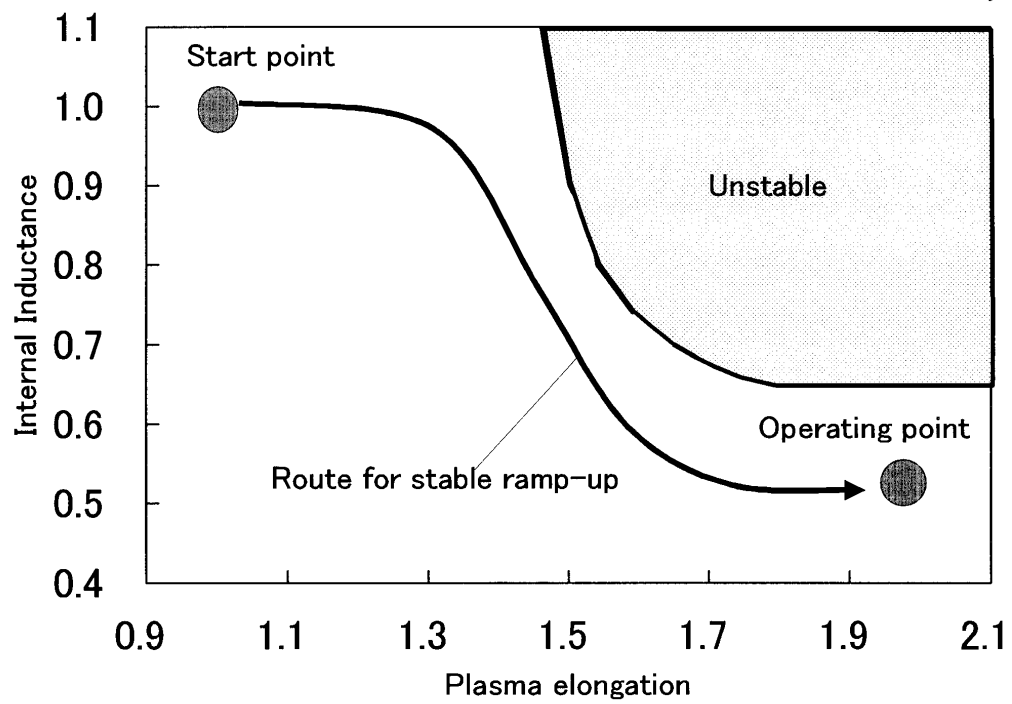


Figure 4.35: Unstable region of positional instability on the internal inductance(l_i) and elongation(κ) plane

Reference

- [4-1] P. N. Yushmanov *et al*, Nucl. Fusion **30** (1990) 1999
- [4-2] H-mode database working group (presented by Thomsen), Nucl. Fusion **34** (1994) 131
- [4-3] J. W. Connor and B. Taylor, Nucl. Fusion **17** (1977) 1047
- [4-4] T. C. Luce *et al*, *16th Conf. Plasma Physics and Controlled Nucl. Fusion Research, Montreal, 1996* F1-CN-64/AP1-3.
- [4-5] C. C. Petty *et al*, Phys. Rev. Lett. **74** (1995) 1763
- [4-6] The JET Team (presented by J. G. Cordey), *16th Conf. Plasma Physics and Controlled Nucl. Fusion Research, Montreal, 1996* F1-CN-64/AP1-2.
- [4-7] F. Ryter *et al*, *16th Conf. Plasma Physics and Controlled Nucl. Fusion Research, Montreal, 1996* F1-CN-64/AP1-5.
- [4-8] H. Shirai *et al*, J. Phys. Soc. Jpn **64** (1995) 4209
- [4-9] J. W. Connor and H. R. Wilson, Plasma Phys. Control. Fusion **36** (1994) 719
- [4-10] J. W. Connor, Plasma Phys. Control. Fusion **37** (1995) A119
- [4-11] H. Nordman *et al*, Nucl. Fusion **37** (1997) 413
- [4-12] ITER confinement database and modelling working group, *16th Conf. Plasma Physics and Controlled Nucl. Fusion Research, Montreal, 1996* F1-CN-64/FP-21
- [4-13] F. L. Hinton and R. D. Hazeltine, Rev. Mod. Phys **48** (1976) 239
- [4-14] A. Taroni, *et al*, JET-P **93** (1993) 84

- [4-15] K. Itoh *et al*, Phys. Rev. Lett. **69** (1992) 1050
- [4-16] K. Itoh *et al*, Plasma Phys. Control. Fusion **35** (1993) 543
- [4-17] A. Fukuyama *et al*, Plasma Phys. Control. Fusion **37** (1995) 611
- [4-18] G. Beteman, Phys. Fluids **B4** (1992) 634
- [4-19] A. Taroni *et al*, Plasma Phys. Control. Fusion **36** (1994) 1628
- [4-20] M. Kotschenreuther *et al*, Phys. Plasmas **2** (1995)
- [4-21] K. Ida *et al*, Phys. Rev. Lett. **65** (1990) 1364
- [4-22] R. A. Moyer *et al*, Phys. Plasmas **2** (1995) 2397
- [4-23] H. Biglari *et al*, Phys. Fluids **B2** (1990) 1
- [4-24] K. C. Shaing *et al*, Phys. Fluids **B2** (1990) 1492
- [4-25] J. W. Connor and H. W. Wilson, Plasma Phys. Control. Fusion **42** (2000) R1
- [4-26] T. D. Carlstrom *et al*, Nucl. Fusion **39** (1999) 1941
- [4-27] E. Righi *et al*, Plasma Phys. Control. Fusion **42** (2000) A199
- [4-28] K. C. Shaing *et al*, Phys. Rev. Lett. **63** (1989) 2369
- [4-29] S-I. Itoh and K. Itoh, Nucl. Fusion **29** (1989) 1031
- [4-30] W. A. Houlberg *et al*, Phys. Plasmas **4** (1997) 3230
- [4-31] ITER Physics Expert Groups on Confinement and Transport and Confinement Modelling and Database, ITER Physics Basis Editors, Nucl. Fusion **39** (1999) 2175
- [4-32] ITER Physics Expert Groups on Divertor, ITER Physics Expert Group on Divertor Modelling and Database, ITER Physics Basis Editors, Nucl. Fusion **39** (1999) 2391
- [4-33] R. J. Groebner *et al.*, Plasma Phys. Control. Fusion. **38** (1996) 1249
- [4-34] F. Ryter *et al.*, Plasma Phys. Control. Fusion. **40** (1998) 725

- [4-35] Hiwatari, R., *et al.*, J. Phys. Soc. Jpn. **67** (1998) 147.
- [4-36] A. S. Kukushkin *et al.*, IAEA-CN77/CT/P-07, Proc. 19th IAEA Fusion Energy Conf. (Lyon, France, 2002)
- [4-37] G. W. Pacher *et al.*, Nucl. Fusion 43 (2003) 188.
- [4-38] R. Hiwatari *et al.*, Nucl. Fusion 44(2004)106.
- [4-39] N. Uckan and ITER Physics Group ITER Physics Design Guidelines:1989 *ITER Documentation Series No.10* (Vienna: IAEA), 1990
- [4-40] Y. Murakami *et al.*, J. Plasma Fusion Res. **77** (2001) 712
- [4-41] T. Yamamoto *et al.*, Fusion Eng. Des. **39-40** (1998) 143
- [4-42] K. Miyamoto and N. Asakura, J. Plasma Fusion Res. **74** (1998) 266
- [4-43] N. Hayashi *et al.*, J. Nucl. Mater. **313-316** (2003) 1041
- [4-44] K. Borrass, Nucl. Fusion **31** (1991) 1035
- [4-45] S. Takamura, J. Plasma Fus. Res. **72** (1996) 866 (in Japanese)
- [4-46] M. Sugihara *et al.*, J. Nucl. Mater. **241-243** (1997) 299
- [4-47] A. Hatayama *et al.*, Nucl. Fusion **40** (2000) 2009
- [4-48] A. Hatayama *et al.*, J. Nucl. Mater. **290-293** (2001) 407
- [4-49] M. Sugihara *et al.*, J. Nucl. Mater. **128-129** (1984) 114
- [4-50] Technical basis for the ITER final design report *ITER EDA Documentation Series No.24* (Vienna: IAEA) 2001
- [4-51] R. Gruber *et al* Comput. Phys. Commun. **21** (1981) 323
- [4-52] H. Naitou and K. Yamazaki Nucl. Fusion **28** (1988) 1751
- [4-53] K. Okano *et al* Plasma Phys. Control. Fusion **32** (1990) 225
- [4-54] K. Okano *et al* Nucl. Fusion **40** (2000) 635
- [4-55] M. Shimada *et al*, Nucl. Fusion **44** (2004) 350

- [4-56] S. Ishida *et al* Nucl. Fusion **43** (2003) 606
- [4-57] A. Möslang *et al* IAEA-CN-94/FT1/2 *Proc. 19th IAEA Fusion Energy conf. (Lyon, October 2002)*(Vienna: IAEA), 2002
- [4-58] Asaoka Y. *et al*, IAEA-CN-116/FTP7/4 *Proc. 20th IAEA Fusion Energy conf. (Vilamoura, October 2004)*(Vienna: IAEA),
- [4-59] K. Okano *et al*, Fusion Eng. Des. **51-52** (2000) 1025
- [4-60] C.Kessel *et al*, Phys. Rev. Lett. **72** (1994) 1212
- [4-61] F. M. Levinton *et al*, Phys. Rev. Lett. **24** (1995) 4417
- [4-62] E. J. Strait *et al*, Phys. Rev. Lett. **24** (1995) 4421
- [4-63] Y .Kamada *et al.*, Proc. 16th IAEA International Conference on Plasma Phys. and Control. Nucl. Fusion Research (Montreal, Canada) vol. 1, p247, 1996
- [4-64] R. C. Wolf *et al.*, Plasma Phys. Control. Fusion **41** (1999) B93
- [4-65] T. H. Osborne *et al.*, Plasma Phys. Control. Fusion **42** (1999) A175
- [4-66] F. Najmabadi *et al* ARIES-AT: An advanced tokamak, advanced technology fusion power plant steady-state tokamak reactor IAEA-CN-77/FTP2/15 *Proc. 18th IAEA Fusion Energy conf. (Sorrento, October 2000)*(Vienna: IAEA),2000 CD-ROM file, <http://www.iaea.org/programmes/ripc/physics/fec2000/html/node1.htm>
- [4-67] S. Nishio, *et al*, J. Plasma Fusion Res. **78**(2000)1218
- [4-68] F. Z. Li *et al.*, Fusion Eng. Des. **39-40** (1998) 109
- [4-69] H. Fujieda, K .Shinya *et al*, JAERI-M 08-256 (Naka-machi:Naka Fusion Research Establishment,JAERI), 1996 (In Japanese)
- [4-70] S. Nishio *et al*, IEEE Transactions on Magnetics **26** (1990) 865
- [4-71] K. Ushigusa, *et al.*, Proc. 17th IAEA International Conference on Plasma Phys. and Control. Nucl. Fusion Research (Yokohama, Japan) IAEA-F1-CN-69/FTP/12, 1998

Chapter 5

Concluding Remarks

In this thesis, plasma performance required for a development scenario of a tokamak-type fusion power plant is investigated.

Chapter 2 shows the plasma performance required for an electric demonstration plant and a commercial power plant. In this thesis, these conditions are named Electric Break-Even Condition and Economic Break-Even Condition, respectively. Under the condition of engineering parameters, a thermal efficiency 30%, a NBI system efficiency 50%, a maximum magnetic field 16 T, and restriction of NBI heating power less than 200 MW, the electric break-even condition requires the simultaneous achievement of $1.2 \leq \beta_N \leq 2.7$, $0.8 \leq HH$, and $0.3 \leq fn_{GW} \leq 1.1$. It should be noted that relatively moderate condition of $\beta_N \sim 1.8$, $HH \sim 1.0$, and $fn_{GW} \sim 0.9$, which corresponds to the ITER reference operation parameters, has a strong possibility to achieve the net electric break-even condition. When the economic break-even condition was analyzed, the break-even price required for introduction in the year 2050 of fusion energy into the world energy scenario is applied to the comparison of economic performance. This break-even price is considered as the necessary condition. Under the same engineering condition except a thermal efficiency 40% and feasibility of a simplified radial build without CS coils, the economic break-even condition requires $\beta_N \sim 2.5$ for 135mill/kWh of upper limit of break-even price and $\beta_N \sim 5.0$ for 65mill/kWh of lower limit of break-even price. The demonstration of steady state operation with $\beta_N \sim 3.0$ in the ITER project leads to the prospect to achieve the upper region of break-even price in the world energy scenario.

Chapter 3 shows a conceptual design of the electric demonstration plant, which is named Demo-CREST, toward the commercial plant CREST. With this conceptual design, the development scenario of fusion energy with ITER, Demo-CREST and CREST was proposed. The plasma configuration for Demo-CREST was optimized so as to sat-

isfy the electric break-even condition with the plasma performance of the reference ITER inductive operation mode. This optimization method is considered to be feasible and credible for the design of a demonstration power plant for early realization of net electric power generation. Within the plasma performance as planned in the present ITER program, net electric power from 0 MW to 500 MW is possible in Demo-CREST with a maximum magnetic field 16 T, thermal efficiency 30 %, NBI system efficiency 50 %, and NBI current drive power restricted to 200 MW. The equilibrium and current ramp-up analysis for the operation point OP1 was carried out as the most severe case for the poloidal field coil system of Demo-CREST. Non-inductive current ramp-up of 2.4MA (15% of total plasma current) is found to be required, however, it is considered to be achievable after the establishment of 85% plasma current.

The operation condition of the divertor plasma is also investigated by using the two-point model. Under the condition of $n_{\text{sol}} \sim 2\langle n_e \rangle / 3$, the outlook for $q_{\text{div}} \leq 10 \text{ MW/m}^2$ of the divertor heat load for Demo-CREST is obtained by the same operation method of impurity seeding as CREST, and the upstream SOL density is found to be the critical parameter for the divertor operation. The precise analysis of the divertor plasma including its effect on the core plasma will be required.

Finally, we have proposed the development path with ITER, Demo-CREST, and CREST for early realization of net electric generation by fusion energy. This development path shows that the early realization of net electric generation such as the Fast Track Approach is feasible. The concept of this development path is based on the effective use of the blanket replacement.

Chapter 4 shows several critical issues on plasma performance in each development stage as for the development scenario proposed in the previous chapter. In the ITER stage, one of the critical issue is the plasma transport phenomena. Generally, the study on the plasma transport is divided into three plasma region, that is, the core plasma region, the core-edge boundary region, and the edge plasma region. As for core plasma region, the validation of plasma transport model with the ITER database was carried out, and the new comparison method, i.e., dimensionally similar simulation, was proposed. As for the core-edge interface region, a model for LH transition phenomena is constructed by using the ion orbit loss concept, and it is found that this model can reproduce the magnetic field and density dependence of LH transition threshold power observed in experiments. As for the edge plasma region, simple Core-SOL-Divertor model to investigate a operation space is developed, and this model shows the possibility of divertor density oscillation during LH transition phase for ITER.

In the Demo-CREST stage, the critical issue is to get the outlook toward the commercial reactor CREST. The development method of the physical and engineering technologies of the commercial plant CREST with the electric demonstration plant Demo-CREST is suggested by the method of replacing the blanket system. This new idea to improve both of plasma and engineering performance by only replacing the blanket system is advantageous for a tokamak fusion reactor. Based on this development method in Demo-CREST, MHD and current drive analysis was carried out, and plasma operation path from ITER-like plasma to CREST-like one was optimized with the same NBI system capacity. In this development scenario, the advanced plasma performance and the advanced engineering technology required for the commercial plant CREST can be demonstrated in the Demo-CREST. When the advanced blanket system with higher thermal efficiency and conducting wall is installed in Demo-CREST, net electric power of about 1000 MW similar to CREST can be produced with a reversed shear plasma configuration.

At last, plasma operation region for highly elongated plasma is discussed. The highly elongated plasma is one of the key to improve the plasma performance. We derived the criterion for the control of the current profile for stable current ramp-up in CREST, and the result is that control from the peaked current profile to the hollow one before attaining the plasma elongation, ($\kappa = 1.5$ in case of CREST) is required. This issue corresponds not only to CREST but also to other designs of a commercial plant with a highly elongated plasma.

In conclusion, this thesis clarified the fundamental conditions (i.e. electric break-even condition and economic break-even condition) and several critical issues on plasma performance as for the proposed development scenario of ITER, Demo-CREST and CREST. Those conditions and critical issues are useful to structure a development scenario, especially, the electric break-even condition and the economic break-even condition discussed in this thesis will contribute to the feasibility study of the development scenario after the ITER project. From now on, it is important to carry out the feasibility study of the development scenario as proposed in this thesis, and accordingly, the priority of the development issues for plasma physics and reactor technology in the fusion energy development should be assessed.

Appendix A

Physical elements of the design database

Table A.1: The physical elements of the design database for tokamak fusion power plants

A	(-)	plasma aspect ratio
B_{tmax}	(T)	magnetic field on TF coils
B_{t}	(T)	magnetic field on magnetic axis
HH	(-)	confinement improvement factor for H-mode
I_{CD}	(MA)	plasma current driven by NBI
I_{bs}	(MA)	bootstrap current
I_{p}	(MA)	total plasma current
M_{n}	(-)	multiplication factor of neutron energy in blankets
P_{α}	(MW)	alpha particle component of total fusion power
P_{NBI}	(MW)	NBI input power for current drive
P_{N}	(MW)	neutron component of total fusion power
$P_{\text{e}}^{\text{circ}}$	(MW)	circulating electric power
$P_{\text{e}}^{\text{gross}}$	(MW)	gross electric power
$P_{\text{e}}^{\text{net}}$	(MW)	net electric power
P_{f}	(MW)	total fusion power
P_{th}	(MW)	total thermal output power
$P_{\text{w}}^{\text{ave}}$	(MW/m ²)	averaged neutron wall load
Q	(-)	energy multiplication factor

R_p	(m)	plasma major radius
S_p	(m ²)	plasma surface
T_{ave}	(keV)	volume averaged plasma temperature
V_p	(m ³)	plasma volume
a_p	(m)	plasma minor radius
f_N	(-)	covering fraction of blanket for the plasma surface
$f n_{GW}$	(-)	ratio of Greenwald density limit
n_{GW}	(10 ²⁰ m ⁻³)	line averaged electron density
n_e	(10 ²⁰ m ⁻³)	volume averaged electron density
n_i	(10 ²⁰ m ⁻³)	volume averaged ion density density
p_f	(MW/m ³)	fusion power density
q_ψ	(-)	safety factor at 95% flux surface
Ψ_{ramp}	(V·s)	flux for current ramp-up
β	(-)	total plasma beta value
β_α	(-)	alpha particle component of plasma beta value
β_N	(-)	normalized beta value
β_{th}	(-)	thermal component of plasma beta value
δ	(-)	plasma triangularity at 95% flux surface
ϵ	(-)	plasma inverse aspect ratio
η_{NBI}	(-)	NBI system efficiency
η_α	(-)	collecting rate for the energy of alpha particle
η_{beam}	(-)	collecting rate for the energy of NBI input power
η_e	(-)	thermal efficiency of electric conversion
κ	(-)	plasma elongation at 95% flux surface
τ_E	(s)	energy confinement time
$\tau_{E,th}^{IPB98(y,2)}$	(s)	scaling law of energy confinement time for H-mode

Appendix B

Conceptual design studies of fusion power plants

Figure B.1: Major parameters of the previous design studies for fusion power plants and ITER.

	A-SSTR2[3-3]	ARIES-AT[3-2]	CREST[3-1]	IDLIT[3-26]	SEAFP[3-27]	SSTR[3-28]	ITER[3-10]
Major radius	6.2	5.2	5.4	10.0	9.4	7.0	6.2
Aspect ratio	4.0	4.0	3.4	5.35	4.5	4.0	3.1
Plasma elongation	1.8	2.2	2.0	1.7	1.66	1.8	1.7
Plasma triangularity	0.4	0.84	0.5	0.3	0.2	0.3	0.35
Plasma temperature	19	16	15.5	13	10	17	8.8
Plasma surface safety factor	4.8	4.0	4.3	3.0	3.9	5.0	3.0
Max. magnetic field	20.5	11	12.5	13	12.8	16.5	12